Uptake Mechanism, Intracellular Trafficking and Endo-lysosomal pH Monitoring of Polystyrene Nanoparticles

Dissertation
zur Erlangung des Grades
Doktor rerum naturalium (Dr. rer. nat.)

Max Planck Graduate Center
mit der Johannes Gutenberg-Universität Mainz
Angefertigt am Max-Planck-Institut für Polymerforschung

Simone Lerch
Geboren in Haan

Mainz 2011

Amtierender Dekan: Name entfernt

Gutachter:

    1. Gutachter: Name entfernt

    2. Gutachter: Name entfernt

Tag der Einreichung: **09. November 2011**

Tag der mündlichen Prüfung: **16. Januar 2011**

1   *Table of content*

2 Abbreviations

2AK	Secondary antibody
AEMH	Aminoethyl methacrylate hydrochloride
AM	Acetoxymethyl
BSA	Bovine serum albumin
CatD	Cathepsin D
Cav	Caveolin
CE	Caveolin-EGFP conctruct
CHC	Clathrin heavy chain
CLSM	Confocal laser scanning microscopy
CMC	Critical micelle concentration
CTB	Cholera toxin subunit B
CTMA-Cl	Cetyltrimethylammonium chloride
DLS	Dynamic light scattering
DMEM	Dulbecco's modified eagle medium (cell medium)
Dyn2	Dynamin 2
EC	EGFP-Caveolin construct
EEA1	Early endosome antigen 1
EGFP	Enhanced green fluorescent protein
FCS	Fetal calf serum
ICS	Immuncytochemical staining
Lamp1	Lysosomal associated membrane protein 1
LUT	Lookup table

M6PR	Mannose-6-phosphate receptor
NP, NPs	Nanoparticle, nanoparticles
PCD	Particle charge detection
PDM	Product of the differences from the mean
PEBBLE	Photonic explorer for bioanalysis with biologically localized embedding
ROI	Region of interest
SNR	Signal-to-noise ratio
SW	Single wavelength (fluorescent sensors)

3 Motivation

Converging scientific disciplines to create novel systems for health benefits has been attempted over the last decades by top-down approaches by medics, e.g. in miniaturizing existent analytical devices, techniques and biomedical materials as well as by bottom-up methods, e.g. in molecular engineering and supramolecular chemistry. Nanomedicine, in particular nanoparticles (NPs), have evolved in consequence as one of the newest cancer-specific treatments and some have already passed worldwide quality, safety, efficacy and risk management regulations [1]. The first attempts range back into the 1970s, where reactive drugs, e.g. Caelyx® have been incorporated into liposomes [2]. Nowadays, one example for novel drug delivery systems is the albumin-bound paclitaxel called Abraxane® that is applied for breast cancer treatment [3]. Drug delivery is an important field to enhance further developments. The global market for novel drug delivery systems was more than € 37.9 billion in 2000 [4].

Mihail Roco has described four generations of purposeful nanotechnology development for the near future [5]. The first generation, the current era, deals with passive nanostructures such as aerosols, colloids or products with incorporated nanomaterials. The second phase, which is just about to begin, features active nanostructures for the targeting and delivery of drugs and biodevices. The third generation which is expected to begin in the next decade will consist of active nanostructures interacting with each other, i.e. guided networks and simple self-evolutionary processes. The last era, due in the 20s, has the competence of building molecular devices such as "nanorobots" by design, in a way that Richard Feynman theorized 1959 [6].

The main advantages of combining effective pharmaceutics with nanotechnological systems, i.e. to design 2nd generation nanotechnology for biomedical application lie in the possibility for drug targeting and controlled release. In addition, stealth drug-NP conjugates minimize drug degradation, may prevent harmful side effects and increase bioavailability. Apart from delivering active reagents to specific cellular targets, nanoparticles are also introduced for medical imaging and multipurpose diagnostic sensors as they are easily tagged with

fluorescence or MRI labels [7]. Systems tested in current drug delivery research include soluble polymers, microparticles made of insoluble or biodegradable material, natural and synthetic polymers, microcapsules, cells, cell ghosts, lipoproteins, liposomes, and micelles [8]. Potential future applications for novel drug delivery systems are not restricted to targeting cancer cells, but include

- the elimination of bacterial infections in a patient as an alternative for antibiotics,
- the ability to perform surgery at a cellular level, removing individual diseased cells and even repairing defective portions of individual cells and
- a significant lengthening of the human life span by repairing conditions that cause aging at a cellular level.

However, the biodistribution of NPs after intravenous or subcutaneous application remains an obstacle and is hard to control by means of NP design. Recent studies in mice show that the biodistribution is a function of NP size and charge and that a main influence is the opsonization in the liver [9].

The release of a drug from a nanoparticular compound depends inter alia on the biodegradability of the material and the metabolic activity of the target cells. Drug release may also be triggered by external stimuli, e.g. a change in pH or temperature. The targeting of NPs, however, must be understood on two different levels. NPs can address specific tissue types within a body, i.e. cancer cells, but they can also address specific compartments within a cell, i.e. vesicles from the endo-lysosomal compartment, the cell nucleus or cytoplasm. Targeting of NP is dependent on passive and active influences. Passive influences are considered to be NP properties such as size, charge and material. Active influences are bioreactive components attached to the particle surface as "address labels", such as antibodies or other targeting moieties. The intracellular distribution of NPs is important for the concerted design, as this may affect drug efficacy. In addition, an acidification of NPs in lysosomal compartments can not only influence NP degradation but also their pharmaceutical potency.

Nanomaterials are mainly taken up into the cell by an endocytotic pathway. In this process, the material is enwrapped by a lipid double layer that origins from the cell membrane. These newly formed vesicles undergo different ripening processes that can end in the degradation of material in lysosomes, the transportation back to the cell membrane and subsequent disposal into the exoplasm (exocytosis), the mere storage of the material or even the release into the cytoplasm. Each different compartment along these intracellular pathways is determined by a set of marker proteins, e.g. small GTPases and can in addition involve an acidification process.

For target-driven design of NPs, it is important to be able to specifically control the processes that involve endocytosis of NPs to cells. The aim of this work is to synthesize comparable sets of non-toxic, bio-inert polystyrene NPs that vary only in size to define the influence of NP size on the uptake to cells and to design a novel nanosensor to probe the acidification process of NPs after endocytosis. The impact of NPs on the uptake kinetic with different sizes with regard to their concentration, amount and overall surface area shall be investigated. In addition, the endocytotic mechanism will be determined with three different techniques, i.e. pharmacological inhibitors, immunecytological staining, and immunefluorescence. The pH-dependent dye SNARF-4F shall be grafted onto the surface of polystyrene NP to create a nanosensor for the investigation of the pH changes in the NP environment after endocytosis.

The results presented in this work should add to the determination of NP – cell interactions and will help in the future to design purpose-driven 2nd generation NPs for novel drug delivery systems. This thesis is addressing several aspects regarding the uptake of nanoparticles into cells:

- What is the influence of size on the amount of NPs uptake into cells?
- Which endocytotic mechanisms are involved?
- Do NPs of different sizes use different endocytotic mechanisms?
- In which specific endo-lysosomal compartment are NP found after the uptake into cells?
- Can particles as a type of nano-sensors detect their environmental pH value while being present in the endo-lysosomal pathways?

4 Theoretical Background

A broad variety of polymerization methods to synthesize NPs with a whole set of different properties enables researchers to gain detailed insights on the interaction of NPs with mammalian cells. However, combinations of a thorough NP colloidal characterization with an exact determination of uptake mechanisms as a function of NP properties are rare. This chapter gives an overview over: i) three polymerization approaches used for NP synthesis, ii) the processes involved in cellular endocytosis iii) the different down-stream fates of molecules and NP and iv) the design and medical application of pH-sensitive NPs.

4.1 Synthesis of polymeric nanoparticles through dispersion, seed and miniemulsion polymerization

Many different approaches have been applied for the radical polymerization of numerous vinyl monomers leading to a broad variety of synthesizable NPs with tunable distinct properties, like material, size, incorporated material or surface charge [10-12].

In the dispersion polymerization (see Scheme 1 A) an initially homogeneous system becomes heterogeneous upon polymerization, because the polymer is insoluble in the solvent. In current work, the monomer, initiator, hydrophobic fluorescent dye (Lumogen F Red, see Figure 1) and a polymeric, protective colloid alternatively non-ionic surfactant (Lutensol AT50, see Figure 1) are solved in an ethanol/water mixture. During polymerization, the growing polystyrene chain becomes insoluble and precipitates in the form of globules stabilized by the surfactant. Upon precipitation, the hydrophobic dye is entrapped inside the NPs. The dispersion polymerization is suitable for the synthesis of monodisperse, non-ionic particles in a size scale between 0.5 and 10 μm. However, in some cases it is difficult to apply this method for the copolymerization. The difference in solubility of monomer and comonomer may lead to the formation of two different homopolymeric NPs [13, 14].

Comonomer
2-Aminoethyl methacrylate hydrochloride (AEMH)

Cationic surfactant
(1-Hexadecyl)-trimethylammoniumchloride (CTMA-Cl)

Nonionic surfactant
Lutensol AT50 or AT80

Fluorescent dye
Lumogen F Red
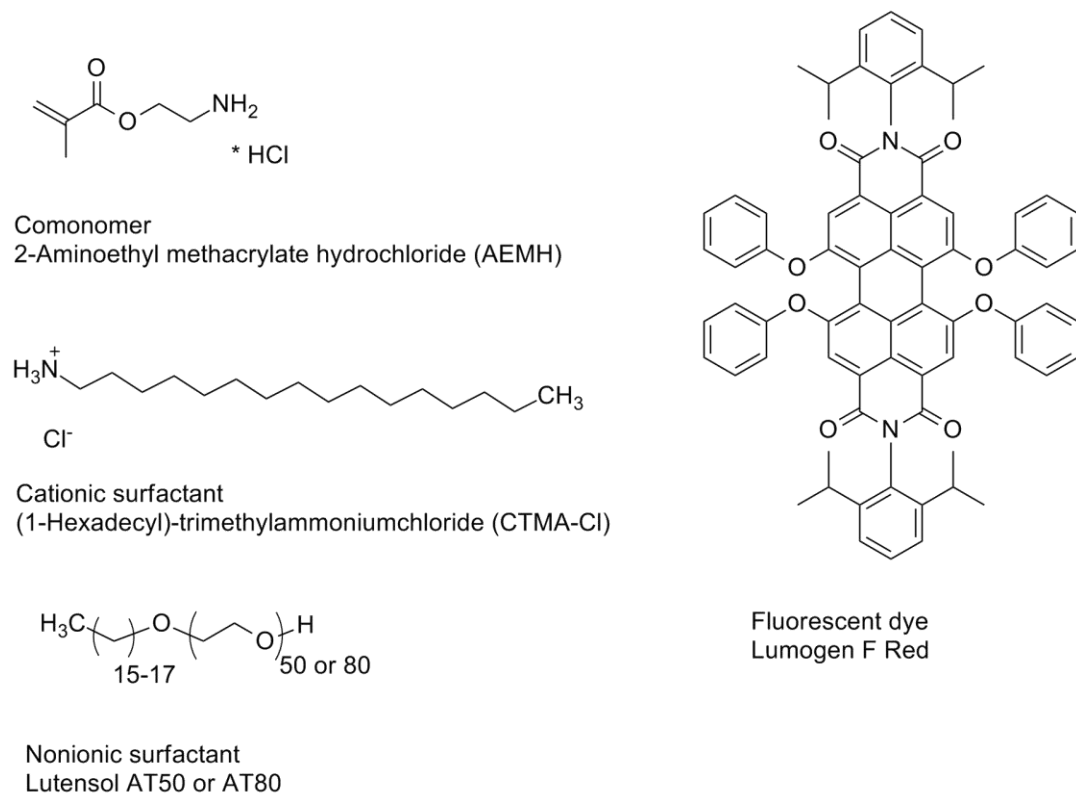
Figure 1: Chemical structure of the comonomer AEMH used for the copolymerization in miniemulsion polymerization and the surfactants: i) CTMA-Cl used in miniemulsion and seed polymerization and ii) Lutensol AT50 and AT80 used in miniemulsion and dispersion polymerization. The perylene fluorescent dye Lumogen F Red is incorporated into the particle as a marker.

The seed polymerization (Scheme 1 C) enlarges pre-formed core particles by swelling and polymerizing them with drop-wise added monomer. The seed polymerization is suitable for the synthesis of monodisperse and electrostatically stabilized particles over a large size scale as a function of the monomer amount and mode / feed rate of the monomer addition. This method features two main drawbacks: i) the copolymerization reactions are hard to control and ii) incorporation of the material, e.g. a fluorescent dye (see Figure 1), is not possible during the seeding. The "payload" must be present in the core particles. It should also be kept in mind that the swelling process results in the reduction of "payload" concentration per $g_{Polymer}$ [15-22].

The miniemulsion polymerization (see Scheme 1 B) is based on the formation of an oil-in-water miniemulsion stabilized by ionic or non-ionic surfactants using high shear homogenization, e.g. ultrasonication, followed by the particle formation via polymerization. This technique comprises

many possibilities in terms of controlled copolymerization (e.g. amine functionalization with the comonomer AEMH, see Figure 1) and incorporation of material (e.g. fluorescent dye Lumogen F Red, see Figure 1). The particle size can be controlled in a range between 50 and 500 nm [23]. Furthermore, the introduction of reactive groups such as amines to the particle facilitates further reactions at the NP surface, e.g. the immobilization of sensor molecules.
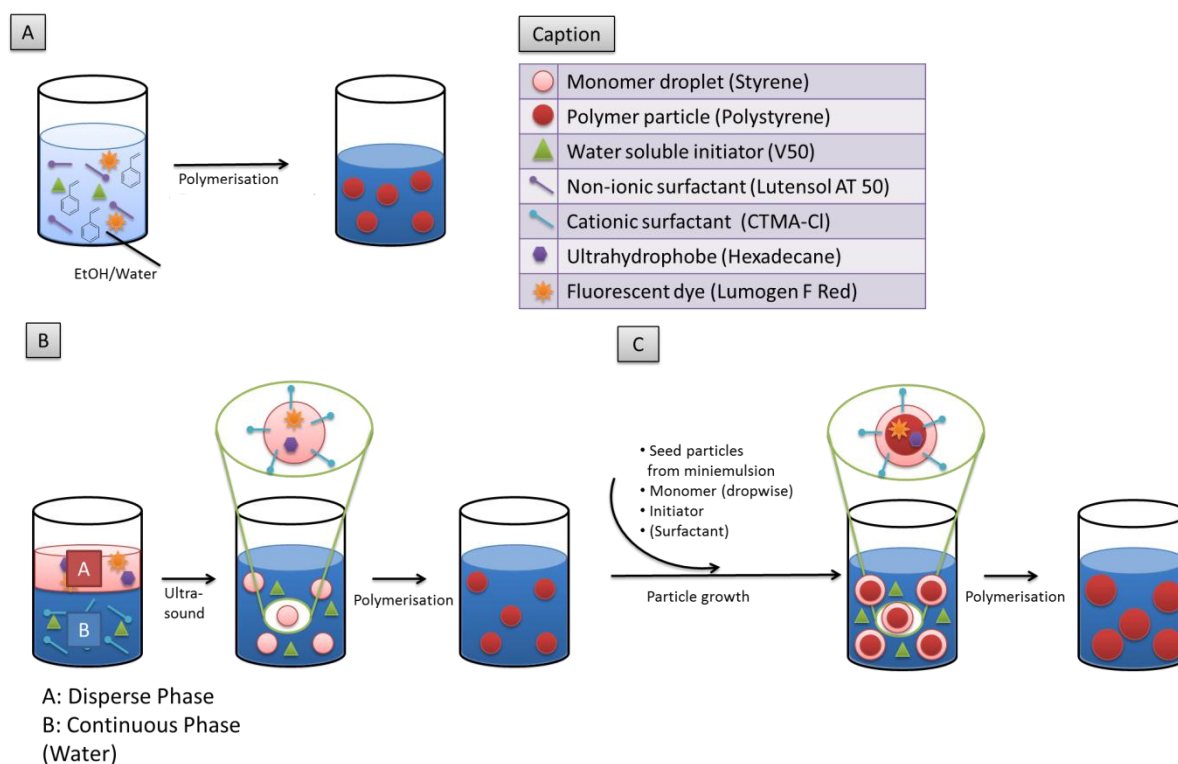
Scheme 1: Polymerization methods used for the synthesis of cationic and non-ionic polystyrene particles with different sizes. A: Dispersion polymerization, B: miniemulsion polymerization, C: Seed polymerization.

4.2 Interaction of nanoparticles with the endocytotic machinery

The endocytotic pathway is used by cells for the uptake of nutrients, like amino acids, sugars, fatty acids, coenzymes, hormones, neurotransmitters, and salts [24], down-regulation of plasma-membrane growth factor receptors [25] as well as monitoring the signaling pathways [26, 27]. Endocytotic pathways are also used by viruses to enter cells [28]. It was found years ago that the uptake of nanoparticles undergoes the same routes as that of aforementioned molecules. As a classical scheme, endocytosis is classified in a) non-receptor mediated

endocytosis, i.e. macropinocytosis and phagocytosis, where dissolved or liquid material and larger contaminants or bacteria are taken up respectively without a sorting process and b) receptor-mediated endocytosis. The latter includes conventionally clathrin-mediated endocytosis, caveolin-mediated endocytosis and a clathrin- and caveolin-independent endocytosis. The caveolin-triggered uptake into so called caveosomes was also discussed [29], but recent studies suggest that caveosomes are merely an artifact from overexpressed caveolin [30].

In recent years, several additional pathways mainly regulated by small GTPases were found: among others, RhoA- [31, 32], Cdc42/Arf1 [33, 34]- and Arf6 [34]-dependent endocytosis. A second form of exvaginated uptake is referred to as circular dorsal ruffles [35], which is known to be actin- and dynamin-dependent.

A major role plays the small GTPase dynamin, which is responsible for the scission of newly formed vesicles. Dynamin forms a spiral that contracts upon GTP hydrolysis which leads to the pinching off of the vesicle from the plasma membrane [36]. Endocytotic processes are often distinguished as dynamin-dependent and –independent. Dynamin participates in clathrin-mediated endocytosis, caveolin-mediated endocytosis, RhoA-mediated endocytosis and endocytosis via circular dorsal ruffles [26, 29, 37-41].

It is possible for the different routes to be combined in the further downstream processing, when vesicles mature to different types of endosomes, multivesicular bodies, or lysosomes [41]. The endosomal vesicles can change their identifying protein attendance, making it hard to track back the original uptake mechanism. The monomeric Rab (Ras-related in brain) GTPases are one of the most common downstream endocytosis regulator families. They regulate the vesicle trafficking, formation and fusion [42]. An overview of possible entries into the cell for NPs and the resulting intracellular fate is given in Scheme 2.
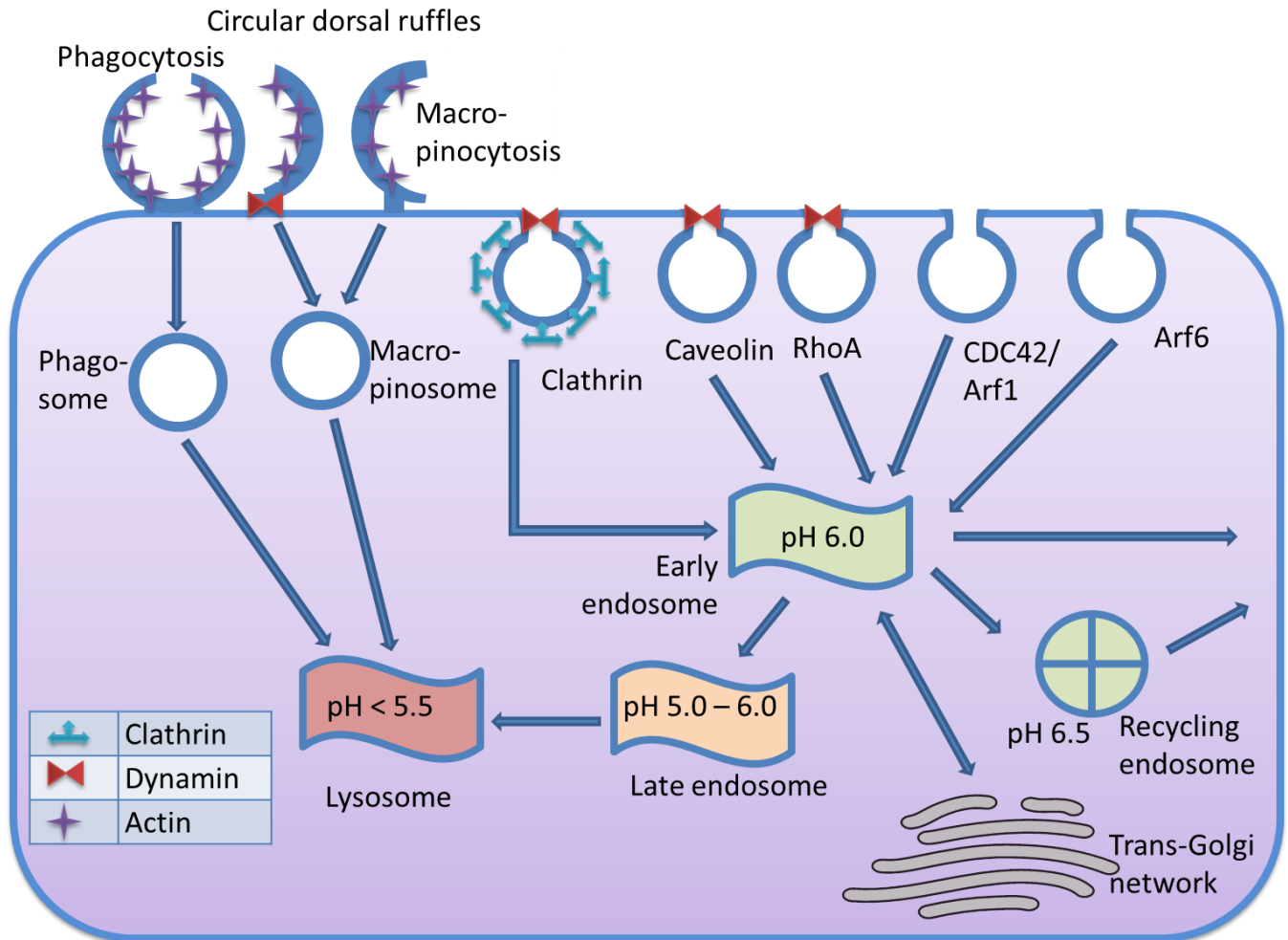
Scheme 2: Possible uptake mechanisms for NPs in cells.

F-actin is classically known to participate in exvaginating endocytotic processes, like macropinocytosis and phagocytosis [38, 41]. Recent studies also reveal the support of F-actin in different endocytotic processes, e.g. clathrin-mediated endocytosis [43]. The role of actin includes: i) deformation and vagination of the plasma membrane, ii) formation of vesicle "neck", iii) creation of cytoskeletal structures to sort endocytotic participants, and iv) transport of vesicles through the cytoplasm. It was shown that endosomes, pinosomes, clathrin-coated vesicles and secretory vesicles are associated to the cytoplasm by a so called actin tail [44-46].

To determine the way NPs enter the cell, i) specific inhibitors e.g. chlorpromazine, ii) intracellular antibody staining, e.g. with antibodies against clathrin heavy chain and iii) cells expressing mutated proteins, e.g. a caveolin-GFP conjugate can be used. These systems are well

established for the above-mentioned well-known pathways. However, with increasing knowledge of additional uptake routes, the existence of downstream "junctions" and the possibility of molecules being taken up by several pathways [35], the cellular uptake system becomes very complex and established methods may affect or detect several mechanisms. Hence, interpretation of data must be done with care and considering several methods in combination.

4.2.1 Endo-lysosomal compartmemnts

The endo-lysosmal network is a complex machinery where lipids and proteins are dynamically transported between the plasma membrane, intracellular vesicles and the trans-Golgi network. Each structure is defined as an accumulation of specific molecules that function as markers, sorters or fusion proteins. However, these sets of markers are interchanged constantly, which makes distinct definitions hard to achieve.

Clathrin heavy chain is a protein that participates in the wrapping of clathrin-coated vesicles. Three heavy chains and three light chains form a triskelion that provides the structural backbone of a clathrin basket [47]. Once budded from the membrane, the clathrin-coated vesicle is uncoated and clathrin heavy chains travels back to the plasma membrane. Appearance of clathrin heavy chain in endo-lysosomal compartments does not occur. Dynamin, as was mentioned before, is a GTPase that participates in the scission of vesicles from the membrane and takes part in several endocytotic mechanisms. The subform Dyn2 is expressed in most cell types, whereas Dyn1 and Dyn3 are localized in neurons and testis, respectively [36, 48, 49]. Caveolin1 (Cav1) is the main component of the lipid raft caveolae, a plasma membrane microdomain enriched in proteins like caveolin and lipids like cholesterol and sphingolipids. The subform Cav2 is expressed similarly ubiquitious like Cav1, whereas Cav3 is restricted to striated and smooth muscle [29, 30]. Early endosome associated protein 1 (EEA1) is present only in early endosomes where it binds the membrane-intrinsic phosphatidylinositol-3-phosphate. It plays a role in endocytotic docking and fusion [50]. Lysosomal associated membrane protein 1 (Lamp1) also called cluster of differentiation 107a (CD107a) belongs to the family of membrane glycoproteins and is one of over 50 known integrated membrane proteins present only in

lysosomes where it participates in the sorting of endocytosed material [51]. The mannose-6-phosphate receptor (M6PR) transports mannose-6-tagged lysosomal hydrolases from the trans-Golgi network to late endosomes and lysosomes [51]. One of the hydrolases resident in lysosomes is cathepsin D (CatD). Cathepsin D is an aspartic protease that gets activated at a pH < 5.0 and cleaves, among others, fibronectin and laminin [52].

An overview of the above mentioned most common proteins and their participation in endocytotic trafficking, sorting and digesting is given in Scheme 3.
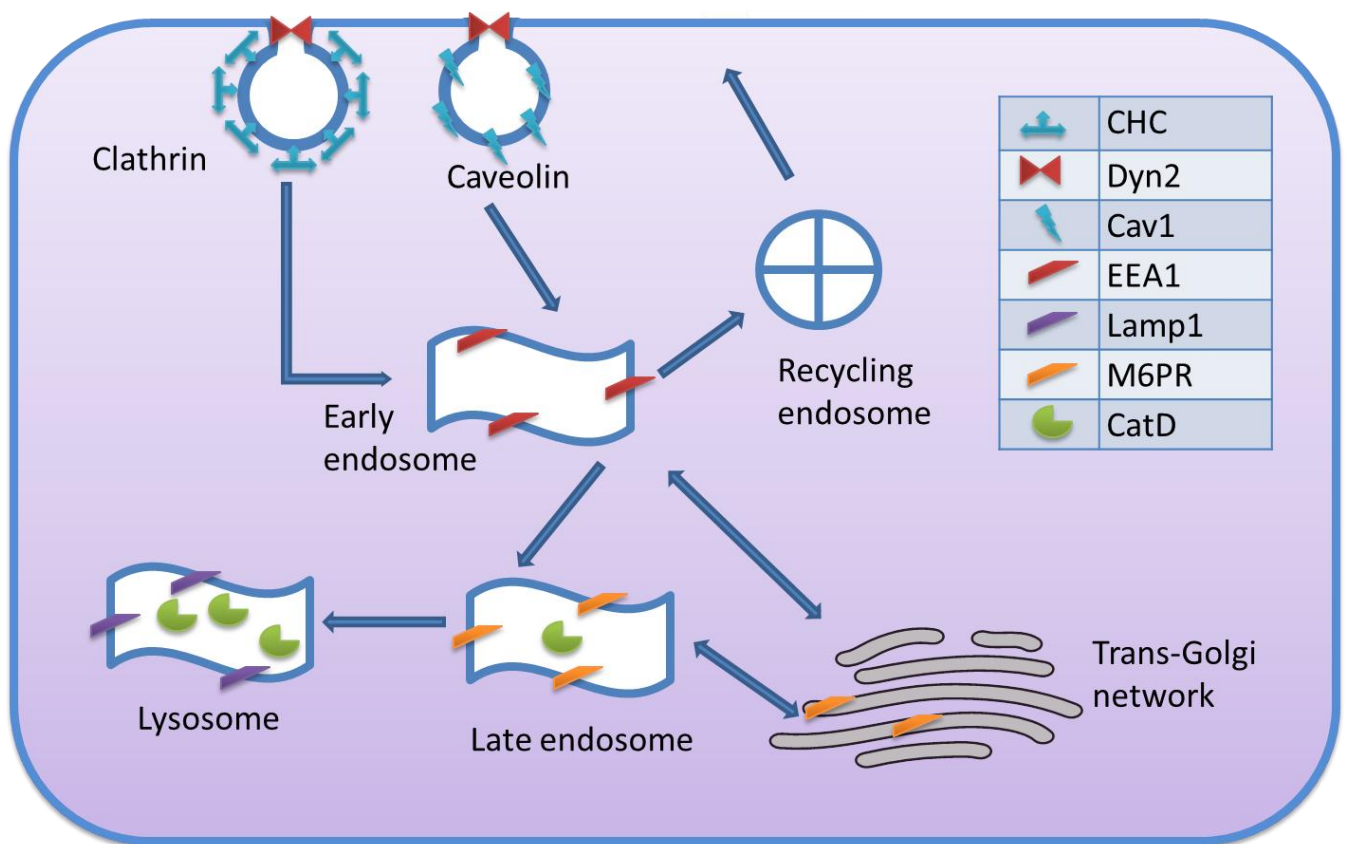
Scheme 3: Compartimentalization of selected proteins in the trafficking, sorting and digestion of endocytosed material. CHC: clathrin heavy chain, Dyn2: dynamin-2, Cav1: caveolin-1, EEA1: early endosome associated protein 1, Lamp1: lysosomal associated membrane protein 1, M6PR: mannose-6-phosphate receptor, CatD: cathepsin D.

4.2.2 Size effect on the NP uptake

As the endocytotic process distinguishes in a most complex manner between different proteins, lipids and sugars dependent on their chemical and biological properties, the uptake of NPs

depends on their characteristics. Main factors like material [53, 54], surface charge [55-61], coating material and thickness [62], size and shape [37, 40, 60, 63, 64], control the kinetic and the cell uptake route. Other parameters arise from additional functionality of the particles with bioactive molecules such as receptor-ligands or antibodies [65], the cell line [66] and so on. For novel approaches in designing nanoscale drug delivery systems, a deep understanding of the tracking of the process inside the cell is of high importance.

Several recent publications report the size-dependent uptake to cells. From the obtained data it can be summarized that carcinoma cells have a higher endocytosis rate than confluent ones [67]. This implies that the uptake is cell-type dependent. Mouse carcinoma cells, as an example, only endocytose particles smaller than 20 nm, which is very uncommon for many other cell lines, like human adenocarcinoma cells [54] or cervix carcinoma cells [55]. It is also reported that non-tumorous cell lines internalize bigger particles easier than tumorous ones [68]. Especially macrophages have a size optimum of 1 μm and literally ignore smaller (200 nm) and bigger (10 μm) particles [61], mainly due to their specific role as scavenger cells in the human immune system. Furthermore, particles can not only be endocytosed but also transported across the cell and transcytosed [69].

The reasons for the variances in the uptake of particles with different size are still to be explored thoroughly. There are indications that the interaction of the particles with the cellular membrane is independent from their size [69]. At the same time the way of endocytosis, e.g. clathrin-dependent or caveolin-dependent endocytosis, or macropinocytosis, is strongly size dependent [40].

Although many papers have been published on the cell uptake studies, the obtained results cannot be directly compared, due to the different experimental conditions and often not completely characterized particles. Particle properties, such as surface charge, amount of fluorescent dye, particle size and size distribution, morphology and so on should be well defined to be able to compare the cell uptake results.

4.3   The role of pH in nanomedicine: Nanoparticles as sensors

For the last decade, polymeric nano-sensors have been synthesized as probes for real-time imaging and dynamic monitoring of various ions that are important for the cellular metabolism, such as H^+, Ca^{2+}, Mg^{2+}, K^+, Na^+, and Cl^- [70-73]. NP sensor-based systems have several advantages in comparison to the use of unconjugated single fluorescent analytes [74] and to high invasive methods like e.g. microelectrode probing [75]. The main advantages are i) that they are physically and chemically non-invasive due to their small size and inert material, ii) that the accessibility of the analyte can easily be tuned because of a high surface-to-volume ratio and the material, and iii) that the uptake and trapping of sensors to cells as well as local analyte concentration can be easily adjusted [76]. Surface properties of NPs [77] as well as multiple functionalization, like additional incorporation of drugs [78], MRI-detectable anorganic labels [79], or antibodies [80], e.g. as delivery targets, can be easily tuned. The most common PEBBLE (photonic explorer for bioanalysis with biologically localized embedding) method is used to embed an analyte sensitive dye into a porous biologically inert matrix [81] and can include advanced fluorescent methods such as fluorescent resonance energy transfer (FRET) based probes [82], ion correlation [83], surface-enhanced Raman scattering (SERS) [84] and modulated optical nanoprobe (MOON) [85] sensors. This sensor matrix is then positioned inside the cell by liposomal delivery [86], membrane-penetration peptides like TAT [87] or gene gun [88] for cytoplasmatic analysis.

In recent years, NPs have also emerged as promising tools to study the cell mechanisms as well as to function as novel drug delivery systems for the transportation of drugs to the specified cell or tissue types. Most NPs are taken up by the cells via various endocytotic mechanisms following the endo-lysosomal pathway [38]. To trigger the release of receptor-bound ligands, such as the well described LDL receptor recycling [89], and to digest assimilated nutrients, the pH of these compartments is acidified during the maturation of the vesicles from early to late endosomes and lysosomes. This acidification can be used to trigger the degradation of biocompatible polymeric nanocapsules and to release incorporated markers or drugs [90]. For example, an acid-sensitive (6-maleimidocaproyl)hydrazone derivate of doxorubicin (DOXO-EMCH) can address tumor cells after binding to albumin by passive targeting and releases the

drug after acidification [91]. Since changes in the local ion concentration, such as H^+ play an important role in metabolic processes, ion transport, cell signaling and cell growth [92], it is important to determine different pH values with a high spatial resolution. Intracellular pH changes also take part in the development of tumor cells, e.g. the pH_i of some tumors rises due to an increased P-glycoprotein activity [93]. Hence, ionic analytes are measured routinely in cancer diagnostics [94].

Up to now, not many studies are published that combine the novel properties of sensor NPs with their ability to work as pH-sensitive drug delivery systems and the quantitative monitoring of NPs in endocytotic vesicles. Little is known on the accurate interactions and the time scales of NP endocytosis to cells. However, to tailor nanoscale systems for the delivery of drugs by pH-triggered release of incorporated material, it is important to specify the acidification kinetics of NP in the endo-lysosomal system. To address this question, a pH-sensitive dye Snarf-4F was grafted onto the surface of NPs to create a pH-sensitive nanosensor for monitoring the acidification of NPs after the uptake into cells.

4.3.1 The pH-sensitive fluorescent dye SNARF-4F

A variety of pH-dependent sensors has been developed in recent years. In general, they can be classified into mono- and dual-wavelength fluorescence. The former exhibits a shift in fluorescence intensity, the latter in emission wavelength upon excitation in different pH environments. Common mono-wavelength pH sensors are fluorescein and BCEF. Dual-wavelength dyes like the SNARF and Snafl indicators, HPTS and Oregon Green cover a large region of pK_a values from 8.0 (HPTS) – 3.5 (LysoSensor) [74]. 2-(10-(Dimethylamino)-4-fluoro-3-oxo-3H-benzo[c]xanthen-7-yl) (SNARF-4F) is a pH-dependent fluorescent dual-wavelength dye with a rather acidic pK_a of ~ 6.4 [95]. The protonated form (Figure 2 AH) emits light upon excitation at a lower wavelength than the deprotonated form (Figure 2 A). The pH value can be calculated from the intensity ratio of the two emission wavelengths so that problems arising from concentration changes such as with mono-wavelength pH-dependent dyes (e.g. fluorescein) can be overcame. SNARF-4F undergoes a conformation change to the non-fluorescent lactone form (Figure 2L) in the presence of organic solvents, e.g. methanol or

DMSO. The lactone conformation also appears in the cell-penetrable acetoxymethyl (AM) ester form (Figure 2 L ester) of the dye, but is not reversible upon redispersion in water. After penetrating the cell membrane, the ester is hydrolysed by unspecific cytosolic esterases and transferred into the fluorescent form.
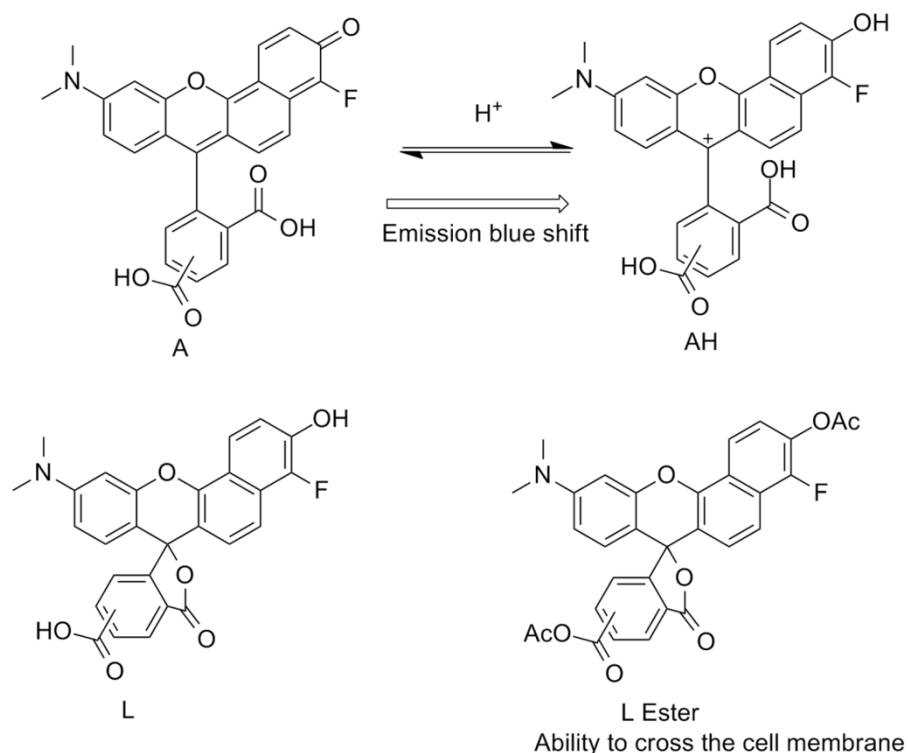
Figure 2: Deprotonated (A), protonated (AH), lactone (L) and lactone ester (L ester) form of SNARF-4F.

4.3.2   Sensor conjugation

To immobilize SNARF-4F on to the NP surface, a reaction must be performed between the Snarf-4F molecule carboxylic group and the amino groups of the particle. EDC is ranked a so called zero-length crosslinker as it forms a direct bond between the substance and the conjugate without additional atoms in between. Thus the side-reactions are eliminated. In addition, the coupling reaction is performed in aqueous media, which is important because NPs are not stable in the organic solvents. 1-Ethyl-3-(3-dimethylaminopropyl)carbodiimide hydrochloride (EDC) is the most common crosslinking agent used and numbers of coupling protocols has been

described in the literature. Other zero-crosslinking conjugation mediators between carboxylic and amino groups include Woodward's Reagent K (N-ethyl-3-phenylisoaxazolium-3'-sulfonate), N,N-carbonyldiimidazoles as well as other carbodiimides such as 1-cyclohexyl-3-(2-morpholinoethyl)carbodiimide (CMC) and dicyclohexyl carbodiimide (DCC).

After activation of the dye with EDC, the obtained o-acylisourea is prone to the hydrolysis. To stabilize the intermediate and prevent side reactions, such as formation of N-acyl urea [96], HOBt is used as a catalyst to form a corresponding HOBt ester, which is more insensitive to hydrolysis and can rapidly form an acrylate with the particle. This nucleophilic reaction is furthermore favored by increasing the pH to 8.6. The reaction scheme is shown in Figure 3. The isourea that is formed as a by-product as well as all other reaction partners are water-soluble and can therefore be easily removed by centrifugation.
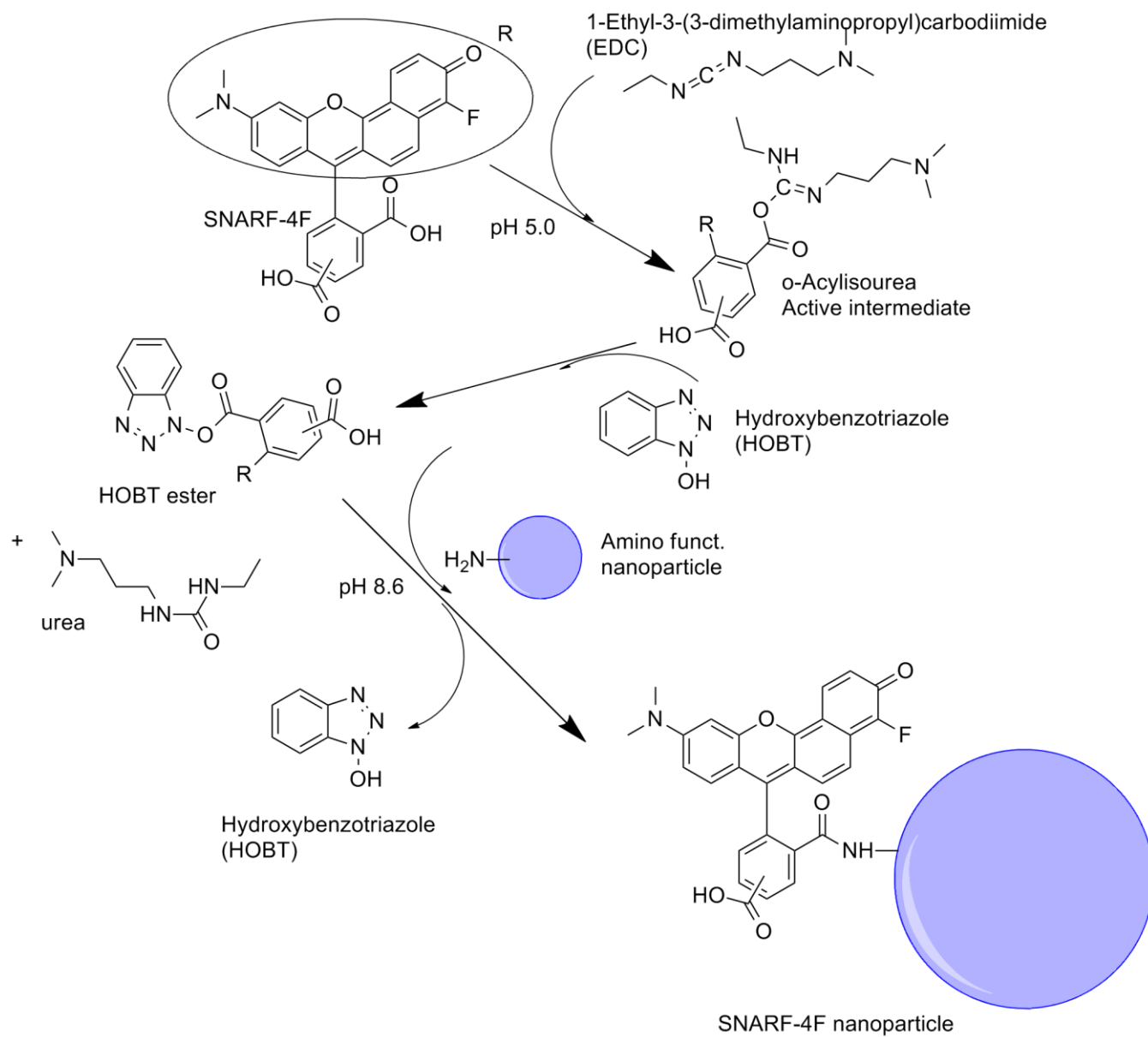
Figure 3: EDC coupling between the pH-sensitive dye SNARF-4F and amino functionalized NPs.

5 Experimental part

In the interdisciplinary research, a large number of different methods needs to be employed for the characterization of NPs and for studies of NP cell interaction. In the following, a description of methods used for colloidal characterization and for cellular studies is presented. A list of chemicals and devices used is listed and experimental specifications for NP synthesis, NP characterization, cell culture and cell uptake are provided.

5.1 Analytical procedures for the characterization of nanoparticles

To draw adequate conclusions on the interaction of NPs with the cells, the physicochemical properties of NPs should be exactly defined. The colloidal attributes presented in this work are: particle size and size distribution, surface charge density, amount of incorporated dye, amount of non-ionic surfactant and particle morphology.

5.1.1 Dynamic light scattering

The light, which hits NPs dispersed in solution is scattered either equally in all directions (Rayleigh scattering) or, is angle-dependent (Mie scattering), if the particle is larger than approx. 250 nm. Due to the particles' Brownian motion, they move forwards and backwards in the illuminated field, thus causing constructive and destructive Doppler interference. This fluctuation is measured by dynamic light scattering (DLS) and can be fitted to an autocorrelation function that yields the diffusion constant of the dispersion. The hydrodynamic radius R_H of a particle in solution is given after the Stokes-Einstein equation as indirectly proportional to the diffusion constant:

$$R_H = \frac{k_B \cdot T}{6 \cdot \pi \cdot D'} \qquad (1)$$

where k_B is the Boltzmann constant, T is the temperature and D is the diffusion constant. The error of the fit function in correspondence to measured data correlates with the polydispersity of the sample [97].

A measurement comparison between large and small particles is depicted in Scheme 4.
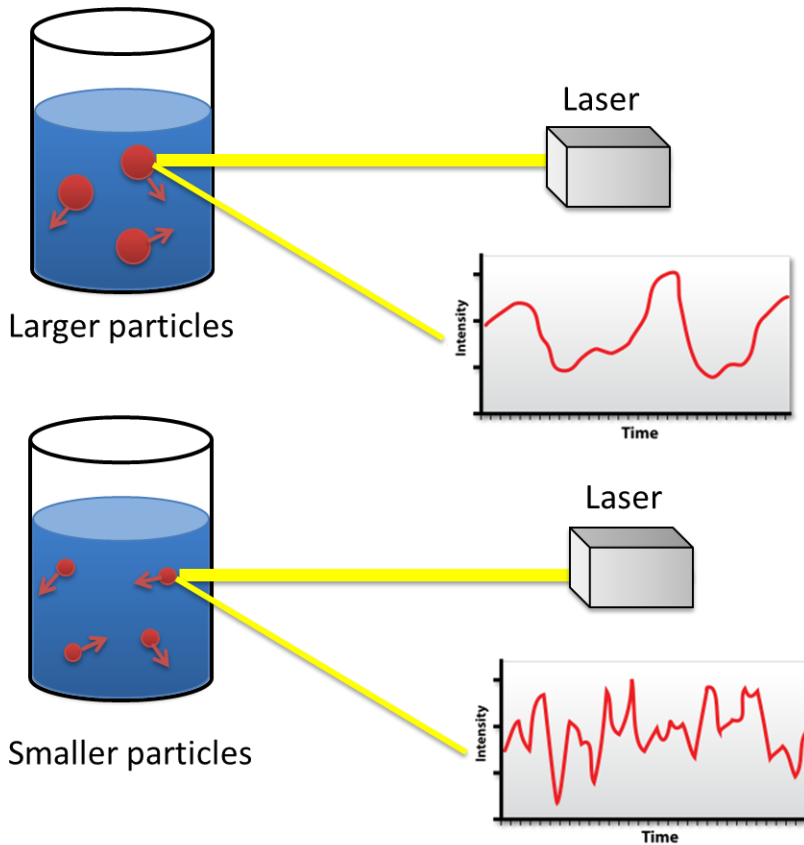
Scheme 4: Schematic configuration of a dynamic light scattering setup. Small particles bear a faster Brownian motion and therefore fluctuate stronger over time than larger particles.

Hence, DLS is a non-invasive method for measuring the size of particles in a submicron. The results of DLS measurements provide an intensity, number and volume weighted diameters of particles as well as a mean average of these three (D_I, D_N, D_V and D_Z, respectively) and a standard deviation which is given as the half-width at half height of a Gauss fitted size distribution. However, DLS is only accurate for round particles with a mono- or at least bimodal distribution. Additional sources of scattering, such as simple dust or proteins present in the solution (e.g. in DMEM with FCS) must be eliminated before measuring.

5.1.2 Zetapotential

There are two main forces that influence the stability of NPs in the aqueous solution: i) sterical hindrance, provided by the non-ionic surfactant such as Lutensol AT50, and ii) electrostatic repulsion, originated from the ionic groups of surfactants, e.g. CTMA-Cl. The layer around the particle, the so called electrical double layer, is composed of an inner region where ions are

strongly bound, called the Stern layer and an outer region, more diffuse layer. The potential that exists between those two regions is called the zeta potential, as is shown in Scheme 5.
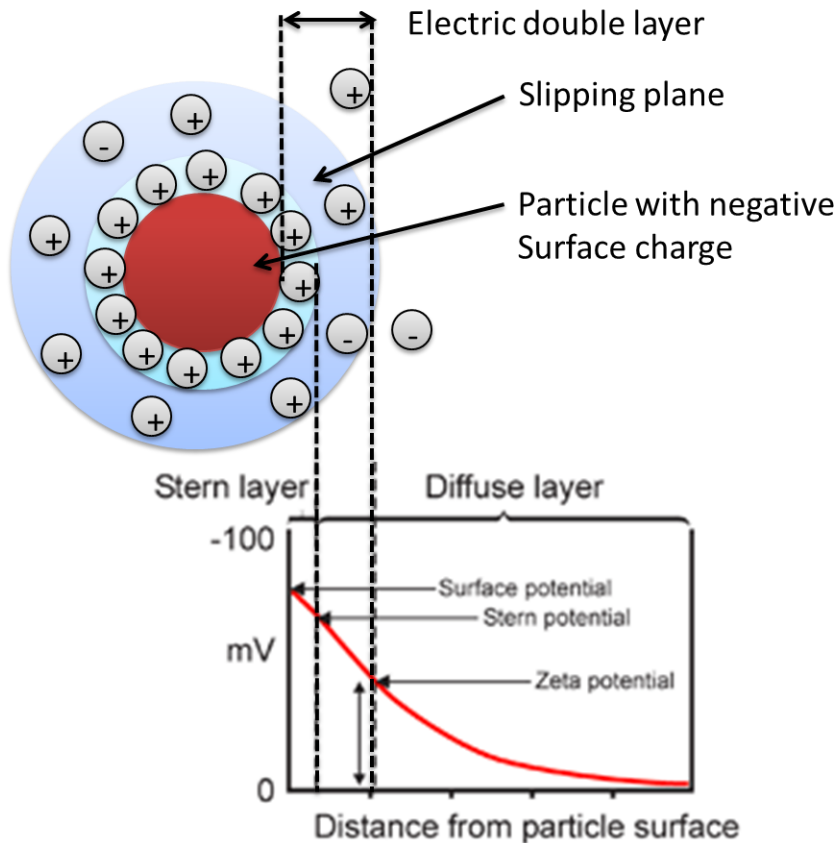
Scheme 5: Schematic charge distribution in a typical electric double layer around a negative charged particle in solution and the corresponding potentials.

When an electric field is applied on a NP dispersion, the charged particles move with a constant velocity towards the oppositely charged electrode. The zeta potential can be calculated from measuring this velocity, also called electrophoretic mobility U_E as it is dependent on the dielectric constant ε of the medium, the zeta potential ζ, a form function $f(Ka)$ called Henry's function and the viscosity of the medium η as given using the Henry equation:

$$U_E = \frac{2 \cdot \varepsilon \cdot \zeta \cdot f(Ka)}{3 \cdot \eta} \qquad (2).$$

The approximation of the Henry function is influenced by the concentration of electrolyte in the medium (Smulochowski approximation), hence measurements are performed in 10^{-3} M KCl solution [98].

The zeta potential gives a degree for the stability of the NPs and, if measured at the same pH value, a semi quantitative comparison for the amount of surface charged groups.

5.1.3 Polyelectrolyte titration

The exact amount of accessible charged groups per nm^2 or per particle is determined by titration with polyelectrolytes. The addition of polyelectrolytes in the NP dispersion causes the interaction of the polyelectrolyte with the charged groups on the NP surface till a net zero charge [99]. A typical polyelectrolyte for the determination of positive groups is sodium polyethylene sulfonate. The titration is quantified with a particle charge detector (PCD). A piston moves with a constant frequency within a cylinder that contains the sample, as can be seen in Scheme 6. The thus built up stream within an approx. 1 mm broad gap between piston and cylinder dismantles the light small counter ions from the polyions. The partial charge separation is measured by two electrodes. The titration is complete when the electric tension equals zero.
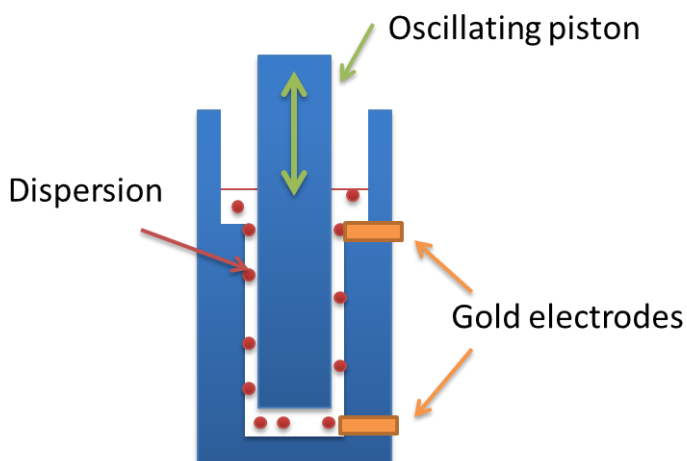
Scheme 6: Schematic setup of a particle charge detection measurement: a piston oscillates in a cylinder containing the sample. The electric tension is measured between two gold electrodes.

The amount of charged groups per particle and per nm^2 is calculated from the amount of consumed polyelectrolyte (as an average of three measurements) as follows:

$$\frac{Groups}{Particle} = \frac{V \cdot M \cdot N_A}{SC} \cdot \frac{\rho \cdot D_I^3 \cdot \pi}{6},$$
(3)

$$\frac{Groups}{nm^2} = \frac{V \cdot M \cdot N_A}{SC} \cdot \frac{\rho \cdot D_I^3 \cdot 10^{-18}}{6}.$$
(4)

The first term defines the amount of groups per $g_{Polymer}$, where V is the volume of consumed polyelectrolyte, M is the molar concentration of polyelectrolyte, N_A is Avogadro's constant $(6.022 \cdot 10^{23}\ mol \cdot l^{-1})$, SC is the solid content of the sample, D_I is the average diameter of the particle and ρ is the density of polystyrene $(1.045 \cdot 10^3\ g \cdot l^{-1})$ [100].

5.1.4 UV/Vis and fluorescence spectroscopy

After the synthesis of NPs, the fluorescence intensity varies between NP samples, and therefore need to be normalized in order to interpret the results of flow cytometry in a quantitative way.

The absolute amount of fluorescent dye is determined by UV/Vis spectroscopy. After dissolving the particles (with the incorporated dye) in THF, the absorption of the dye is measured in the UV/Vis range. The concentration of an absorbing species c is linear dependent on the absorbance E, as given by the Lambert-Beer law:

$$E = \varepsilon \cdot c \cdot d,$$
(5)

where ε is the absorption coefficient and d is the thickness of the cuvette under the condition of a non-turbid, homogeneous distributed sample in which absorbers act independently from each other and the incident light beam is preferably monochromatic [101]. A linear fitted calibration curve obtained in an experimental relevant concentration range, gives the total amount of fluorescent dye per $g_{Polymer}$. However, as the sample is dissolved in an organic solvent, the amount of dye per $g_{Polymer}$ does not necessarily equal to the fluorescence intensities as these can be influenced by intra-particle effects such as dye quenching or interaction of the dye with the polymer.

Fluorescence spectrometry of the NPs measured directly in dispersion yields the fluorescence signals with all of the above mentioned intra-particle effects. However, the absolute values regarding the incorporation yield of the dye cannot be given because no appropriate calibration exists. NP fluorescence intensities that are compared between the samples, which are adequate for normalizing flow cytometry data. The fluorescence intensity of three different NP dilutions is displayed over the solid content of NP dispersions. As fluorescence intensity, like absorption, is linear dependent on the concentration [102], the three values can be fitted linear. Fluorescence properties between NP samples could be compared from the obtained slope.

A comparison of the different schematic setups for absorption and fluorescence spectrometry is shown in Scheme 7.
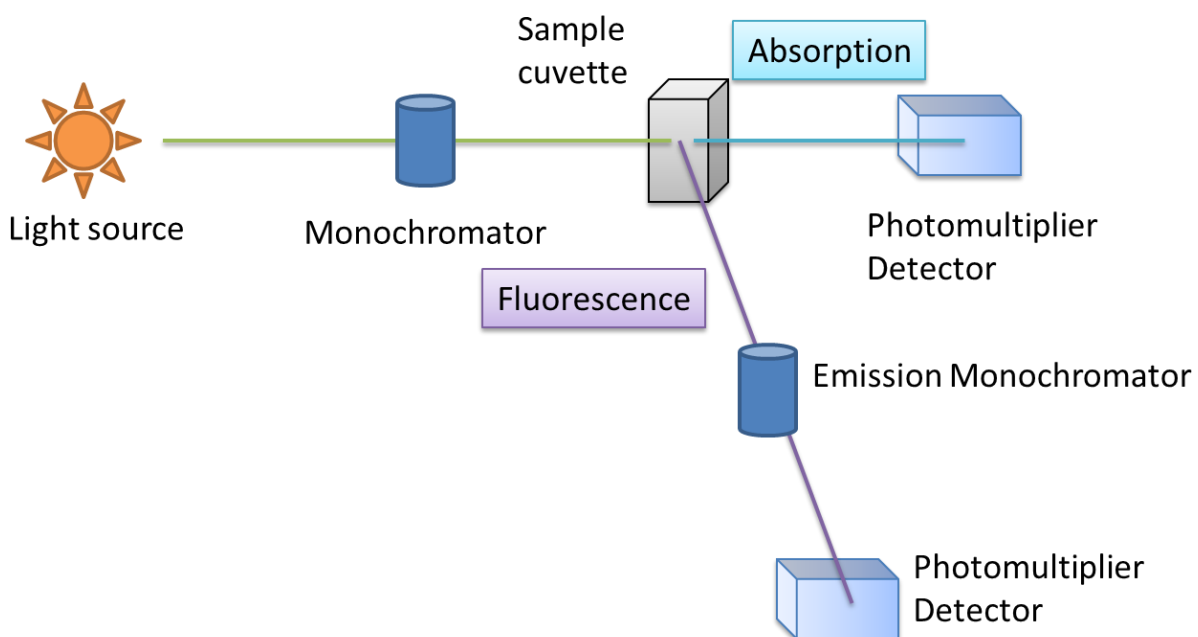
Scheme 7: Schematic setup of absorption and fluorescence spectrometry measurement. Absorption is measured at an 180 ° angle and fluorescence at an 90° angle.

5.1.5   Gel permeation chromatography

Gel permeation chromatography (GPC) separates analytes on the basis of their size and not on physical or chemical interaction with the column material. Hence it is often used to characterize

the molecular weight and the polydispersity index (PDI) of polymers. Smaller analytes travel slower across the column because they are held back by porous packing material [103].
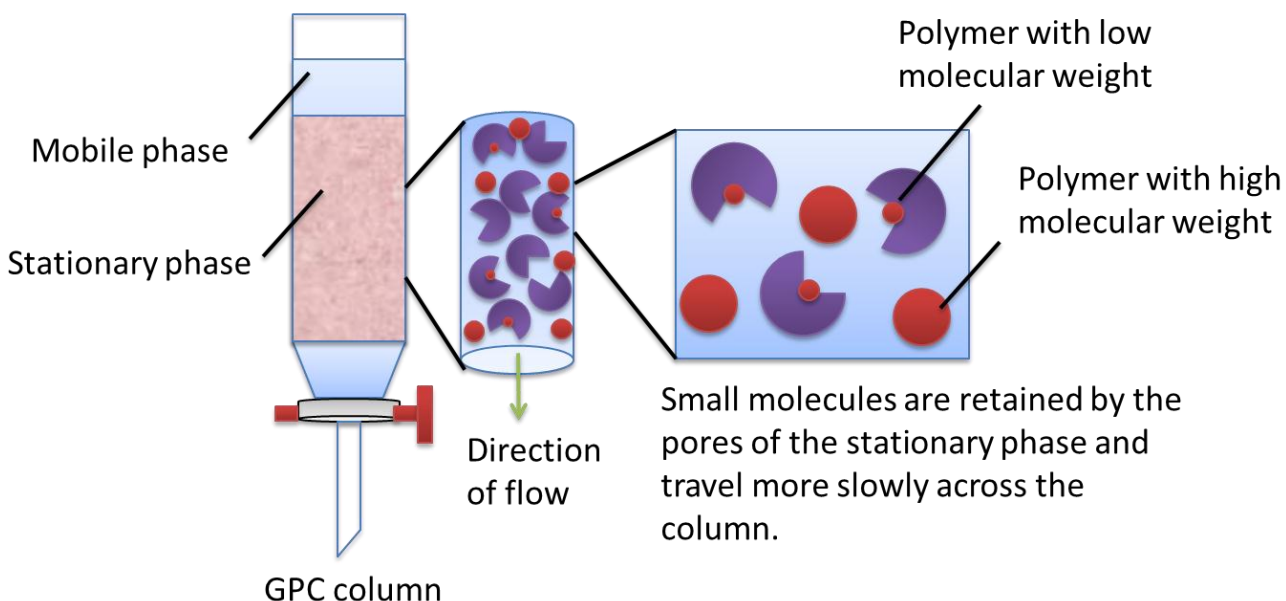
Scheme 8: Schematic setup of a GPC column: small molecules are retained by the pores of the stationary phase and travel more slowly across the column.

GPC can also be used for quantification [104] if the same amount of NP sample is applied to the column and an adequate calibration is performed. After dissolving polystyrene NPs stabilized with non-ionic surfactant Lutensol AT50 in THF, the signals from polystyrene and Lutensol AT50 are distinguishable in the GPC elugram. The calibration is performed with polystyrene and different amounts of Lutensol AT50. The percentage of the Lutensol AT50 peak integrals with respect to the polystyrene is displayed over the weighted percentage of Lutensol AT50. The thus obtained fit equation determines the percentage of Lutensol AT50 in relation to polystyrene in a NP sample. The amount of Lutensol AT50 per particle and nm^2 is calculated as follows:

$$Lutensol\ AT50\ per\ particle = Weight_{Particle} \cdot \%Lu =$$
$$= \frac{4}{3} \cdot \rho \cdot \pi \cdot r^3 \cdot \%Lu , \tag{6}$$

$$Lutensol\ AT50\ per\ nm^2 = \frac{Lutensol\ AT50\ per\ particle}{surface\ of\ particle} =$$

$$\frac{Lutensol\ AT50\ per\ particle}{4 \cdot \pi \cdot r^2}, \qquad\qquad (7)$$

where *%Lu* is the percentage of Lutensol AT50 as obtained by the calibration fit, *r* is the average half diameter of the NP sample as obtained from the DLS measurements and ρ is the density of polystyrene ($1.045 \cdot 10^6\ g \cdot l^{-1}$).

5.2   Analytical procedures for the interaction of NPs with cells

From the complexity of biological systems arises the need for a combination of advanced technologies as one method often addresses just one aspect of a given question, such as the interaction of NPs with cells. Hence, a combination of methods is necessary. For example, the uptake can be measured quantitatively with flow cytometry, but this method does not distinguish between particles taken up by the cell and those attached to the membrane. A supporting, qualitative method such as fluorescence microscopy needs to be performed additionally to address the experimental question. Mostly these methods include the use of fluorescence markers for the tagging of NPs and cellular compartments. Fluorescent labeling has several advantages, inter alia the detection of several markers at once even at low concentrations of dye-conjugates with a good signal to noise ratio (SNR). Flow cytometry, confocal laser scanning microscopy, immunecytochemical staining, immunofluorescence as well ion imaging use fluorescence as a means for detecting particles and cellular compartments and will be addressed in the following chapter.

In addition, electron microscopy was used to further increase the resolution to determine the subcellular localization of particles taken up by cells.

5.2.1   Flow cytometry

Flow cytometry allows the quantification of NPs associated to cells, which are defined by their size and granularity. Cells incubated with NPs and optionally labeled with a fluorescent antibody are separated by a constant sheath flow. Each object is detected individually in the cuvette with regard to their light scattering and fluorescent properties. Light scattered at a forward-bias, so called forward scatter (FSC), roughly correlates with the size of the object; sideward scattered light (SSC) is a unit for the granularity. In addition, the object's fluorescence with varying

excitation and emission wavelengths is collected. A schematic configuration of a typical flow cytometer is given in Scheme 9. In a typical fluorescent setup, three to six fluorescent channels (Fl1 – Fl6) are common.

By dot plotting the FCS, SSC or fluorescent channel of the cell antibody label it is possible to distinguish cells from cell fragments, dirt and single particles within the sample, as shown Figure 4 A and B. The cell signals are gated to the fluorescent channel histogram of the NPs (pink gate in Figure 4 A and B, gated signal histogram in Figure 4 D), which can then be quantified. Data are obtained as an average of three and a minimum of 20,000 cells per sample.
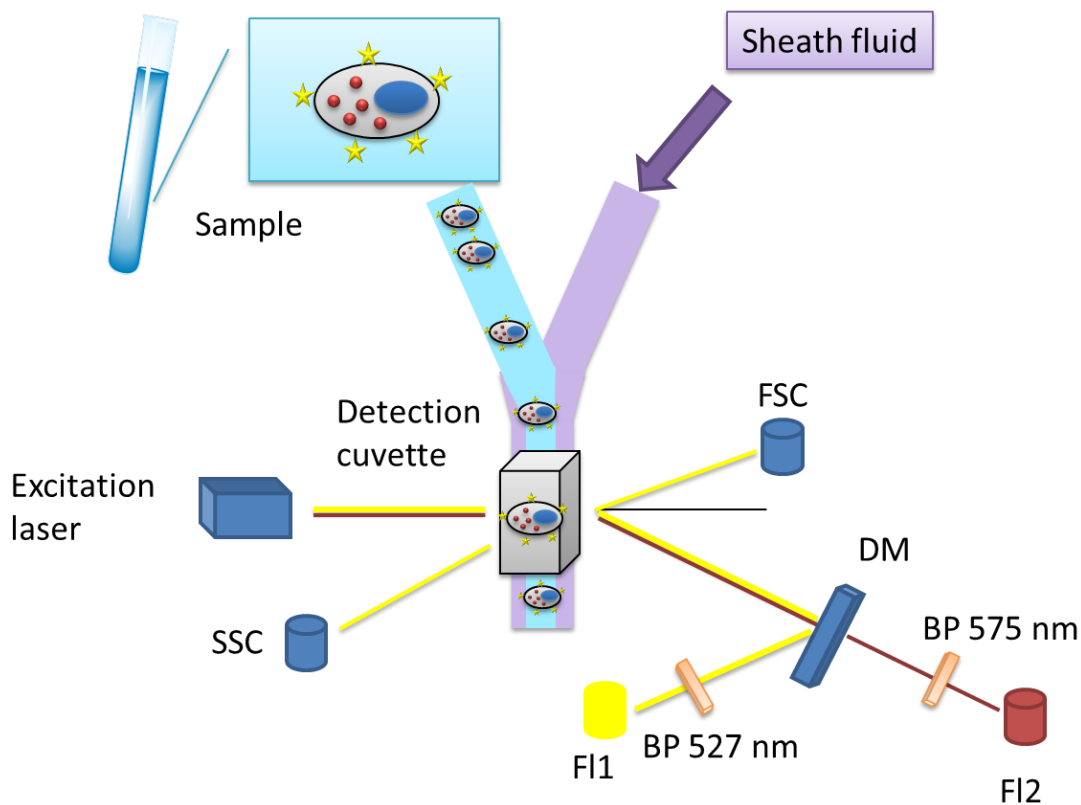
Scheme 9: Typical flow cytometer setup: a sample with NPs (red) incubated and antibody (yellow) labeled cells is diluted and enwrapped in a sheath fluid. Upon excitation in the detection cuvette, scattered and emission light is detected. FSC: forward scatter, SSC sideward scatter, Fl: fluorescent channel, DM: dichroic mirror, BP: band pass filter.
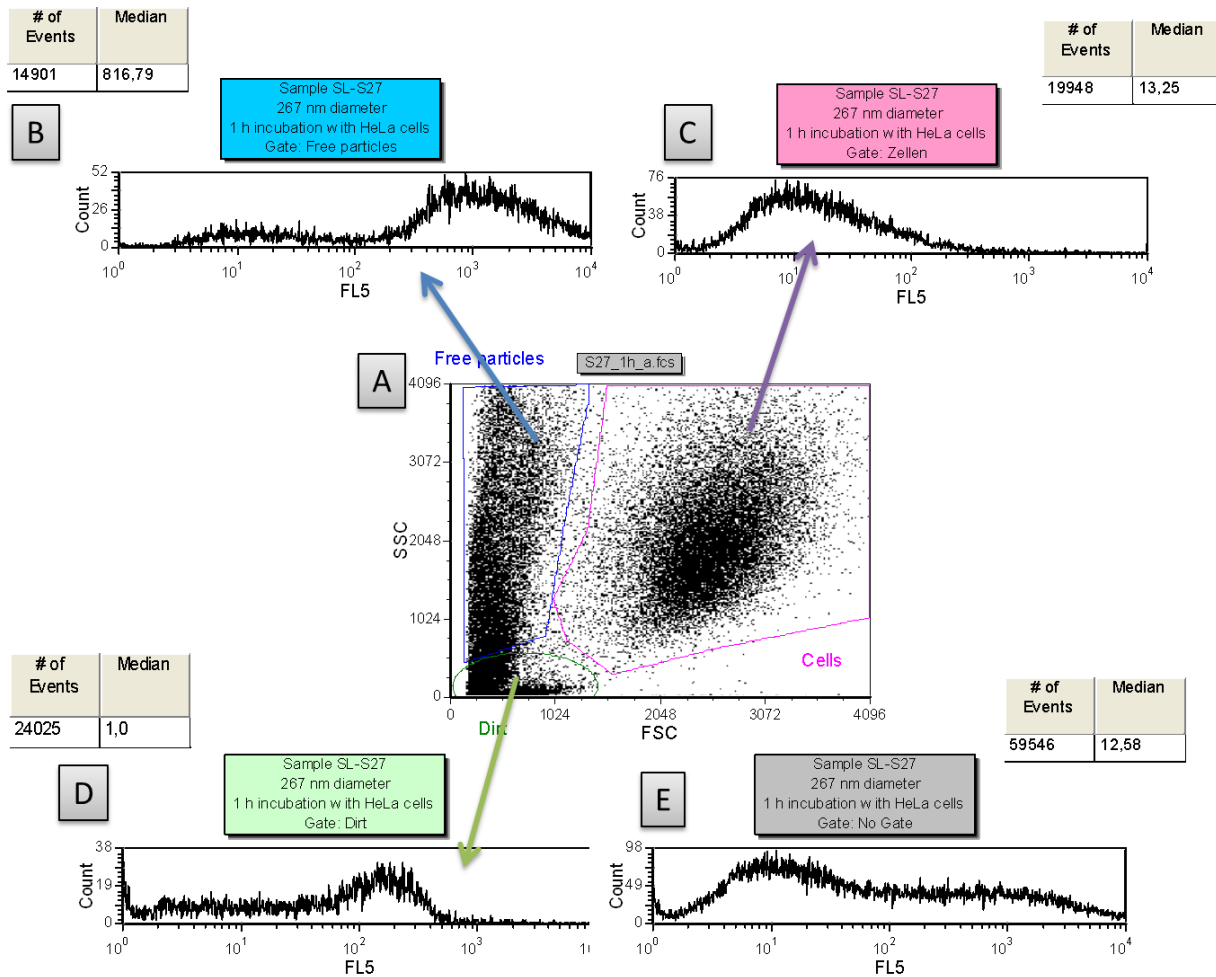
Figure 4: Flow cytometry data evaluation example of HeLa cells incubated with fluorescent NPs SL-S27 for 1 h at a concentration of 75 µg · ml-1. A: Dot plot of forward and sideward scatter with gated cells, free particles and dirt. B: Histogram of fluorescent channel 5 (Fl5) with gated particles. C: Histogram of fluorescent channel 5 (Fl5) with gated cells. D: Histogram of fluorescent channel 5 (Fl5) with gated dirt. E: fluorescent channel 5 (Fl5) with no gate (all events).

5.2.2 Confocal laser scanning microscopy

Flow cytometry gives quantified values of a fluorescent intensity correlated to cells. However, for a distinction between NPs taken up by cells or merely attached to the plasma membrane as well as intracellular localization of NPs microscopy techniques must be applied. In a typical confocal microscopy setup, the specimen is excited with a laser beam. The fluorescence signal travels through a pinhole that collects only light from a set confocal plane, as can be seen in Scheme 10A. In traditional widefield microscopy, excitation and emission of fluorescent molecules occurs and is collected throughout the sample, as shown in Scheme 10B. A limitation

of the illuminated (blue) and detected (red) emission maintains better resolution, SNR and limitation of photo damage. In confocal microscopy, only fluorophores within the XY-range, but throughout the optical z axis of the laser are excited. The detected emission is restricted by an additional pinhole in the emission beam path to the diffraction-limited volume of the focal spot [105].
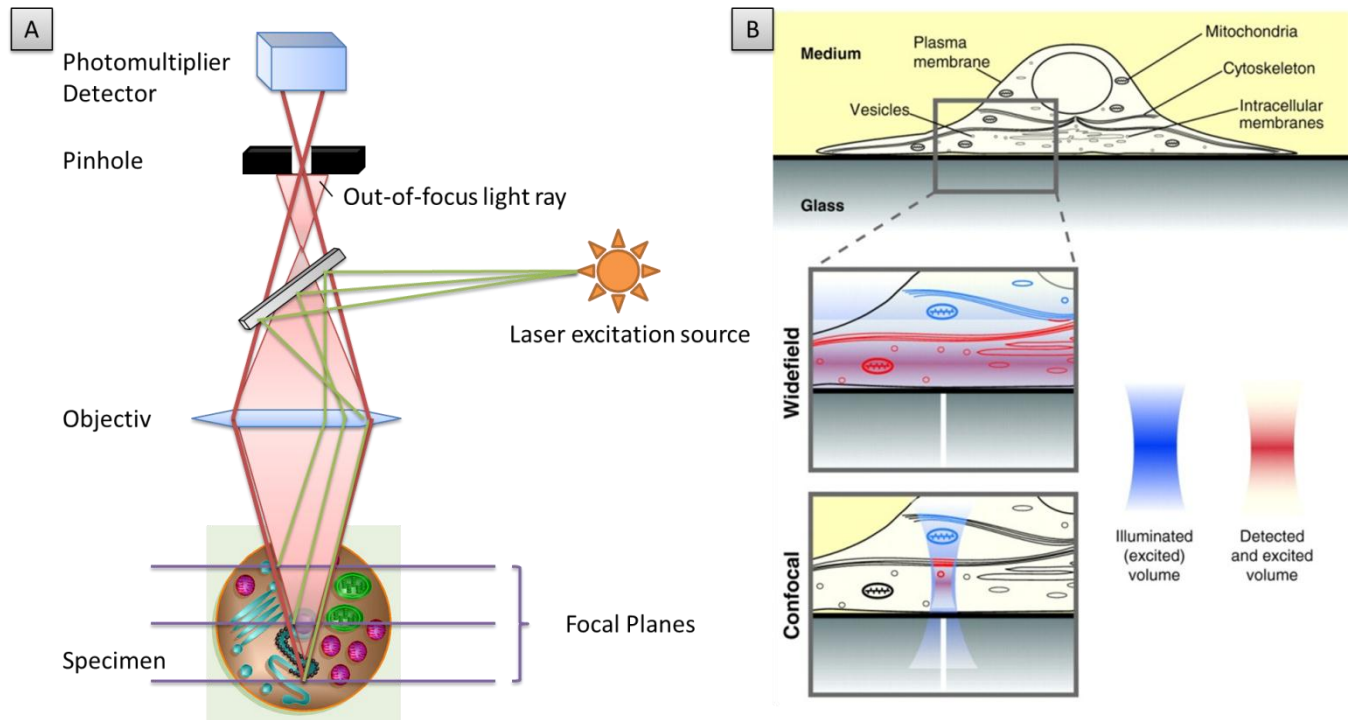
Scheme 10: A: Schematic optical path in confocal laser scanning microscopy. B: Comparison between the illumination upon excitation and emission detection of widefield and confocal microscopy for cellular imaging (adapted from and with permission of M. Cebecauer et al. [105]).

5.2.3 Electron microscopy and cryo-fixation

Imaging particles in the nanometer scale reaches the resolution limit of conventional microscopy. To determine the sub-cellular localization of particles taken up by cells, electron microscopy techniques are used. They lower the resolution in a way that cellular compartments can be distinguished and a more detailed localization of particles is possible. The maximum resolution of non-confocal microscopes is approx. 200 nm. By Abbe's law [106], the minimum resolution d_{min} is defined by the initial wavelength λ:

$$d_{min} \approx 0.61 \; \frac{\lambda}{NA}, \hspace{6cm} (8)$$

where *NA* is the numerical aperture of the lens. The wavelength of electrons is about 100,000 times shorter than that of visible light, which gives a maximum resolution of 50 pm [107].

Scanning electron microscopy (SEM) screens the surface of a sample. Upon interaction with the sample, electrons are scattered and loose energy. The so called secondary electrons are displayed in the SEM image. Transmission electron microscopy (TEM) images the transmission of an electron beam through a sample. Electrons are scattered at molecules or atoms with high atomic numbers or dense structures while they pass through areas with low atomic numbers.

The main drawback of electron microscopy is the need for a high vacuum in the electron path. Samples must be dry, tentatively stained and the images are only representative for a snap-shot. As polystyrene NPs consist of little amount of water, drying artifacts are minimized. However, when imaging cells a complex preparation procedure is required to prevent artifacts and to sustain cellular compartments and cell membranes.

To conserve the cellular structures, fixed cells are frozen under high pressure with liquid nitrogen to prevent the formation of ice crystals that destroy fragile membrane structures. To enhance contrast and sample stability, cells are stained with osmium tetroxide. The amorphous ice is replaced by a resin and the sample is cut ultrathin (70 – 100 nm). Cryo-fixation of cells and sample preparation for TEM imaging have been performed by Dr. Martin Dass.

5.2.4   *Blocking of endocytotic pathways with pharmacological inhibitors*

The direct probing of endocytotic pathways by pharmacological inhibitors is well established and has several advantages: the protocol is much simpler than that of more sophisticated molecular biological tools, all cells of a population are equally affected but side effects must be minimized due to a short incubation time. However, the main problem that undermines the use of pharmacological inhibitors is their questionable specificity for one endocytotic pathway, esp. pathways that have not been described to a full extent yet.

A variety of inhibitors is used to probe endocytotic mechanisms. Chlorpromazine is a cationic amphiphatic inhibitor for clathrin-mediated endocytosis [48, 108]. In addition, several publications indicate that chlorpromazine also affects the formation of phagosomes and macropinosomes due to incorporation into the cell membrane [49, 108, 109] and may not be efficient in all cell types [110]. Cytochalasin D blocks actin formation by occupying a faster-growing "barbed" end of actin filaments [111, 112] thus inhibiting macropinocytosis and phagocytosis. However, actin has been reported to participate in several other uptake mechanisms, like clathrin-mediated endocytosis and caveolin-mediated endocytosis [43-46, 113, 114]. Cytochalasin must be considered as a global, nonselective inhibitor of all internalization pathways. The amiloride derivate EIPA was shown to effectively block macropinocytosis and phagocytosis in mammalian cells [115]. EIPA reportedly also disturbs clathrin-mediated endocytosis [116] and CDC42-mediated endocytosis [117] and alters the morphology and intracellular distribution of early and late endosomes [118]. Dynasore effectively inhibits dynamin-dependent endocytosis [39, 119], however that includes several endocytotic pathways (see Scheme 2). Table 1 gives an overview over the inhibitors and their pitfalls.

Table 1: Overview of pharmacological inhibitors and their main drawbacks.

Agent	Inhibitor of	Endocytotic pathway	Drawback
Chlorpromazine	Rho GTPase	Clathrin-mediated endocytosis	May also affect formation of phagosomes and macropinosomes; dependent on cell type.
Cytochalasin D	Actin formation	Macropinocytosis and others	Global inhibitor for endocytotic processes; no specificity
EIPA	Sodium-proton exchange, thus lowering submembraneous pH	Macropinocytosis	May effect clathrin-mediated endocytosis, CDC42-mediated endocytosis and disturbs endosomal morphology and distribution
Dynasore	Dynamin	Several mechanisms	Global inhibitor for dynamin-dependent endocytosis; no specificity

5.2.5 *Quantitative immunecytochemical staining and immunofluorescence*

To distinguish between intracellular structures or compartments in cLSM, proteins and antigens of interest are labeled with antibodies by immunocytochemical staining (ICS). A colocalization between the fluorescent tagged antigen and the NPs, detects the intracellular localization and interaction of NPs with cellular processes. It is possible to distinguish endo-lysosomal structures within the cell and to assign them to the NPs. A huge variety of useful antibodies is available. However, there are several problems that inflict this technique: cells must be fixed before staining, which can affect intracellular structures; nonspecific clusters of NPs or antibodies can lead to false positive results; colocalization can also be due to structures being in close proximity instead of real interaction and a sample only reveals the data of a few cells at one certain time.
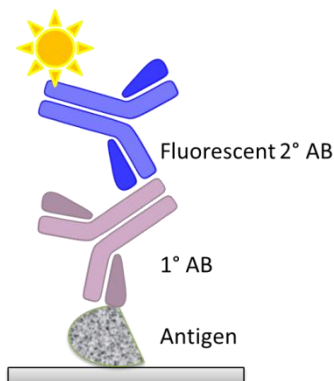
In ICS, fixed cells are treated with a surfactant to perforate the plasma membrane for the antibodies. Vesicles and other lipid structures are prone to disrupt if perforation procedure is performed negligent. In direct ICS, cells are stained with a single fluorescent antibody. To increase the SNR, in indirect ICS a non-fluorescent primary antibody is labeled with several fluorescent secondary antibodies (Scheme 11).

Scheme 11: In indirect immunocytochemical staining (ICS), the antigen is labeled with a non-fluorescent primary antibody which is then stained with a fluorescent secondary antibody. AB: Antibody.

Cells can express green fluorescent protein (GFP) tagged endocytotic proteins via the transfection of constructs to detect colocalization with NPs. The disturbance to the general cellular system is much less than the use of histological staining. However, the function of proteins may be altered by the GFP-tagging and expression of the protein may increase upon transfection, which leads to unwanted lower-affinity side effects. For example, the construct cav1-EGFP results in a fully functional fluorescent cav1, whereas EGFP-cav1 transcripts for a cav1 knock-down mutant [120]. For immunofluorescence, HeLa cells are transfected with a plasmid that contains a DNA construct that codes for EGFP-tagged caveolin. As both the plasmid DNA and the cell membrane bear a negative net charge, a transfection agent is used to overcome the cell membrane barrier. Transfected cells express the fluorescent protein and can easily be detected in fluorescence microscopy.

ICS and immunofluorescence must allow for a statement if two objects, i.e. a protein and a NP, reside at the same spatial localization or volume of interest. The main limitation for this statement is the resolution of the confocal microscope, which is defined by Abbé's law (see chapter 5.2.3). In a best case scenario, one can only say if two objects occupy approx. the same 130 x 130 x 300 nm volume, or voxel, when images are in confocal mode measured at an excitation wavelength of 500 nm. A qualitative analysis draws upon a color overlap of two channels, e.g. green and red with a yellow overlap. However, the amount of yellow is extremely

susceptible and depends on external factors, esp. those that modify the intensity histogram of the image.

Before detecting colocalization, typical sources for errors must be eliminated. Background correction to purge false-positive signals from background noise by setting the threshold must be done with care, as this step is prone to bias. Cross-talk must be minimized by accurately setting the hardware with the use of negative controls. Also, the imbalance between lateral and axial resolution will distort a round-shaped object along the z-axis. Therefore, any colocalization must be carried out in three dimensions.

Several approaches are known to quantify the colocalization. Most commonly, the Pearson's correlation factor R_R is calculated:

$$R_R = \frac{\sum (R_i - \bar{R}) \cdot (G_i - \bar{G})}{\sqrt{(R_i - \bar{R})^2 \cdot (G_i - \bar{G})^2}}, \qquad\qquad (9)$$

for i pixel in the image; R and G are intensities of the red and green channel, respectively. The Pearson coefficient gives values between 1 and -1, where 1 is perfect correlation. However, perfect exclusion does not necessarily give values of -1. Pearson coefficients with low or negative values are hard to interpret. As it is expected that NPs colocalize at best partially with endocytotic proteins (if at all), the Pearson correlation factor should not be applied.

The overlap coefficient R is easier to understand than the Pearson coefficient. It ranges between 1 and 0 or between 100 and 0%, with 1 and 100% being perfect colocalization:

$$R = \frac{\sum_i (R_i \cdot G_i)}{\sqrt{\sum_i (R_i)^2 \cdot \sum_i (G_i)^2}}, \qquad\qquad (10)$$

for i pixel in the image; R and G are intensities of the red and green channel, respectively. The overlap coefficient can only be applied when the numbers of green and red pixels are approx. the same. With ICS, a lot more green pixels representing the endosomal marker proteins are present in the images and it is concluded that the overlap coefficient cannot be used either.

A rather new approach called the intensity correlation quotient (ICQ) is given by Li [121]: If the intensities in two images vary in synchrony (i.e. they are dependent), they will vary around their

respective mean image intensities together. In an image where the intensities vary together, the product of the differences from the mean (PDM) will be positive and vice versa:

$$PDM = (R_i - \bar{R}) \cdot (G_i - \bar{G}) , \tag{11}$$

$$ICQ = \left(\frac{N_{+ve}}{N_{total}}\right) - 0.5 , \tag{12}$$

for i pixel in the image, R and G are the respective intensities in the red and green channel, PDM is the product of differences from the mean for each channel, N_{+ve} is the number of positive values for PDM and N_{total} the total number of pixels that do not have a value of zero in each channel. The ICQ values lie between -0.5 (segregated) and 0.5 (dependent staining). It is not prone to the numbers of red and green pixels and has not been reported a stable method for complete exclusion [122].

Biological images are impaired with noise, aggregates of NPs or antibodies and so on. Therefore, to ensure accurate statements, the ICQ value is given as a mean of min. 3 regions of interest that include only and exclusively a part of the cell, for the same lower threshold settings and for a three-dimensional z-stack. The ICQs are calculated with adjustable threshold by the ImageJ plugin JACoP (jet another colocalization plugin).

However, the ICQ value only gives an overview of the ROI selected. As a more differentiated way of data interpretation, the PDM plot is also taken into consideration. For PDM plots, the products of the differences from the mean for both channels are plotted against the intensity of each channel, thus giving a green and red PDM plot. If the PDM values are centered at zero and bear an hourglass shape plot, i.e. given an ICQ of 0, random staining is present in the sample. A true colocalization results not only in positive PDM values but also in a typical exponential plot shape. Figure 5 shows constructed examples of three different colocalization possibilities. As can be seen, the ICQ value does not necessarily reflect the true relations. For example, 100% colocalization with only little green staining leads to an ICQ value of -0.085. However, the colocalisation is clearly detectable from the shape of the PDM plots.
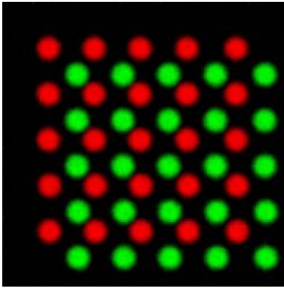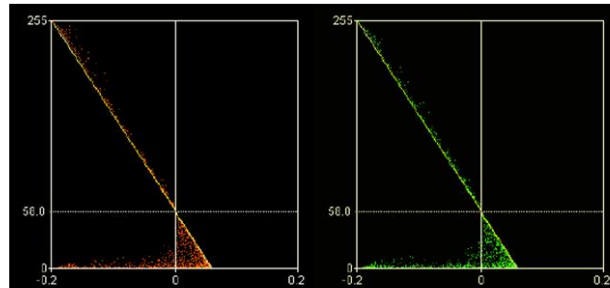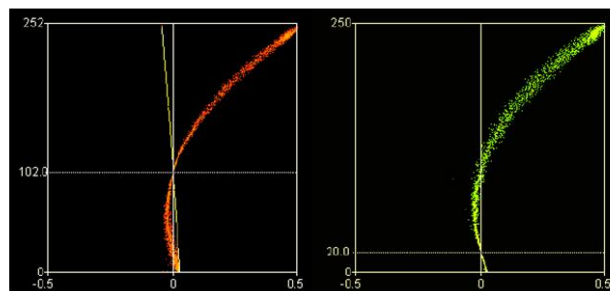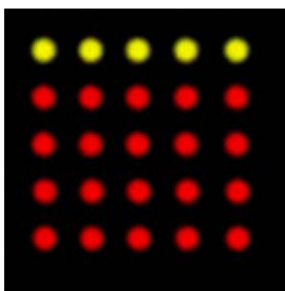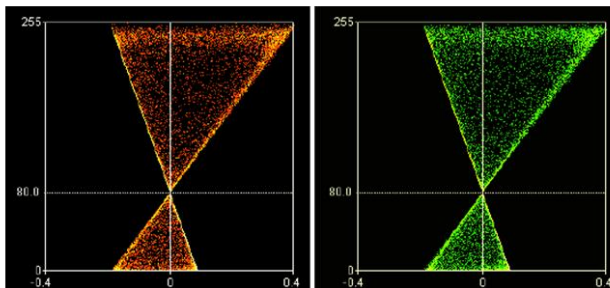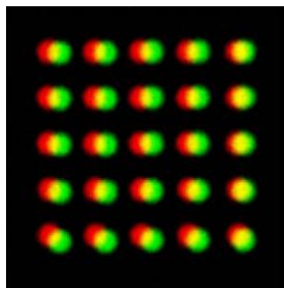
Figure 5: Constructed examples of exclusion, complete and random colocalization with the corresponding ICQ values. A: Original image; B: PDM plot for the red and green channel (adapted from and with permission of T. Collins [123].

5.2.6   Live cell pH imaging

Most commonly, ion detection in cells is performed with the use of ion sensitive fluorophores. These molecules change their excitation and/or emission properties in the presence of the analyte. These sensors fall into two operational classes: single wavelength (SW) and ratiometric fluorophores. For SW indicators, the fluorescence intensity is dependent on the concentration of the analyte, where the spectral maxima remain unchanged. Ratiometric indicators not only

exhibit intensity changes in the presence of different concentrations of analyte, but they also undergo a shift of the spectral maxima from unbound to bound indicator. SW sensors need to be elaborately calibrated according to their local concentration. Ratiometric indicators are independent of their concentration as the concentration of the analyte is a function of the ratio of the bound to the unbound spectral maxima.

As the ratio is altered in the presence of cellular constituents [124], an intracellular calibration needs to be performed. The most common ion analytes are water-soluble and cannot cross the cell membrane [125]. However, ester forms of the dye are hydrophobic enough to pass the membrane. They are cleaved to the free dye form by intracellular esterases and thus trapped in the cytoplasm. Several factors influence the efficiency and quality of acetoxymethyl (AM) ester loading. AM esters are large, unipolar molecules and hence poorly soluble in water or in the cellular medium. An addition of the ester at the solubility limit might lead to precipitation of the dye, which is then unavailable for the uptake to cells. A convenient method to increase the solubility of the indicator is the pre-incubation with FCS. The proteins are presumed to sequester the AM ester, thus preventing precipitation and the aggregates formed are presumed to serve as a steady source for the uptake. The net result is a significantly increased loading of indicator into cells. AM esters can also be taken up by endocytosis or enter subcompartments like endo-lysosomal vesicles, the ER etc. by diffusion, where they are cleaved and trapped. As endocytosis is an energy-dependent process, loading of cells with the ester at RT decreases the amount of take taken up into the endo-lysosomal compartment. This procedure also lowers the cleavage activity of the cytoplasmatic esterases. On that account, the loading process is followed by an additional incubation at 37 °C. For our purpose, the AM ester is loaded into cells only for calibration reasons and the ionophores used to equilibrate the extracellular and intracellular pH also affect vesicles and intracellular compartments [126]. A quantification of dye present in the cytoplasm or cellular compartments is not necessary. A value of 10% for compartimented dye is typical [125]. However, as the AM ester is only used for calibration in the presence of ionophores, this does not affect the experiment as it would e.g. intracellular pH measurements. The dye is not completely trapped within the cells but leaks out at a certain speed. In addition, the toxic effect of the ionophores perforates the plasma membrane which

leads to a fast disposition of the dye into the medium. Cells are imaged as fast as possible after loading with dye and addition of ionophores.

5.2.7   Image batch processing

Image processing is an important part when dealing with quantitative ion sensing. As with ICS, appropriate threshold settings must be applied and is prone to bias. In this work, the threshold is applied only to the ratio image to avoid disturbance of the original data. In addition, cell imaging over a long time period produces a large number of images which cannot be processed by hand. To display a movie which shows in a pseudo-colored image the pH changes over a long time period (i.e. one hour), a batch program has been written that executes an ImageJ macro for each set of images per time. The macro conducts the following processing steps:

- Open images for protonated and deprotonated form at one time point;
- Subtraction of background for both channels;
- Ratio image of channels;
- Create threshold image for a duplicate of channel 1 and divide with 255 to create a mask image with only 1 and 0 values;
- Multiply ratio image with mask to reduce background noise;
- Apply binominal fit function as determined by intracellular calibration;
- Set min / max values and appropriate LUT;
- Save and open new image set.

5.3   Materials, devices, chemicals and consumables

Styrene was distilled under reduced pressure and stored at -20 °C before use. All other chemicals were used without further purification. Demineralized (demin.) water was employed throughout the experiments. A list of all chemicals with the according manufacturers and purity grade, as far as they are known, is given in Table 2 for NP synthesis and for cellular applications.

Table 2: Chemicals and materials used for NP synthesis and characterization.

Notation	Abbre-viation	Application	Manufacturer
(1-Hexadecyl)-trimethylammonium-chloride	CTMA-Cl	Cationic surfactant	Alfa Aesar, USA
1-Ethyl-3-(3-dimethylaminopropyl)-carbodiimid	EDC	Coupling reagent for the synthesis of carboxamides	Alfa Aesar, USA
1-Hydroxybenzotriazole hydrate, > 98%	HOBt	EDC coupling co-reagent	Sigma-Aldrich, USA
2,-2'-Azobis(2-methylbutyronitrile)	V59	Oil soluble initiator	Wako chemicals, Japan
2-Aminoethyl methacrylate hydrochloride, 90%	AEMH	Amino funct. comonomer	Sigma-Aldrich, USA
2,2'-Azobis(2-methylpropionamidinbe)dihydrochloride	V50	Water soluble initiator	Wako chemicals, Japan
Ethanol, p.a.	EtOH	Solvent	Merck, Germany
Hexadecane	HD	Ultrahydrophobe	Sigma-Aldrich, USA
Lutensol AT50 and AT80		Non-ionic surfactants	BASF, Germany
N,N-Bis(2,6-diisopropylphenyl-)1,6,7,12-tetraphenoxyperylene-3,4,9,10-tetracarboxdiimide	Lumogen F Red	Perylene dye	BASF, Germany
Polystyrene, M = 14,300		Standard in quantitative GPC analysis	Synthesized by Thomas Wagner (MPI-P, Germany)
Styrene, 99%		Monomer	Merck, Germany

Table 3: Chemicals and materials used for cell culture and application.

Notation	Abbre-viation	Application	Manufacturer
(3-(4,5-Dimethylthiazol-2-yl)-5-(3-carboxymethoxyphenyl)-2-(4-sulfophenyl)-2H-tetrazolium)	MTS	Toxicity measurement	Promega, USA
1,4-Piperazinediethane-sulfonic acid, 99%	Pipes	Buffer	Sigma, Germany
2-(N-morpholino)-ethanesulfonic acid	MES	Buffer	Sigma, Germany
4-(2-Hydroxyethyl-)piper-azine-1-ethanesulfonic acid, 99%	HEPES	Buffer	Merck, Germany
5-(N-Ethyl-N-isopropyl)amilorid	EIPA	Endocytosis inhibitor	Sigma, Germany
7-Aminoactinomycin	7-AAD	Toxicity measurement	Sigma, Germany and Alexis Biochemicals, Switzerland
Albumine from bovine serum cohn fraction V, lyphilised powder, 96%	BSA	Buffer	Sigma, Germany
Anti CatD		Antibody for cathepsin D	BD Bioscience, USA
Anti Cav-1		Antibody for caveolin-1	Santa Cruz, USA
Anti CD55/FITC		FITC-labeled antibody for CD55	Ancell, USA
Anti clat		Antibody for clathrin heavy chain	BD Bioscience, USA

Table 3: Chemicals and materials used for cell culture and application (continued).

Notation	Abbre-viation	Application	Manufacturer
Anti DNM2		Antibody for dynamin-2	Antibodies-online, Germany
Anti EEA1		Antibody for early endosome antigen-1	BD Bioscience, USA
Anti Lamp1		Antibody for lysosomal associated protein 1	BD Bioscience, USA
Anti M6P		Antibody for mannose-6 phosphate receptor	Merck, Germany
Bicin, 99%		Buffer	AppliChem, Germany
CellMask^{TM}		Membrane dyes	Invitrogen, Germany
Chlorpromazine hydrochloride		Endocytosis inhibitor	Sigma, Germany
Cytochalasine D		Endocytosis inhibitor	Sigma, Germany
DiD		Membrane dye	Invitrogen, Germany
DNA constructs	CE, EC	Transfection construct	Gilles Spoden, Uniklinik Mainz, Germany
Donkey anti-rabbit/Alexa488		Alexa488-labeled 2AK	Invitrogen, Germany
DRAQ5		Cell nucleus stain	Biostatus Limited, United Kingdom
Dulbecco's modified eagle medium with 2 mM L-glutamine and 10% FCS (if not otherwise stated)	DMEM	Cell medium	Invitrogen, Germany

Table 3: Chemicals and materials used for cell culture and application (continued).

Notation	Abbre-viation	Application	Manufacturer
Dulbecco's phosphate buffered saline with additional calcium and magnesia	PBS$^+$	Buffer	Invitrogen, Germany
Dulbecco's phosphate buffered saline, without additional calcium and magnesia	PBS	Buffer	Invitrogen, Germany
Dynasore		Endocytosis inhibitor	Sigma, Germany
EPON$^®$		Fixation resin	Sigma-Aldrich, USA
Ethylene glycol-bis(2-amino-ethylether)-NN,N',N'-tetraacetic acid	EGTA	Buffer	Sigma, Germany
Fetal calf serum	FCS	Cell culture	Invitrogen, Germany
Fluoromount G		Mounting medium	Southern Biotech, USA
Fugene HD		Transfection agent	Promega, USA
Goat anti-mouse/Alexa488		Alexa488-labeled 2AK	Invitrogen, Germany
Human serum	HS	Coagulation study	Blutspendezentrale Mainz, Germany
Nigericin, free acid		Ionophore	Invitrogen, Germany
Osmiuumtetroxide	OsO$_4$	Staining reagent	Carl Roth, Germany
Paraformaldehyde, 95%	PFA	Fixation agent	Sigma-Aldrich, USA
Penicillin		Cell culture	Invitrogen, Germany
Polytheylene glycol, M = 8,000	PEG	Buffer	Sigma, Germany

Table 3: Chemicals and materials used for cell culture and application (continued).

Notation	Abbre-viation	Application	Manufacturer
SNARF-4F		pH-sensitive fluorescent dye	Invitrogen, Germany
SNARF-4F AM ester		pH-sensitive cell permeable dye	Invitrogen, Germany
Streptomycin		Cell culture	Invitrogen, Germany
t-Octylphenoxy-polyethylethanol	Triton X-100	Permeabilisation agent	Sigma, Germany
Trypsin		Cell culture	Invitrogen, Germany
Uranylacetate		Staining agent	Riedel-de Haën, Germany
Valinomycin		Ionophore	Invitrogen, Germany

Table 4 displays the devices used in this work.

Table 4: Devices.

Notification	Abbre-viation	Application	Type and Manufacturer
-80° Freezer		Cell culture	Thermo Scientific, Germany
Absorption spectroscope	UV/Vis		Lambda 25, Perkin Elmer, USA
Cell counter			TC10, Bio-Rad, USA
Centrifuge			5810R and 5430, Eppendorf, Germany
Confocal laser scanning microscopy	cLSM	Cell imaging	Leica SP5 II, Leica, Germany
Dynamic light scattering	DLS	Particle size	Nicomp 380 Submicron Particle Sizer, Nicomp Particle Sizing Systems, USA
FCSExpress		Software for flow cytometry	De Novo, USA
Flow		Cell culture	S@fermate 1.2, Bioair, Italy and c-(Max Pro)^3-130, Berner, Germany
Flow cytometer		Quantification of NP uptake	CyFlow ML with FloMax Software, Partec, Germany
Fluorescence spectroscope			TIDAS FL3095 SL, J&M, Spectralytics, Germany
Gel permeation chromatographe	GPC	Amount of surface Lutensol AT50 and M_w measurement	SDV column, detectors ERC RI-101 and UV S-3702 with PSS-WinGPC Unity software, PSS, Germany
Incubator		Cell culture	Heraeus Instruments, Germany

Table 4: Devices (continued).

Notification	Abbre-viation	Application	Type and Manufacturer
Inverse sonifier		Redispersion	Branson, USA
Inverted microscope		Cell culture	CKX41, Olympus, Germany
Non-confocal fluorescence microscope		NP flocculation test	IX-70, Olympus, Germany
Particle charge detection	PCD	Amount of charged surface groups	PCD 02, Mütek GmbH, Germany with a Titrino Automatic Titrator, Metrohm AG, Switzerland
Platereader		Absorption and fluorescence measurements in well plates	Infinite M1000 with software i-control 1.6.19.0, Tecan, Germany
Raster electron microscopy	REM	Particle morphology	Leo Gemini, Zeiss, Jena, Germany
Sonic bath		Redispersion	Bandelin Electronic, Germany
Sonifier		Miniemulsion polymerization	Branson sonifier W450 digital ½" tip, Branson, USA
Transmission electron microscopy	TEM	Particle morphology	Zeiss 902, Zeiss, Jena, Germany
Zetapotential measurement			Zetasizer, Malvern, United Kingdom
GPC detector		Detection of molecules eluting from the GPC column	ERC RI-101 and UV S-3702, Soma, Japan
GPC software			PSS-WinGPC Unity, PSS, Germany

A list of consumables is given in Table 5.

Table 5: Consumables.

Notification	Application	Manufacturer
24well plate, black, clear bottom	Cell culture, platereader fluorescence measurements	Porvair Science, United Kingdom
4'' silicon wafer	SEM imaging	Ted-Pella, USA
6well plate	Cell culture	Nunc, Germany and Greiner Bio-one, Germany
96well plate, black, clear bottom	Cell culture, platereader fluorescence and absorption measurements	Corning, USA
Cellulose dialysis tube *Visking*, Cut-off 14,000	Dialysis of ionic stabilized NPs	Carl Roth, Germany
Labtek II 8well, cell culture treated or untreated	Cell culture, cLSM imaging	Nunc, Germany
Labtek II chamber slide, 8well	Cell culture, cLSM imaging	Nunc, Germany
Tissue culture cell star	Bottles for cell culture	Greiner Bio-one, Germany

5.4 Experimental specifications

5.4.1 Non-ionic particles with different sizes

Fluorescent polystyrene particles stabilized with the non-ionic surfactant Lutensol AT50 and having diameters in the range between 130 and 890 nm were synthesized via dispersion polymerization. Briefly, 6 g styrene, 0.1 g oil-soluble initiator V59, 0.004 g fluorescent dye (Lumogen F Red), 15 g demin. water, 9 g EtOH and different amounts of Lutensol AT50 were mixed together and stirred at 500 rpm for 20 min under argon atmosphere. After that the temperature was increased till 72 °C and the polymerization proceeds for 20 h under magnetic stirring.

5.4.2 Synthesis of cationic polystyrene particles with different sizes

Positively charged fluorescent particles with the diameter of 120 nm were synthesized using the miniemulsion polymerization in the presence of cationic surfactant CTMA-Cl. The disperse phase consisting of 6 g styrene, 0.25 g HD and 0.004 mg Lumogen F Red was mixed with the aqueous phase containing 24 g demin. water, 0.1 g water-soluble initiator V50 and 100 mg CTMA-Cl. The mixture was stirred for 1 h at 1,000 rpm and then sonicated under ice cooling for 120 s at 90%. The polymerization proceeds for 20 h at 72 °C under magnetic stirring.

Positively charged fluorescent particles with a diameter bigger than 120 nm were synthesized by seed polymerization. Polystyrene seed particles with the diameter of 120 nm were synthesized by miniemulsion process as described above with only the difference that 40 mg instead of 4 mg Lumogen F Red was used. For seed polymerization, 48 ml of 0.1% seed particles were mixed with different amounts of CTMA-Cl. The mixture was purged with argon and stirred for 15 min at 72 °C. After that, the water-soluble initiator V50 dissolved in 2 ml water was added to the mixture and after 5 min of stirring a 30 – 200 times excess of styrene with respect to the amount of seed particles was introduced at a rate of $1 \ ml \cdot h^{-1}$ using a syringe pump. Upon the monomer addition and during the whole reaction time the mixture was magnetically stirred at 700 rpm for 20 h at 72 °C.

5.4.3 Amino-functionalized particles for the immobilization of SNARF-4F

Fluorescent amino-functionalized polystyrene particles were synthesized using the miniemulsion polymerization in the presence of the amino functionalized comonomer AEMH and the non-ionic surfactant Lutensol AT80. The disperse phase consisting of 5.7 styrene, 0.1 g oil-soluble initiator V59 and 0.25 g HD was mixed with the aqueous phase containing 0.3 g AEMH, 24 g demin. water and 0.2 g Lutensol AT80. The mixture was stirred for 1 h and then sonicated under ice cooling for 120 s at 90%. The polymerization proceeds for 20 h at 72 °C under magnetic stirring.

5.4.4 Nanoparticle characterization

After synthesis, prior any characterization all latexes synthesized in the presence of non-ionic surfactant were purified with demin. water via repetitive centrifugation/redispersion at 20,800 x g for 25 min. Particles synthesized in the presence of CTMA-Cl were dialyzed using a cellulose dialysis membrane until the conductivity of the water reaches a constant value of 8 $\mu S \cdot m^{-1}$.

 After purification, the particles were characterized with respect to their average size, size distribution, zeta potential, concentration of surface functional groups, molecular weight, amount of incorporated dye, morphology, fluorescence intensity and stability in physiological media.

The particle size was measured with dynamic light scattering at 20 °C and a scattering angle of 90°. The zeta potential was measured in 10^{-3} M KCl at 20 °C. The amount of positive charges on the particle surface was determined by titration against the opposite charged polyelectrolyte sodium polyethylene sulfonate (PES-Na). For the measurement, 10 mL of the latex sample with a solid content of $1 \, g \cdot l^{-1}$ were used. The amounts of groups were calculated from the amount of consumed polyelectrolyte [100].

The polymer molecular weight and the amount of the surfactant Lutensol AT50 presented on the particle's surface was measured using gel permeation chromatography (GPC) with a SDV (PSS) column in THF at a flow rate of $1 \, ml \, \cdot min^{-1}$. The amount of Lutensol AT50 was determined

using the calibration curve, which was obtained by mixing different Lutensol AT50 amounts with polystyrene (M_w = 14,300 g · mol^{-1}) dissolved in THF.

The amount of incorporated fluorescent dye was determined by dissolving of 7.8 mg dried latex particles in 2.5 ml THF and measuring the absorbance of the solution at the peak maxima (568 nm for Lumogen F Red) using UV/Vis spectrometry. A calibration curve was used to determine the amount of dye per 1 g polymer.

The particle morphology was studied with scanning electron microscopy (SEM) and transmission electron microscopy (TEM). For SEM images, 1 µl of the diluted particle dispersion was dried on a silicon wafer. For TEM images, 3 µl of the diluted dispersion was dried on a carbon covered cupper grid.

The difference in fluorescence intensity between the particles was determined by fluorescence spectroscopy. The measurements were performed with particle dispersions (solid content 20 wt%) diluted with water at different ratios, i.e. to an estimated solid content of 0.5, 0.25 and 0.05%. The fluorescence intensity was read out at an excitation wavelength of λ_{ex} = 500 nm and an emission wavelength of λ_{em} = 600 nm. The slope of the line that was obtained by plotting the fluorescence intensity values against the solid content was used as a correction factor for flow cytometry experiments.

The critical micelle concentration of Lutensol AT50 and AT80 is determined by measuring the surface tension of Lutensol solutions in water using the DuNuoy ring method.

The stability of the particles in different media was determined by incubating NPs in demin. water, different buffers and cell media at a concentration of 75 mg · ml^{-1} on hydrophobic Ibidi 8well slides. Transmission and fluorescence images are taken after 1 and 24 h using a non-confocal fluorescence microscope and a 63x oil objective.

5.4.5 Grafting of SNARF-4F onto amino functionalized nanoparticles

The pH-sensitive dye SNARF-4F was grafted onto amino functionalized nanoparticles by a non-spacer EDC-coupling reaction that results in the amide formation between the carboxylic group of the dye and the amino group on the surface of the nanoparticle.

The reaction was performed at the conditions similar to those described in [127]. 0.15 mg of SNARF-4F (Invitrogen, Karlsruhe, Germany) dissolved in 300 µl DMSO (c = 0.5 g · l^{-1}) is added under stirring on ice to a solution of 0.32 mg HOBt and 200 µl H_2O. After addition of 425 µl EDC, the pH is adjusted to 5.0 with 2.5 ml 1 M HCl. The reaction is stirred at 4 °C for 30 min. After addition of 6 mg amino or non-functionalized nanoparticles in 120 µl H_2O, which leads to a 100x excess of SNARF-4F to the amount of surface amino groups, the pH is adjusted to 8.6 with 0.6 – 1.3 ml 0.1 M NaOH. The total volume of all samples is kept constant. The coupling reaction is performed at 4 °C under stirring for 42 h.

After the coupling reaction, prior any characterization all latexes were purified with PBS buffer (pH 7.2) via repetitive centrifugation/redispersion at 20,800 x g for 25 min until no fluorescence signal can be detected in the supernatant.

Fluorescence intensity is measured after 1:10 dilution of samples with phosphate buffer at different pH values to avoid self-quenching effects using a platereader. For fluorescence intensities at two distinct emission wavelengths, the following settings were used: λ_{Exc} = 542 nm, Δ_{Exc} = 5 nm and λ_{Em} = 575 nm (protonated form) alternatively 675 nm (deprotonated form), Δ_{Em} = 20 nm, where λ represents the wavelength and Δ represents the gap width of the monochromator. The gain is fixed to 100 a.u. For 2D and 3D fluorescence spectra, Δ_{Em} = 10 nm with a fixed gain of 150 a.u. and a step width of 5 nm is used. Measurements are performed in a black clear-bottom polystyrene 96-well plate. The plate is shaken for 5 s before measurements and data are obtained as mean values of 9 spots within one sample.

To determine the amount of physically adsorbed dye in comparison to covalently bonded dye, a pellet of 1 mg SNARF-4F-NPs is flocculated in 1 ml methanol, stirred at RT for 15 h and sonicated for 10 min in a sonication bath. After centrifugation, the methanol-containing supernatant is

freeze-dried and resuspended in buffer. The fluorescence intensity of the redispersed solution is measured and compared between approaches with amino and non-functionalized particles.

5.4.6 General cell culture

HeLa cells [128] were incubated in DMEM with 10% fetal calf serum, 100 units $\cdot$ ml^{-1} penicillin and 100 µg $\cdot$ ml^{-1} streptomycin in a humidified incubator at 37 °C and 5% CO_2. Cells were harvested after washing with 7 ml 0.5% trypsin/PBS for 7 min at 37 °C and ingested in 10 ml DMEM before counting. Thawed cells were kept in culture for max. 3 months due to the high mutation rate particular for HeLa cells.

5.4.7 Flow cytometry analysis

For flow cytometry analysis, cells were seeded at a density of 0.02 $\cdot 10^6$ cells per cm^2 in cell medium and 6well plates on day 1, incubated with polymer solution for different times on day 2 and, after a defined incubation time (typical 1 – 24 h) washed once with PBS and harvested with 0.5 ml 0.5% trypsin solution after an incubation time of 7 min at 37 °C. Trypsin reactivity is stopped by adding 0.5 ml of DMEM and washed 2 times with PBS. For antibody labeling with CD55/FITC, cells are redispersed after centrifugation with 20 µl of the 1:50 diluted antibody and incubated on ice for 45 min in darkness. The cells were washed again with PBS and filtered before measurement.

Flow cytometer data is obtained as a single intensity diagram (histogram) or as logarithmical two-dimensional dot plot. To gate the cells according to their size and internal complexity (granularity), a forward and sideward scatter (FSC/SSC) dot plot is generated. For CD55/FITC-labeling, cells are gated via a FCS/Fl1 plot. Fl1 specifications are λ_{Exc} = 488 nm, λ_{Em} = 527/30 nm. Nanoparticle fluorescence intensities are obtained by applying the cell gate to the fluorescence channel histogram (Fl5, λ_{Exc} = 561 nm, λ_{Em} = 610/30 nm). Data is taken as the median intensity of the selected events. Threefold determination is performed. Fluorescence intensities are normalized for comparison reasons with the amount of fluorescent dye of the particles as measured by fluorescence spectroscopy.

5.4.8 Cell toxicity

Cell toxicity is determined by staining apoptotic and necrotic cells with the fluorescent dye 7-AAD in flow cytometry or by measuring cell vitality as the conversion rate of a triphenyl tetrazolium chloride to a red triphenylformazan dye by metabolic active cells.

7-AAD is a fluorescent dye that labels the cytoplasm in apoptotic and, in addition, the nucleus in necrotic cells. Hence, three cell populations can be distinguished and quantified in flow cytometry. For 7-AAD labeling, cells are incubated after harvesting according to the flow cytometry standard procedure and incubated with 20 µl 7-AAD solution ($c = 0.2$ g $\cdot$ l^{-1} in PBS$^+$) for 15 min on ice. If antibody staining is performed, both 7-AAD and the antibody are coincubated.

3-(4,5-dimethylthiazol-2-yl)-5-(3-carboxymethoxyphenyl)-2-(4-sulfophenyl)-2H-tetrazolium (MTS) is a white compound that is enzymatically reduced to red formazan dye by the activity of various dehydrogenases. Reduction does not occur in necrotic cells due to degradation or denaturation of enzymes. For the MTS test, cells are grown and stimulated with the NPs in 96well plates. The cell medium is replaced by MTS-containing medium (dilution 1:10) and incubated for 60 min. The absorbance of the supernatant is measured at 492 nm in a black 96well plate with a platereader. Vitality is given in percentage of untreated cells.

5.4.9 Cryo-substitution preparation for TEM imaging

Cryo-subsitution experiments were performed by Dr. Martin Dass. HeLa cells were cultivated on carbon coated sapphire discs for 24 h at 37 °C, 5% CO$_2$ and 96% humidity, treated with polymer suspension during 24 h and fixed with a high pressure freezer. The concentration in the medium was 300 µg $\cdot$ ml^{-1} for each particle suspension. Afterwards, all samples were cryo-substituted in a substitution medium of acetone, 0.2% osmium tetroxide, 0.1% uranylacetate and 5% of water for 18 h [129]. During this process the temperature was increased from -90 °C to 0 °C. The staining effect of osmiumtetroxide was increased when the substituted samples were left in the substitution medium for 30 min to 1 h at room temperature. The samples were embedded in EPON and ultrathin sectioned with a microtome.

5.4.10 Blocking of endocytotic mechanisms with specific inhibitors

To determine the uptake pathway of nanoparticles, endocytotic processes are blocked by specific inhibitors. HeLa cells are pre-incubated with different concentrations of various inhibitors (chlorpromazine, cytochalasin D, dynasore and EIPA) in 1 ml PBS$^+$ for 30 min at 37 °C and 5% CO_2. Particles are added at a concentration of 150 µg · ml^{-1} and incubated for 60 min in the presence of the drugs. Cells are harvested for flow cytometry as described above. To distinguish between the particle and cell signal in the flow cytometer, cells are stained with an antiCD55/FITC antibody. The toxicity of the inhibitors is determined by staining cells with 7-AAD. For analysis, the values with the highest concentration of inhibitor with no effect to cell toxicity are used. This is in good agreement with previous studies [130].

5.4.11 Immunocytological staining

To study the uptake mechanism of nanoparticles, the participation of proteins involved in endocytotic processes can be determined by a colocalisation with nanoparticles. The proteins are labeled with their primary antibodies, which are stained with a fluorescent secondary antibody.

HeLa cells grown on Labtek chamber slides are incubation with nanoparticles at a concentration of 75 µg · ml^{-1} for different times. Cells are fixed with 300 µl of 3.7% PFA/CS-buffer for 20 min at RT and washed 3x. CS buffer chemicals from Table 6 are solved in 2 l demin. H_2O. After pH adjustment to 7.2 with 0.1 M NaOH (approx. 8 g), buffers are sterile filtered and stored at – 20 °C.

Table 6: CS buffer for fixation of cells with PFA (specifications for 2 l demin. H_2O).

Chemical	Concentration	Amount, g
Pipes	0.1 M	60,6
EGTA	0.001 M	0.76
PEG 8000	4 wt%	80

Permeabilisation is performed using 0.2% Triton X100/PBS buffer for 20 min at RT and washed 3x 200 μl of primary antibodies diluted in 1% BSA/PBS buffer are incubated with the cells for 1 h at RT in darkness and washed 3x. For antibody dilutions, see Table 7. 250 μl of diluted 2AK in 1% BSA/PBS buffer is incubated with the cells for 1 h at RT in darkness and washed 3x. Cell nucleus stain is performed with 250 μl of 1:1000 dilution of DraQ5/PBS buffer for 10 min at RT in darkness and washed 3x. The chamber slide is replaced by a cover slip and cells are covered with mounting medium Fluoromount G. To ensure long time stability, the cover slip edges are sealed with nail polish.

Table 7: Antibody dilutions.

Antibody	Dilution
EEA1 mouse	1:250
Lamp1 mouse	1:100
M6P mouse	1:100
Cav-1 rabbit	1:300
Cathepsin D mouse	1:100
Clathrin heavy chain mouse	1:100
Dynamin mouse	1:100
Anti-mouse/Alexa488 goat	1:1000
Anti-rabbit/Alexa488 donkey	1:1000

LSM images are obtained using a 100x oil objective. Excitation wavelengths were used as follows: λ_{Exc} = 476 nm for 2AK, λ_{Exc} = 594 nm for NPs and λ_{Exc} = 633 nm for cell core staining. To gain the ICQ values and PDM plots of the obtained samples, the ImageJ (http://rsbweb.nih.gov/ij/index.html) plugin *Jacop* [122] and *Intensity Correlation Analysis* (http://www.uhnresearch.ca/facilities/wcif/software/

Plugins/Intensity_Correlation_Analysis.java) are applied to a 100x100 pixel ROI of a sample stack.

5.4.12 Live cell labeling

Live cell labeling experiments have been performed by Dr. Sandra Ritz.HeLa cells are transfected with GFP constructs of endocytotic proteins, a gift from Gilles Spoden, Uniklinik Mainz. A list of the constructs is given in Table 8.

Table 8: Constructs for live cell labeling of endocytosis proteins [131].

Construct	Concentration, $g \cdot l^{-1}$	Application
Cav1-EGFP (CE)	1	Caveolin mediated endocytosis
EGFP-cav1 (EC)	1	Negative mutant for caveolin mediated endocytosis

1 µg of DNA is mixed with 100 µl serum-free DMEM and 3 µl Fugene HD and incubation for approx. 30 min. The DNA/lipid mixture is applied to HeLa cells in Ibidi-treat 8well plates and 200 µl DMEM. After 24 h incubation, cells are stimulated with NPs at different times or with AlexaFluor 594-labeled cholera toxin B (c = 5 µg $\cdot$ µl^{-1}) for 1 h and imaged by cLSM.

5.4.13 Intracellular calibration of pH-sensitive SNARF-4F for cLSM and fluorescence spectroscopy

For quantitative evaluation of the environmental pH of SNARF-4F-NPs an intracellular calibration using SNARF-4F AM ester (and at representative pH values SNARF-4F-NPs) is performed by equilibration the extracellular and intracellular pH with ionophores.

For loading of HeLa cells with SNARF-4F AM ester, cells are washed with HEPES buffer. 0.5 µg SNARF-4F AM ester in 10 µl DMSO is incubated with 10 µl of FCS for 5 min to improve water solubility and loading efficiency [125] and then added to the cells with 500 µl buffer. The loading procedure is performed during 15 min at RT. After the loading procedure, the cleavage of the dye is performed in a humidified incubator for 15 min at 37 °C and 5% CO_2. Alternatively for calibration measurements with dye-nanoparticle constructs, cells are loaded with 0.15 g $\cdot$ l^{-1} of

SNARF-4F-NPs for 24 h, washed and measured in 500 µl buffer. The ionophores nigericin (5 µg) and valinomycin (2.5 µg) are solved in 15 µl DMSO and added to cells immediately before measurements to minimize toxic effects to the cells.

All buffers used are potassium rich and carbonate-free to ensure good pH equilibration by K^+ ionophores and a long time pH stability in the presence of air, respectively. Table 9 shows the buffers used for intracellular calibration. Buffer chemicals are solved in 500 ml demin. H_2O. After pH adjustment with 0.1 M HCl or NaOH, buffers are sterile filtered and stored at 4 °C.

Table 9: Buffers used for intracellular calibration (specifications for 500 ml demin. H_2O).

pH	4.6	5.0	5.5	5.75	6.0	6.4	6.6	6.8	7.2	8.0
KCl, g	4.8	4.8	4.8	4.8	4.8	4.8	4.8	4.8	4.8	4.8
FCS[1], g	5.0	5.0	5.0	5.0	5.0	5.0	5.0	5.0	5.0	5.0
$MgCl_2 \cdot 6\ H_2O$, g			0.2	0.2	0.2	0.2	0.2	0.2	0.2	0.2
HEPES[2], g									3.6	
MES[3], g			3.0	3.0	3.0	3.0	3.0	3.0		
Bicine, g										2.4
Citric acid $\cdot$ 1 H_2O, g	5.6	5,1								
$Na_2HPO_4 \cdot 2\ H_2O$, g	8.2	9.1								

[1] *Fetal calf serum (FCS),* [2] *4-(2-hydroxyethyl)-1-piperazineethanesulfonic acid (HEPES),* [3] *2-(N-morpholino)ethanesulfonic acid (MES).*

For platereader measurements, λ_{Exc} = 514 nm, Δ_{Exc} = 5 nm and λ_{Em} = 575 nm (protonated form) alternatively 675 nm (deprotonated form), Δ_{Em} = 20 nm. The plate is shaken for 5 sec before measurements and data is obtained as a mean value of 9 spots within one sample. CLSM measurements are performed using a 100x oil objective and a tunable Argon laser with λ_{Exc} = 514 nm and 20% power. λ_{Em} = 550 - 610 nm, gain 761.4 a.u. and offset -0.3 a.u.(protonated form) alternatively 640 - 750, gain 813.9 a.u. and offset -0.3 a.u. nm (deprotonated form). Confocal setup is kept constant throughout the experiments.

For platereader measurements, the obtained intensities at the two emission wavelengths were used as processed. For cLSM images, the mean value of 50 quantified regions of interest per sample is used. To generate a calibration fit, the ratios of protonated and deprotonated fluorescence intensities are displayed in dependence to the associated pH value and fitted binomially. The thus obtained fit can be applied as calibration formula for platereader measurements and cLSM image processing.

5.4.14 cLSM image batch processing

For image batch processing, a self-written batch program executes an ImageJ (http://rsbweb.nih.gov/ij/index.html) macro created with ImageJ macro recorder for all cLSM files within a specific folder.

To obtain an image, z-stack or movie that directly displays the pH values of the nanoparticles in a LUT table, the following steps are performed: multiply ratio image (Channel1 / Channel2) with a mask image to reduce background noise, perform mathematic operation according to binomial fit function as obtained by calibration and set LUT.

3D images of pH pseudocolored z-stacks were obtained using the ImageJ plugin Volume Viewer from K. Barthel, Berlin, Germany.

For quantification, a histogram displaying the distribution of pH values per image can be exported from ImageJ.

6 *Results and Discussion*

The potential of nanoparticles as novel drug delivery systems is still a very active area of research. To design nanoparticles in a way, that they will specifically target incorporated active ingredients is still a big challenge. One main factor that may influence the uptake kinetic and route is thought to be the NP size. To define the size dependent uptake kinetic and the endocytotic pathway of NPs, two sets of polystyrene NPs with different sizes, stabilized either with non-ionic or with cationic surfactant have been synthesized with different polymerization techniques: miniemulsion, dispersion and seed polymerization. Non-ionic NPs with different sizes were synthesized with dispersion polymerization. Seed particles for seeding polymerization that incorporated a high amount of fluorescent dye were synthesized with miniemulsion polymerization and cationic NPs of bigger size (> 120 nm) were synthesized with seeding polymerization.

The uptake kinetics of these particles was determined with regards to their number, solid content and the total surface area. The uptake mechanism of cationic NPs with different sizes was investigated using three different techniques: blocking of uptake processes with pharmacological inhibitors, immunocytological staining, and immunofluorescence. The obtained results were compared, where possible.

Incorporated nutrients or proteins that need to be down-regulated are enwrapped in vesicles which are acidified during their maturation process and subsequently digested. Upon endocytosis, NPs end up in the same endo-lysosomal compartments. To probe the environmental pH of NPs within these vesicles over time, the pH-sensitive dye SNARF-4F was grafted onto amino-functionalized NPs through EDC-coupling reaction. The amino functionalized polystyrene NPs were synthesized by miniemulsion polymerization. In the intracellular calibration a cell-penetrable SNARF-4F AM ester is used to define accurate pH values of the NP environment. The acidification process of NPs is quantified over time.

6.1 Formation and cell interaction of cationic and non-ionic particles with different sizes

Two sets of non-ionic and cationic NPs were synthesized with miniemulsion, dispersion and seed polymerization. The colloidal characterization of the NPs after purification includes their size, morphology, zeta potential, fluorescent intensities, amount of non-ionic surfactant Lutensol AT50 as well as amount of positive surface charges.

The endocytotic process is defined for cationic NPs with different sizes by blocking of specific mechanisms with pharmacological inhibitors, staining of endocytotic proteins with antibodies as well as expressing two fluorescent variants of caveolin.

6.1.1 Routes of synthesis

For the preparation of non-ionic and ionic polystyrene particles with different sizes and well-defined properties such as a total net charge and surface chemistry, three different approaches were applied: dispersion polymerization, miniemulsion polymerization, and seed dispersion polymerization. Dispersion polymerization was used to synthesize the particles stabilized with the non-ionic surfactant Lutensol AT50. This method allows production of large and small size particles as a function of the surfactant amount. The miniemulsion polymerization was applied to obtain positively and negatively charged particles of 120 nm. Polystyrene particles synthesized by miniemulsion were further used in free radical polymerization of styrene as seed particles. The addition of styrene to the aqueous dispersion of polystyrene seed particles leads to the swelling of seeds and in the presence of initiator to their growth in size upon polymerization. Thus, monodisperse, positively and negatively charged particles of bigger size could be produced.

The amount of surfactant used in miniemulsion is typically below the critical micelle concentration (CMC) when the surface of the droplets is taking into account, so that secondary nucleation is eliminated. The CMC of the cationic surfactant CTMA-Cl is $1.25 \cdot 10^{-5}$ mol $\cdot$ l^{-1} [132]. The CMC of Lutensol AT50 and AT80 was determined as $1.7 \cdot 10^{-6}$ mol$\cdot$l^{-1} and $1.1 \cdot 10^{-6}$ mol$\cdot$l^{-1}, respectively by measuring the surface tension of Lutensol AT50 and AT80 solutions using the

DuNuoy ring method (see Figure 6). The CMC of both Lutensol types is in the same concentration range and lower than the CMC of CTMA-Cl, which is due to the lower solubility of the nonionic surfactant in water.
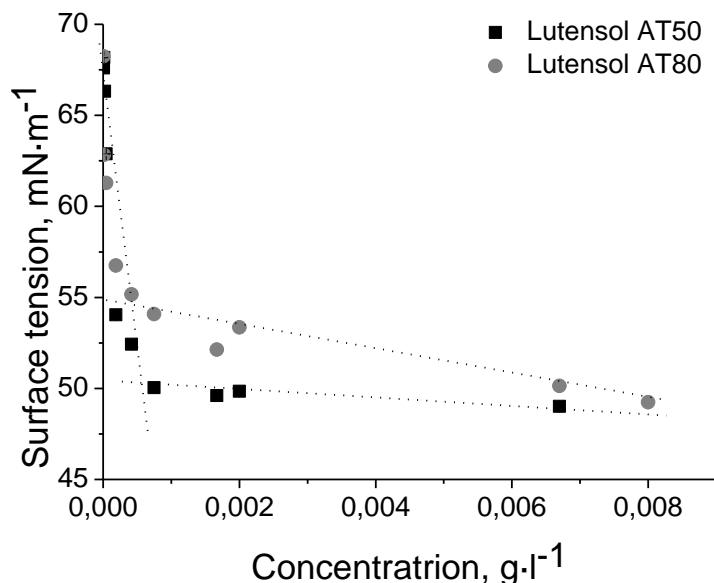

Figure 6: Surface tension of Lutensol AT50 and Lutensol AT80 aqueous solutions as measured using the DuNuoy ring method to determine the CMC; $CMC_{Lutensol\ AT\ 50} = 1.7 \cdot 10^{-6}\ mol \cdot l^{-1}$ and $CMC_{Lutensol\ AT\ 80} = 1.1 \cdot 10^{-6}\ mol \cdot l^{-1}$.

For the detection in cells by cLSM and flow cytometry, particles are labeled with the fluorescent perlyene dye Lumogen F Red. Absorption and fluorescence spectra of Lumogen F Red are given in Figure 7. The absorption spectrum is very broad with a maximum at 568 nm. The fluorescence maximum with λ_{Exc} = 561 nm is located at 601 nm. Ergo Lumogen F Red possesses a Stoke's shift of approx. 40 nm. Absorption at 488 nm, which is a typical excitation for an Argon laser and is used for many biomolecule labels, e.g. with the dye Alexa488, is rather low. The co-excitation of e.g. Alexa488-labeled molecules and Lumogen F Red incorporating NPs is possible if a fluorescence setup is used that eliminates bleed-through between the two channels, as it was done here by using two different excitation wavelengths.
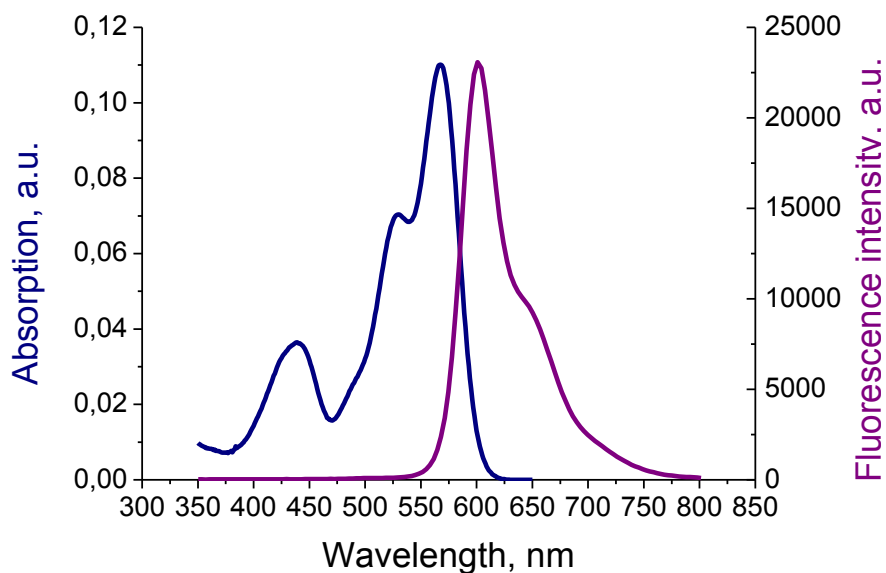
Figure 7: Absorption and fluorescence spectrum (λ_{Exc} = 561 nm) of Lumogen F Red in THF.

Polystyrene particles with different sizes and non-ionic surfactant

The synthesis of non-ionic polystyrene particles was performed via the dispersion polymerization in water/ethanol medium. Dispersion polymerization in ethanol is an effective approach to obtain monodisperse polystyrene particles using a non-ionic surfactant in a broad size range [13, 14]. Using different amounts of the non-ionic surfactant Lutensol AT50, polymeric particles with an average size between 132 and 846 nm were obtained. For the cell uptake experiments it is very important that the studied particles differ only in their sizes, whereby holding other parameters, such as the total net charge and surface chemistry identical. Therefore, all samples were purified under the same conditions and afterwards the amount of Lutensol AT50 in the particle dispersion was determined by GPC. The results reveal that all particle samples contain approximately the same amount of Lutensol molecules per nm^2. The values of zeta potential for non-ionic particles were between -1 and - 3 mV. The characteristics of the particles are summarized in Table 10 and SEM images are presented in Figure 10.

Table 10: Characteristics of fluorescence polystyrene particles obtained with non-ionic surfactant Lutensol AT50 by dispersion polymerization.

Sample	Luten-sol AT50, mg	D_i, nm	Lutensol AT50 molecules per nm$^{2a)}$	Lumogen F Red [d]		Fluorescence normalization [e]	
				mg per $g_{Polymer}$	Factor	a.u.[f]	Factor[g]
SL-DP5	1,000	132 ± 19	0.12	0.66	1.00	564.2	2.76
SL-DP6	500	180 ± 10	0.08	0.71	1.07	230.0	6.76
SL-DP7	200	242 ±27	0.05	0.49	0.74	495.6	3.14
SL-DP8	100	635±70	_ [b]	_ [b]	_ [b]	_ [b]	
SL-DP8-420[c]		816 ± 44	0.05	0.95	1.44	379.5	4.10
SL-DP8-110[c]		846 ±51	0.06	0.80	1.21	1237.5	1.26

a) Determined from the GPC measurements after dialysis; b) The measurements were not performed as these particles were used for further processing; c) Particles obtained after separation through centrifugation of sample SL-DP8; d) Calculated from the UV/Vis spectroscopy data, e) Measured by fluorescence spectroscopy at three different particle concentrations: f) The three fluorescence intensities obtanied from different particle concentrations are linearised and the slope is given as a mean to normalize the differences in fluorescence between the particles; g) Fluorescence intensity slope from particle SL-V502 is set to 1 (see Table 11) and all other values are adjusted accordingly.

In general, with 200 mg (3.3% with respect to styrene) and above of Lutensol AT50, small and monodisperse particles were produced. With 100 mg (1.7% with respect to styrene) of surfactant, the obtained particles were big in size and have polymodal size distribution (±70 nm). Different modes were separated by centrifugation the sample at 110 x g and 420 x g. After each centrifugation step, the obtained pellet was redispersed in water and characterized. The DLS and SEM data reveal the narrow size distribution of particles (Table 10, Figure 10, samples SL-DP8-420 and SL-DP8-110). The incorporation yield of fluorescent dye, which was calculated from particles dissolved in THF and measured by UV/Vis, is high enough (0.5 - 1 mg · $g_{Polymer}^{-1}$) to provide a detectable signal in the flow cytometry analysis.

As UV/Vis measurements reveal the exact amount of fluorescent dye per $g_{Polymer}$, but ignore interactions within the polymer, the fluorescence of particle dispersion was measured directly

at three different dilutions (estimated solid content of 0.5, 0.25 and 0.05%). Measuring dispersion in fluorescence spectroscopy induces a broadening of the excitation peak as the NPs scatter the incoming light. The fluorescence spectra in Figure 8A are measured at λ_{Exc} = 500 nm for the exemplary sample SL-DP6. It can clearly be seen that the excitation peak spreads almost from 450 – 550 nm and intrudes on the fluorescence signal of the dye as can be seen in Figure 8B. In addition, the spectra exhibit a larger noise. The slopes obtained by linear fitting of fluorescence peak maxima over the solid content are used as normalization factors (see Table 10). A typical fit is displayed in Figure 8C from the sample SL-V502.
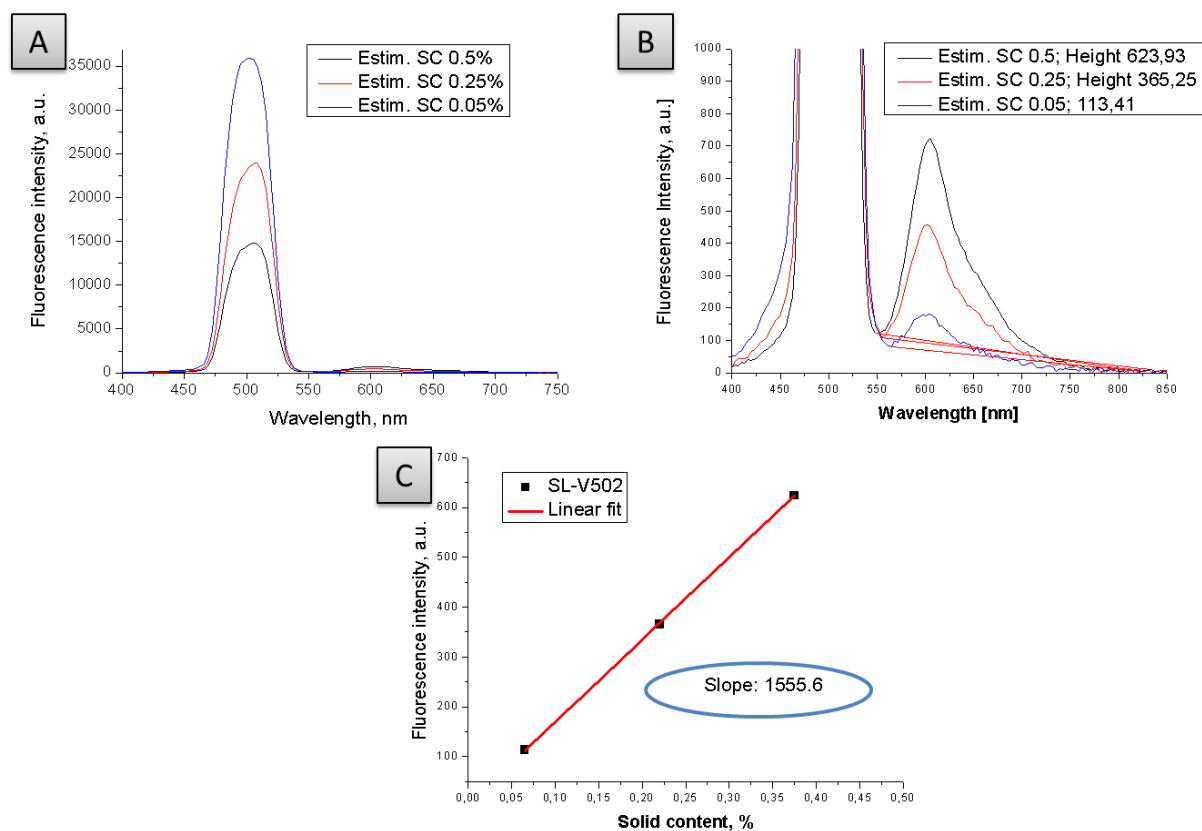

Figure 8: Fluorescence spectroscopy of NP dispersions at three different dilutions is used to normalize the fluorescence intensities between the NPs. A: Fluorescence spectra exhibit a broad excitation peak, B: Fluorescence signals from Lumogen F Red, C: Linear fit of the peak maxima in correlation to the sample's solid content.

The particle size in dispersion polymerization could be adjusted to the amount of surfactant used. Figure 9 shows that this dependency is not linear and that the standard deviation increases with a decrease of surfactant.
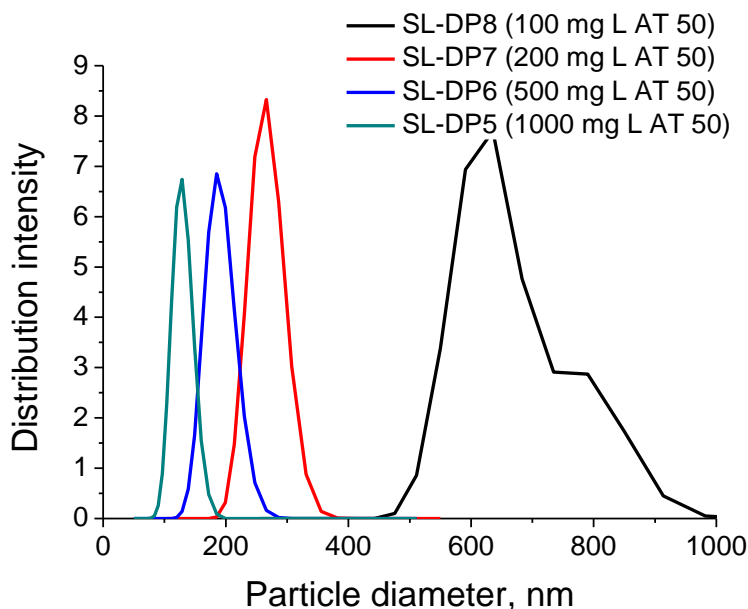

Figure 9: Size distribution histograms for NPs obtained with different amounts of non-ionic (L AT 50 = Lutensol AT 50; sample SL-DP8 before separation).

Figure 10 represents SEM images of the polystyrene particles formed with different amounts of Lutensol AT50. It is clearly seen that the particles are spherical in shape, monomodal in the size, and the mean size of the particles decreases with higher concentrations of surfactant.

The amount of Lutensol AT50 that is present in the dispersion of particles synthesized with non-ionic surfactant is obtained by quantitative GPC. The elution diagram is displayed in Figure 11A. The percentage of Lutensol AT 50 with respect to polystyrene as obtained by integrating the elution peaks was compared and fitted with a Boltzmann fit with the weighted percentage of Lutensol AT50 (Figure 11B). Using this calibration, the percentage of Lutensol AT50 in a NP sample is determined. Figure 11C shows an elution diagram of an exemplary NP sample in THF. The polystyrene from the NPs features a broader molecular distribution and the Lutensol AT50 peak possesses the same elution volume value. The non-linear sigmoidal course of the fit is due to the lower and upper detection limits of the GPC detector.

Recapitulatory, it was possible to synthesize non-ionic fluorescent polystyrene particles with different sizes that feature a monomodal size distribution and a comparable amount of surfactant per nm^2. The particles are characterized reasonably to draw conclusion from comparing the cellular uptake of these NP.
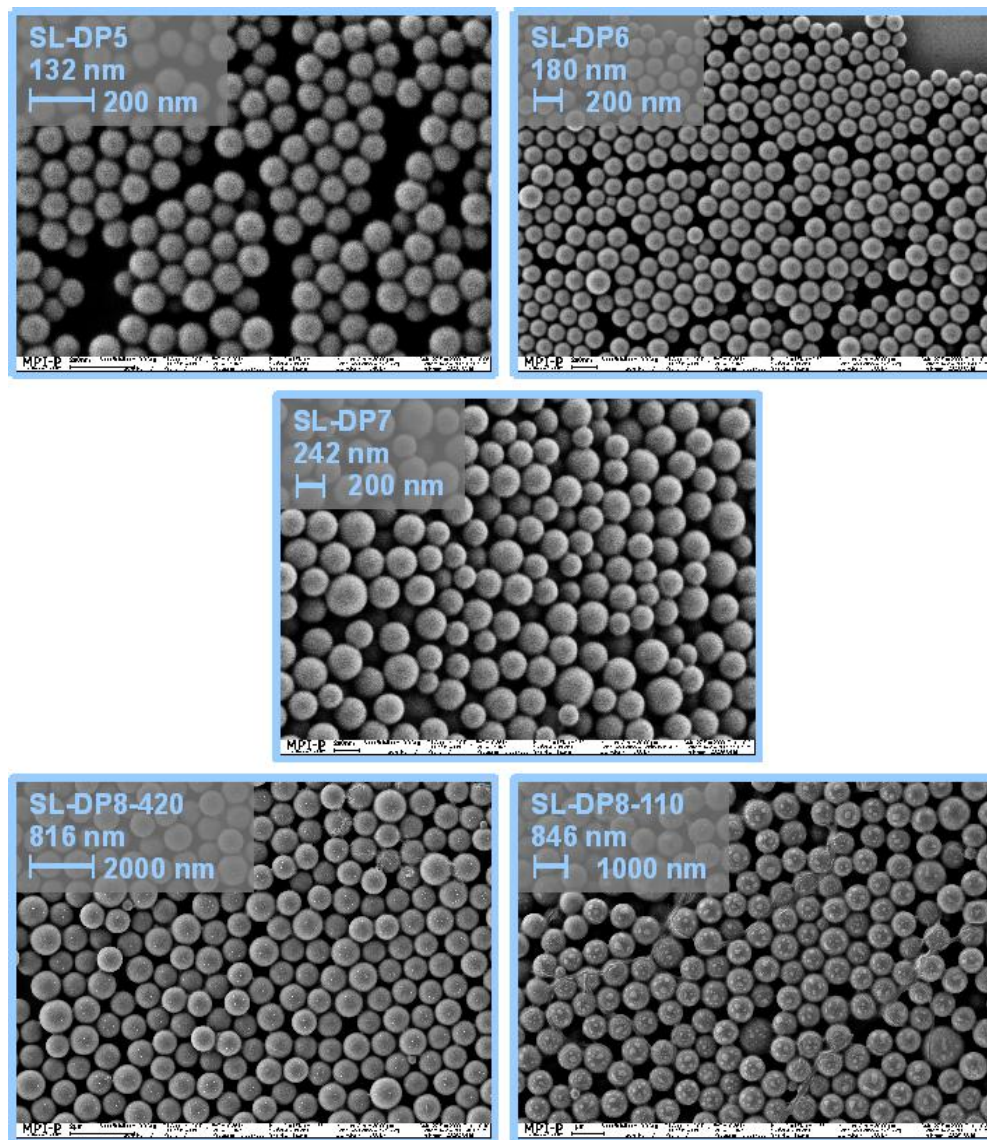

Figure 10: SEM images of polystyrene particles obtained via dispersion polymerization with different amounts of surfactant Lutensol AT50. SL-DP5: 1,000 mg Lutensol AT50, 132 nm; SL-DP6: 500 mg Lutensol AT50, 180 nm; SL-DP7: 200 mg Lutensol AT50, 242 nm; SL-DP8-420: 100 mg Lutensol AT50 and additional fractionation, 816 nm; SL-DP8-110: 100 mg Lutensol AT50 and additional fractionation, 846 nm.
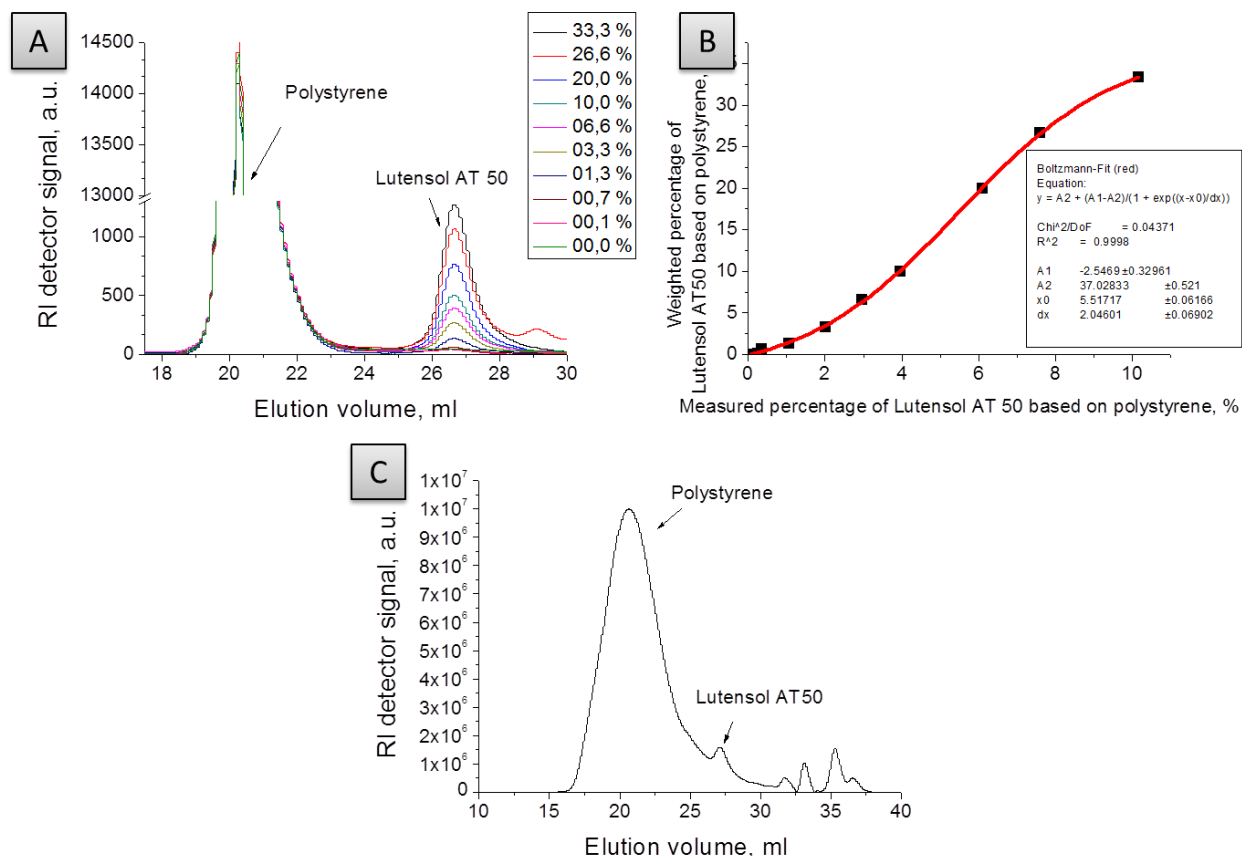
Figure 11: Determination of Lutensol AT50 amount per nm² using gel permeation chromatography. A: Elugram of polystyrene with different amounts of Lutensol AT50, B: Calibration fit, C: Elugram of an exemplary NP sample (SL-DP5).

Polystyrene particles with different sizes and cationic surfactant

Positively charged polystyrene particles with a diameter of 120 nm (sample SL-V502) were obtained by the miniemulsion polymerization using the cationic surfactant CTMA-Cl and the water-soluble cationic initiator V50. Seed dispersion polymerization was used to increase the particles size. The seed particles (120 nm, sample SL-SP) were obtained by miniemulsion polymerization. The difference between SL-V502 and SL-SP is the amount of used fluorescent dye Lumogen F Red: 4 mg in SL-V502 and 40 mg in SL-SP. The incorporation of a higher dye content in the seed particles was necessary to have enough fluorescence signal after particle "growth" via seed polymerization. Due to its pure diffusion in the water phase and absence of polymerizable moiety, the hydrophobic dye cannot be inserted in the "growing" polymeric layer upon seeding polymerization.

After polymerization, the particles were washed from the excess of surfactant and possible water-soluble oligomers and characterized by DLS, TEM, UV/Vis, fluorescence spectroscopy, PCD and zeta potential measurements. The obtained data are summarized in Table 11 and TEM images are given in Figure 12.

Table 11: Characteristics of fluorescent positively charged polystyrene particles obtained with cationic surfactant and water-soluble cationic initiator V50.

| Sample | CTMA-Cl, wt% | D_i, nm | Lumogen F Red[c] | | Fluorescence normalization [d] | | Amount of positive charges | | Zeta pot. [g], mV |
			mg per $g_{Polymer}$	Factor	a.u. [e]	Factor [f]	Per particle $\cdot 10^3$	Per nm^2	
SL-V502	1.7	120 ± 10	0.80	1.00	1555.6	1.00	32	0.71	+73
SL-SP	1.7	120 ± 12	_ [b]	_ [b]	_ [b]	_ [b]	_ [b]	_ [b]	+77
SL-S27[a]	0.7	208 ±29	2.16	0.37	3164.4	0.49	25	0.19	+56
SL-S30[a]	0.17	267±28	1.23	0.65	4077.2	0.38	76	0.34	+56
SL-S26[a]	0	603±15	0.28	2.85	1122.4	1.39	1,307	1.14	+60

a) Obtained by seed dispersion polymerization, using SL-SP as seed; b) The measurements were not performed, because these particles were used only as seed particles and not studied in the cell uptake experiments. c) Calculated from the UV/Vis spectroscopy data; d) Measured by fluorescence spectroscopy at three different particle concentrations: e) The three fluorescence intensities obtanied from different particle concentrations are linearised and the slope is given as a mean to normalize the differences in fluorescence between the particles; f) Fluorescence intensity slope from particle SL-V502 is set to 1 (see Table 11) and all other values are adjusted accordingly; g) Zeta potential.

From DLS and TEM studies it can be seen that particles possess a narrow size distribution. The PCD measurements reveal that with the increase in particle size, the density of positive charges increases. We did not expect to observe this effect, because to obtain bigger particles less

amount of surfactant was used (see Table 11). We hypothesize that the charges originated from the cationic initiator. After polymerization, the positively charged groups from the initiator are covalently bonded to the particle surface and their concentration does not change after dialysis of the particles, whereas surfactant molecules are partially washed out. All particles possess a positive zeta potential value around +60 mV $\pm$ 10 mV.

The particle fluorescence was directly obtained by measuring the fluorescence intensity of the diluted particle dispersions. As shown in Table 2, the correction factor between the amount of fluorescent dye (measured by UV/Vis spectroscopy) and the fluorescence intensity is not the same. This is probably due to interactions between the dye molecules themselves as well as between the dye molecules and the polymer that lead to a disturbance of the fluorescence intensity, e.g. by quenching. For the analysis of flow cytometry data, the correction factors obtained from fluorescence spectroscopy measurements were used.
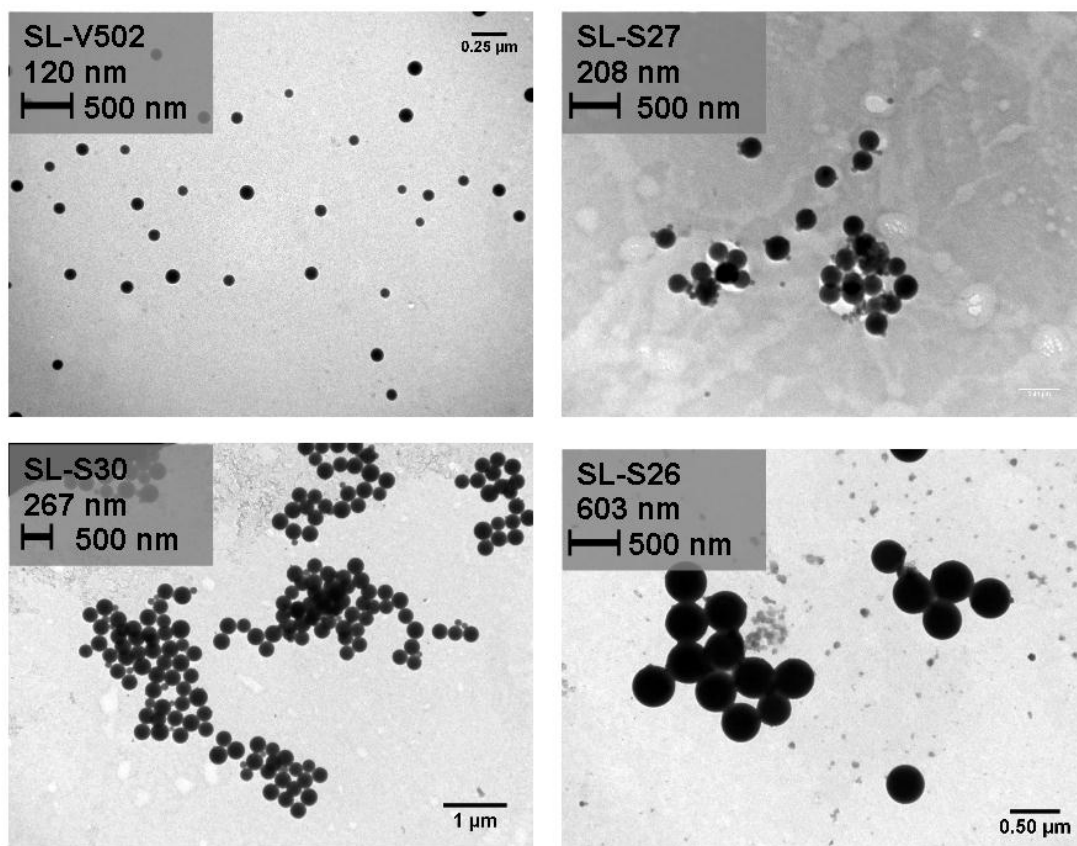

Figure 12: TEM images of positively charged polystyrene particles synthesized by miniemulsion (SL-V502) and seed (SL-S27, SL-S30 and SL-S26) polymerization.

The particle size is correlated to the amount of monomer added to the system. An excess of 30, 60 and 100 times the amount of styrene with respect to the solid content is used for SL-S27, SL-S30 and SL-S26, respectively.

The theoretical maximum size that is obtainable in seed polymerization can be calculated as follows:

$$d_{theor} = 2 \cdot ((\tfrac{1}{2}D_I)^3 \cdot X)^{1/3} \, , \qquad\qquad (13)$$

where D_I is the diameter of the seed particle and X the excess of styrene with respect to the amount of seed particle. As can be seen in Figure 13, the calculated size is not exactly the same as the obtained one. A smaller particle size as with SL-S27 and SL-S30 results from a loss of styrene due to the secondary nucleation and polymerization in the continuous phase rather than in the seed particles [19]. The thus formed oligomers and low-weight polymers are removed during the purification process. For SL-S26, the obtained value is slightly higher than the calculated size. The reason for this remains unclear.
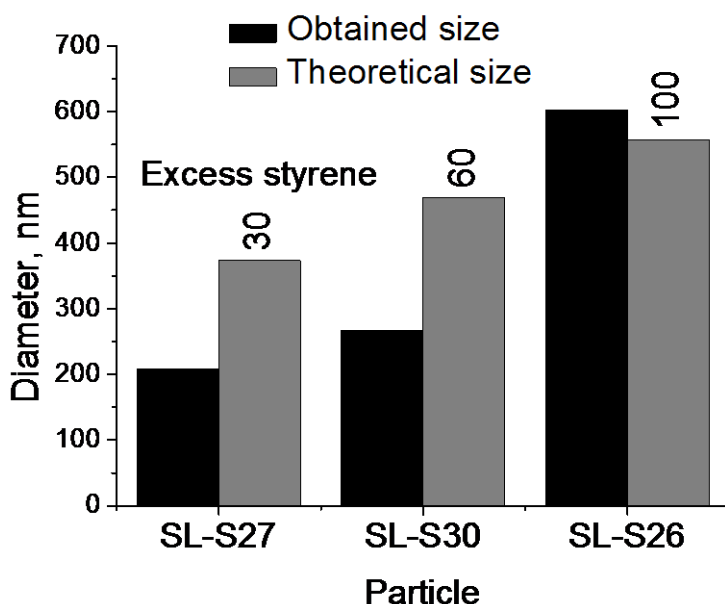

Figure 13: Comparison between theoretical and obtained diameters as measured by DLS in seed polymerization for a styrene excess of 30, 60 and 100 with respect to the amount of seed particle.

The chemical composition of the continuous phase plays an important role on the stability of NPs that are synthesized with ionic or non-ionic surfactant. The behavior of NPs in cellular medium influences the uptake to cells, as proteins form a layer around the particles. NPs were incubated in different media and observed with light and fluorescence microscopy to gain a semi-quantitative conclusion on the stability of NPs. Figure 14 shows fluorescence and transmission images of the sample SL-S26 in different media after 24 h incubation as an example to determine the behavior of the particles in different aqueous solutions. The different media influence the distribution and flocculation behavior of the NPs. In water and human serum (HS), particles are clearly separated from each other. In other types of media, esp. phosphate buffer with additional calcium and magnesia (PBS$^+$) and Dulbecco's modified eagle medium (DMEM) some flocculation is visible, but the majority of NPs appear single particles. However, particles can still be present in small aggregates. This cannot be distinguished from free NP due to the insufficient resolution of transmission and fluorescence microscopy.

An overview of the flocculation behavior of NPs is given in Table 12. Although all particles are stabilized with the cationic surfactant CTMA-Cl and bear same zeta potential, the flocculation behavior varies. The most sensitive are the smallest particles (sample SL-V502) in almost all tested media. Larger particles prove to be more stable suggesting that the stability may also depend on the particles' curvature or surface area. The higher the surface, the more "stabilizing" proteins can be attached to it. The medium that causes the lowest degree of flocculation is DMEM with 10% serum, and therefore it was used for the incubation of NPs with cells in the following experiments.

H₂O   PBS⁻   PBS⁺

DMEM   DMEM plus FCS   HS
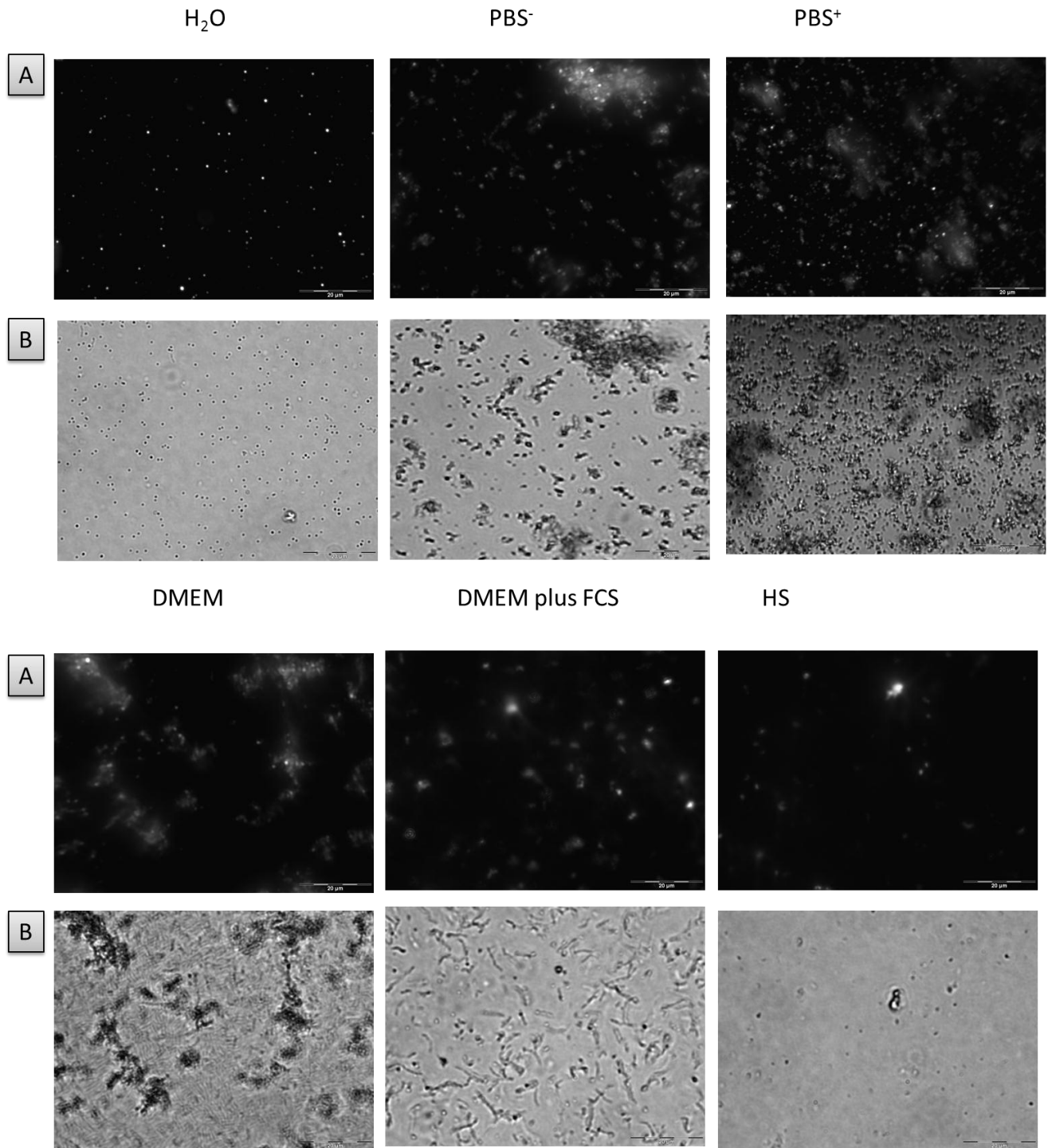
Figure 14: Wide field fluorescence (A) and transmission (B) images of sample SL-S26 in different media: H₂O, PBS buffer without (PBS⁻) and with (PBS⁺) magnesia and calcium, cell medium without (DMEM) and with (DMEM plus FCS) 10% serum and human serum (HS). Scale bar at 20 μm.

Table 12: Flocculation behavior of NPs in different media after 1 and 24 h incubation as determined by transmission and fluorescence microscopy.

	SL-V502		SL-S27		SL-S30		SL-S26	
	1 h	24 h	1 h	24 h	1 h	24 h	1 h	24 h
H$_2$O	+	0	-	+	-	-	-	-
PBS$^-$	+0	+	-	0	0+	0+	0	0
PBS$^+$	+0	+	0	-	0+	0+	0	0+
DMEM	+	+	0	0	+	0+	+	0+
D/F [a]	0-	+	-	+	-	-	0-	0
HS [b]	+	0	-	+	-	-	0-	0

a) DMEM with 10% FCS; b) human serum; +: majority of particles is flocculated; 0: some flocculation occurs, but most particles seem to be single; -: particles appear to be completely separated.

6.1.2 Size-dependent uptake kinetic of cationic and non-ionic particles to HeLa cells: Influence of particle concentration, number and total surface area

The cellular uptake of nanoparticles with different sizes and net surface charge was studied by confocal light scanning microscopy (cLSM) and flow cytometry. Detailed particles characteristics are given in Table 10 and Table 11. In the first set of studies, the weight of the nanoparticles added was kept constant at 75 µg · ml^{-1}.

Confocal laser scanning microscopy images of the particles endocytosed by HeLa cells are presented in Figure 15. In Figure 16, the quantitative uptake values as measured by flow cytometry are shown. The uptake of particles with non-ionic surfactant is low and the uptake (in wt%) of smaller size particles was consistently higher than that of large particles. In addition, particles with 816 nm and 846 nm in diameter tend to stick to the cell membrane and they are not endocytosed into the cell, as can be seen in Figure 15.
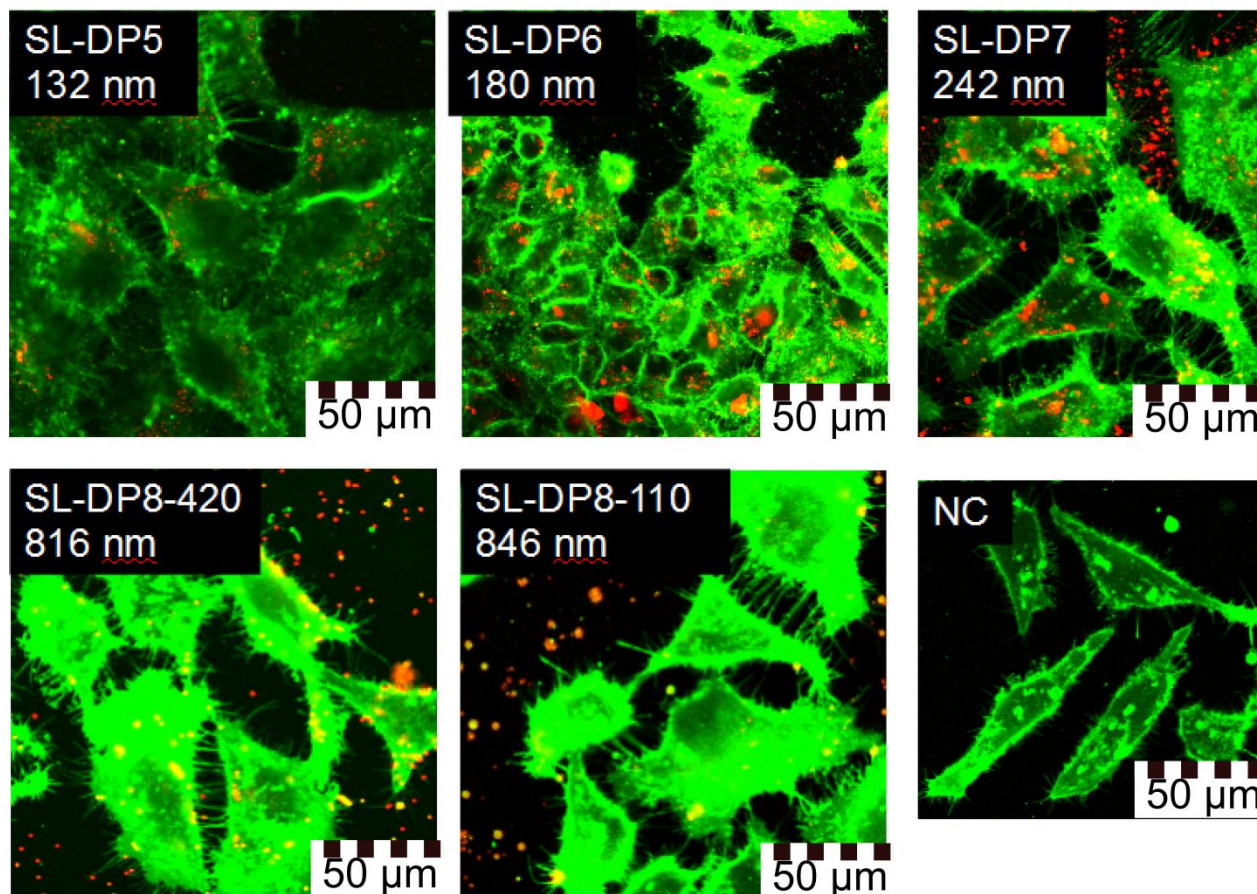
Figure 15: cLSM images of HeLa cells after incubation for 24 h with 75 µg·ml⁻¹ of polystyrene particles stabilized with non-ionic surfactant. The HeLa cells are stained with DiO (green) and particles are red in color. NC corresponds to the negative control. (HeLa cells after incubation for 24 h without addition of particles).

The toxicity of Lutensol AT50 stabilized particles is known to be very low [55]. In contrast, CTMA-Cl functionalized particles may be toxic due to the quarternary ammonium groups of the surfactant. The toxicity is mainly dependent on the amount of surfactant present in the particle dispersion. The cell vitality was measured by the metabolic rate of the enzymatic reduction of the formazan dye MTS. Figure 17 displays the cell vitality with respect to a positive control for the cationic NPs of different sizes after 1 and 24 h at different concentrations. All particles synthesized with seed polymerization (SL-S27, SL-S30 and SL-S26) are not toxic to HeLa cells in any of the tested concentrations. Only SL-V502 shows toxic effects after 24 h incubation and at higher concentrations. The concentration of 75 µg · ml⁻¹, which is the standard concentration for cellular uptake experiments, is not toxic to cells even after 24 h. The concentration of

150 µg· ml^{-1}, which is used for experiments with pharmacological inhibitors, is toxic, but only after 24 h. For the afore mentioned experiments, an incubation time of 1 h is used, so that no toxic effects are present. All particles show a comparable zeta potential including SL-V502. However, a larger amount of initiator and a lesser amount of CTMA-Cl is used for seed polymerization and particles are purified again after seeding. The difference in toxicity may refer to different surface groups of the particles: SL-V502 features more positively charged CTMA-Cl whereas seed particles feature more positively charged amidine groups that origin from the initiator and are known to be not toxic to cells [133]. For some particles, the vitality reaches significantly values higher than the control. It may be that in some cases the presence of particles gives rise to an increase of metabolic activity as cells are occupied taking up particles.
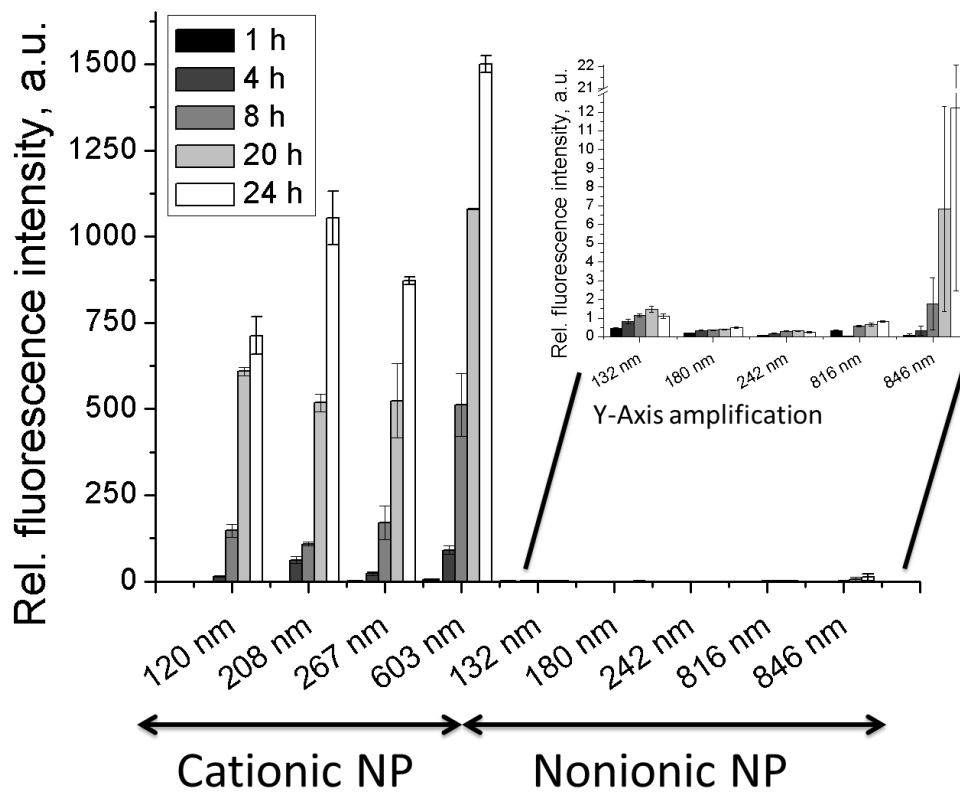
Figure 16: Time-dependent HeLa cells uptake of polystyrene particles (c = 75 µg · ml⁻¹) stabilized with cationic CTMA-Cl surfactant and non-ionic Lutensol AT50. Averages and standard deviation from triplicate measurements are given.
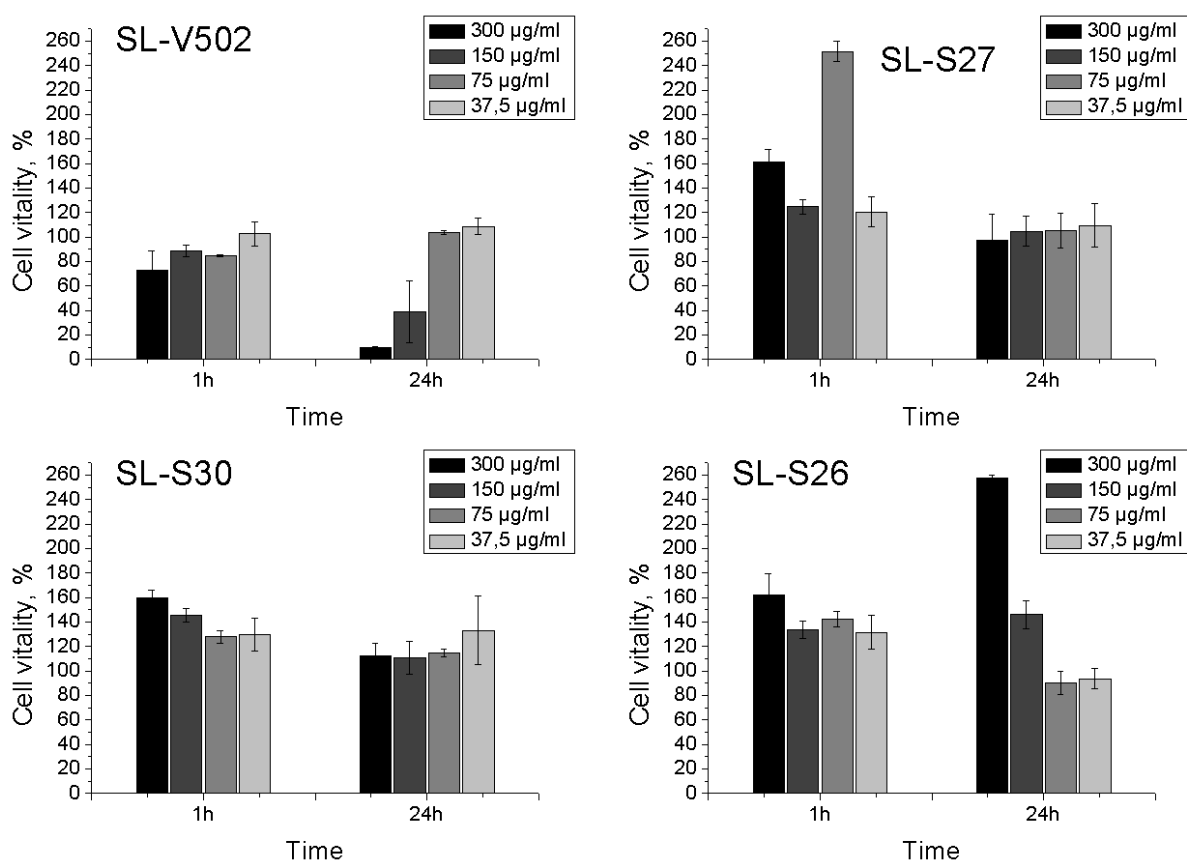
Figure 17: Vitality of the HeLa cells after incubation with cationic NPs at different concentrations. The vitality was determined by MTS test.

In contrast to the Lutensol AT50 stabilized particles, the uptake of positively charged particles is significantly higher up to a factor of 100, as can be seen from the cLSM images (Figure 19) and uptake kinetics results (Figure 16). It has been previously reported [55, 61, 134] that high rate and extent of positively charged particles uptake is mainly due to the strong attraction between the particles and a negatively charged outer cell membrane surface. This effect seems to be size independent because even particles large than 500 nm (sample SL-S26, 603 nm) are taken up by the cell, although HeLa cells are non-phagocytic. It is questionable if the whole particle or a section of the particle's surface is recognized by the cell. Thus, additional cell uptake experiments were performed with positively charged particles of different sizes, keeping either the number of particles or the total interaction surface area constant (before the weight or volume was kept constant). The number of particles and surface area were calculated from the

mean diameter values are given in Tables 1 and 2. The amount of internalized particles was measured by flow cytometry after 1 and 24 h incubation (Figure 18). For all samples, except SL-S26, the amount of particles was set to $7.9 \cdot 10^{16}$ particles per ml and the total interaction surface area at 2060 m^2 per ml. Both values correspond to the number of particles or total surface area, respectively, of 208 nm particles (sample SL-S27) with a solid content of 75 µg · ml$^-$^{1}. In the case of large particles (sample SL-S26, 603 nm) it was not possible to perform the cell experiments with $7.9 \cdot 10^{16}$ particles per ml, therefore the amount was set 10 times lower, i.e. $0.79 \cdot 10^{16}$ particles per ml. For a comparison, the uptake of particles with 267 nm (sample SL-S30) was measured at both numbers of particles.

The flow cytometry data reveal that when the particles with the same solid content (equal total amount of polymer) are incubated with the cells, the same abundance of polymeric material is taken up; however the amount of particles inside the cells is much higher for the smaller particles. When the experiments were performed with the equal number of particles, the uptake of larger particles was much higher. This suggests that the uptake rather depends on the total amount of polymeric material present in the media than on the number of particles. The total particle's surface area does not correlate linearly with the uptake, thus indicating that there is no direct dependency between the total surface area and the cellular endocytotic process.
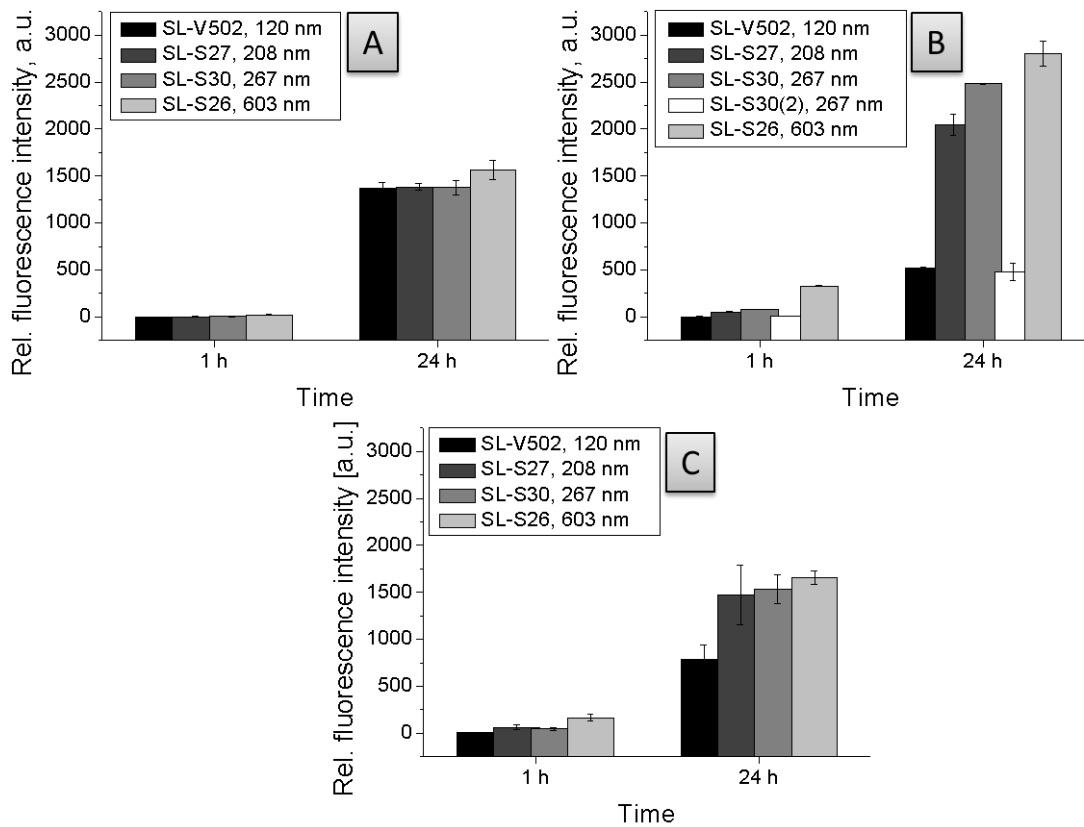
Figure 18: Uptake of positively charged polystyrene nanoparticles in HeLa cells as measured by flow cytometry keeping constant: A: polymer concentration at 75 µg · ml^{-1}; B: number of particles at 7.9 · 10^{16} particles per ml for samples SL-V502, SL-S27, SL-S30 and at 0.79·10^{16} particles per ml for samples SL-S30(2) and SL-S26; C: total interaction surface area at 2060 m^2 per ml.
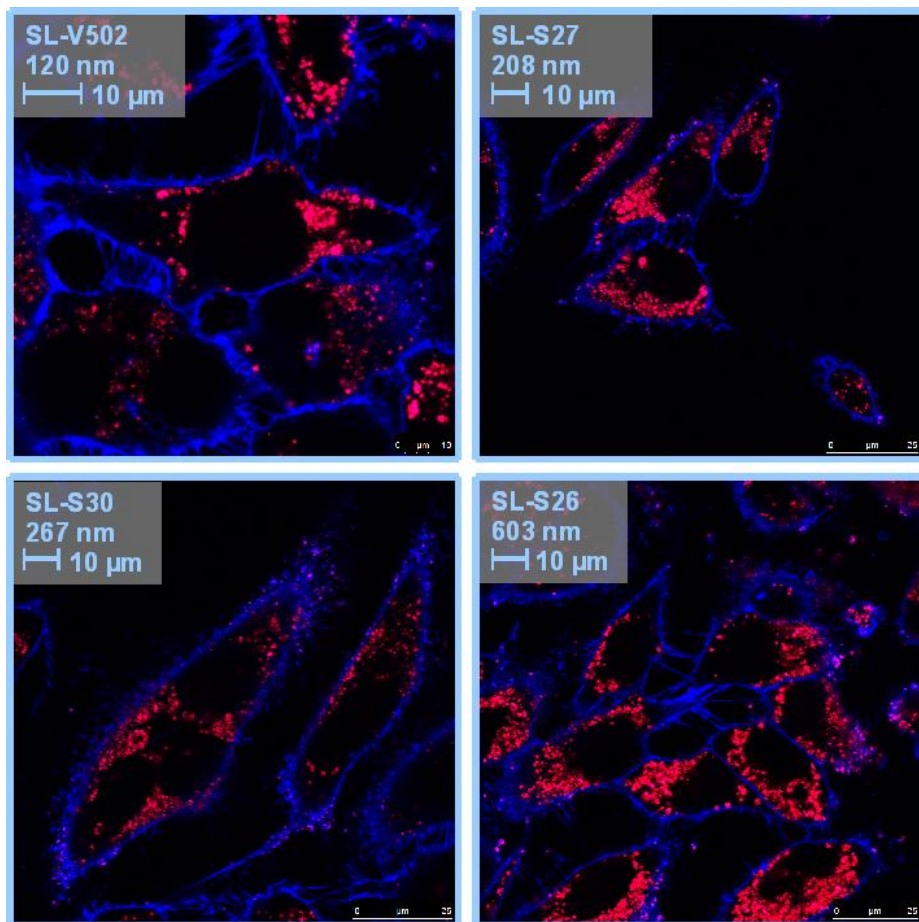
*Figure 19: cLSM images of HeLa cells after incubation for 24 h with 75 µg·ml⁻¹ of positively charged polystyrene particles stabilized with cationic surfactant, CTMA-Cl. The HeLa cell membrane is stained with DiD (blue) and particles are red in color.*

For the uptake of positively charged polystyrene particles an *excavator shovel* like mechanism is suggested that has a given maximum volume for each vesicle and a limited number of formed vesicles per time unit to take particles into the cells. The endocytotic processes and suggested mechanism is schematically shown Scheme 12.
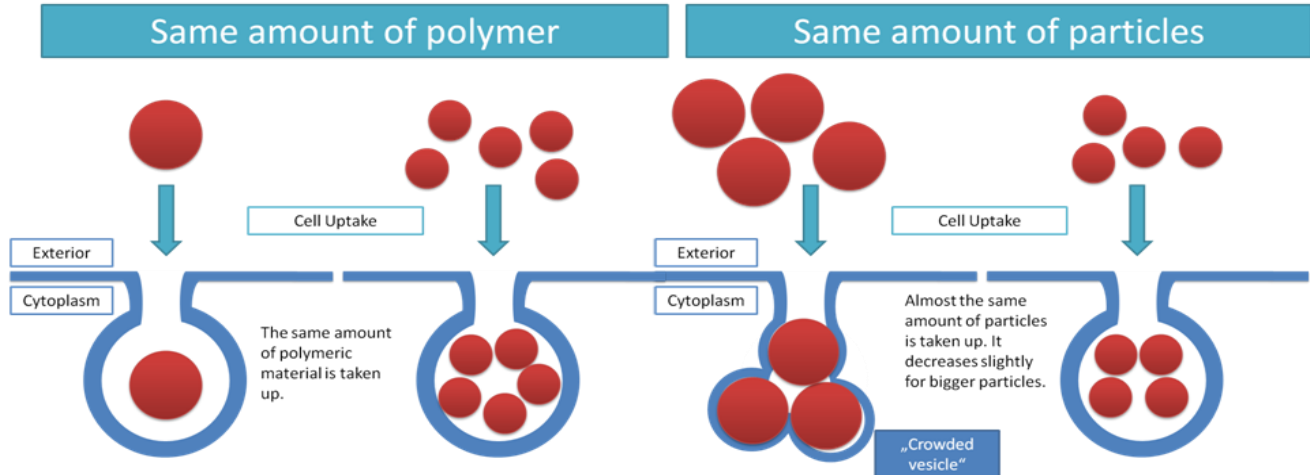
Scheme 12: Suggested scheme for the uptake of cationic polystyrene particles of different sizes into HeLa cells by an excavator shovel like mechanism.

To gain further insides in the endocytotic mechanism, the HeLa cells incubated with particles were studied with cryo-TEM by Dr. Martin Dass. As an example, HeLa cells with internalized particles of 603 nm (sample SL-S26) are presented in Figure 20. The *crowded vesicles* (compare Scheme 12) are clearly deformed and have a rather *cloverleaf* than round shape. Also, macropinocytotic cell ruffles which shape around a particle can be seen. This indicates that particles are taken up by an exvaginated, macropinocytosis-like mechanism that supports the previously explained *excavator shovel* theory concluded from the flow cytometry data.
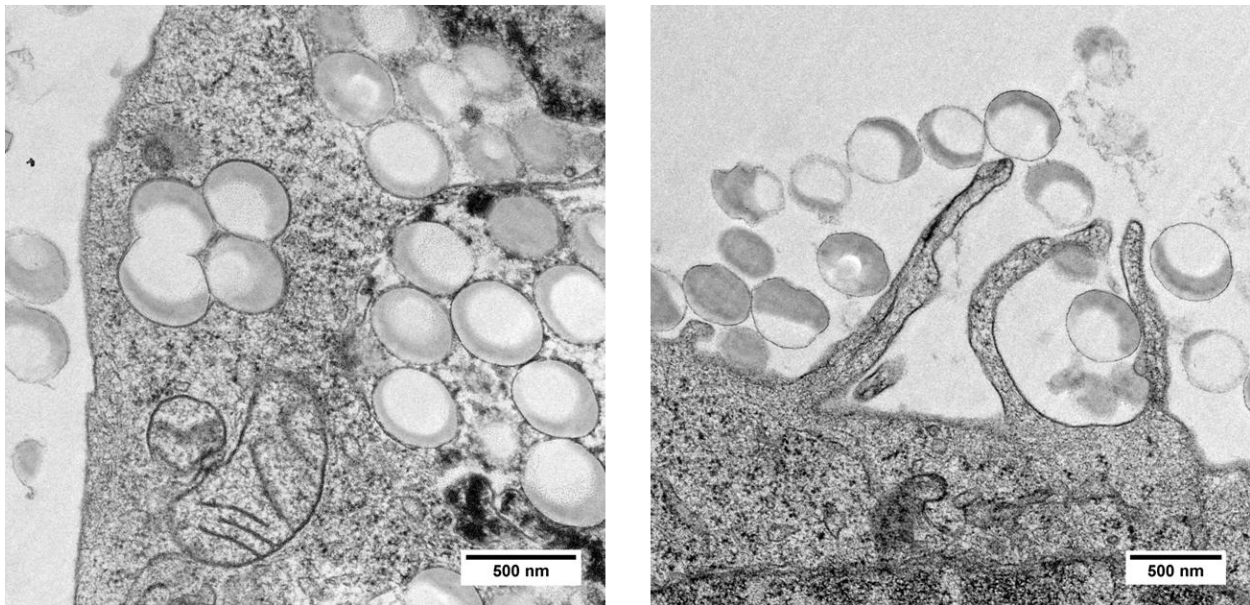
Figure 20: Cryo-TEM images of HeLa cells after incubation for 24 h with 603 nm positively charged polystyrene particles (SL-S26).

6.1.3 Blocking of endocytotic processes with specific inhibitors

The participation of certain proteins which are specific to endocytotic pathways can be blocked by using inhibitors. Four different inhibitors were studied and the results compared with each other. Cytochalasin D blocks the actin polymerization. Actin filaments participate in a whole variety of endocytotic processes. Most common, it is referred to as macropinocytosis. Chlorpromazine inhibits a Rho GTPase which is essential for the formation of clathrin-coated vesicles in clathrin-mediated endocytosis. EIPA lowers the submembraneos pH thus preventing a membrane ruffling which is necessary for macropinocytosis. Dynasore blocks the GTPase dynamin, which participates in the pinching off of the vesicle from the cell membrane. Magnesia and calcium are known to participate in the endocytotic process [135-137], ergo a buffer containing these ions is used. Different concentrations of inhibitors were tested. Figure 21 shows the particle uptake to HeLa cells with respect to an untreated control as measured by flow cytometry. For most inhibitors and particles, the uptake is dependent on the inhibitor concentration. However, a typical dose-response curve which features a sigmoidal shape cannot be observed although concentrations were chosen at a broad range. The sigmoidal shape comes about when the drug concentration reaches a critical minimum value when the concentration of

the drug is just high enough to initialize the inhibition and when it reaches a critical maximum value, i.e. when all possible pathways are blocked. All inhibitors show a general decrease in the uptake with an increase of the inhibitor concentration. An exception is chlorpromazine. The blocking of clathrin-mediated endocytosis leads to an increase of particle uptake until a concentration of 50 µM, for higher concentrations the uptake decreases. A possible explanation could be that the cell activates other endocytotic processes to compensate for the loss of clathrin-mediated endocytosis. These additional mechanisms affect also the uptake of NPs. For higher concentrations, the uptake decreases because of toxic effects. As can be seen in Figure 22, toxic effects of chlorpromazine are consistent with the decrease of NP uptake (> 75 µm).

The inhibitor values for final analysis were used at their highest concentration that still does not show any toxic effects. These values coincide very well with the previous experiments [130]. The percentage of alive, apoptotic and dead cells as determined by 7-AAD staining is shown in Figure 22. 7-AAD is a fluorescent dye that does not penetrate healthy cells. Upon apoptosis, the cell membrane becomes permeable and the dye stains the cytoplasm. Dead cells are stained in cytoplasm and the nucleus. Therefore, three distinct populations can be distinguished in flow cytometry, which refer to the above mentioned overall health states of the cells. The severest toxicity can be seen for the inhibitor chlorpromazine.
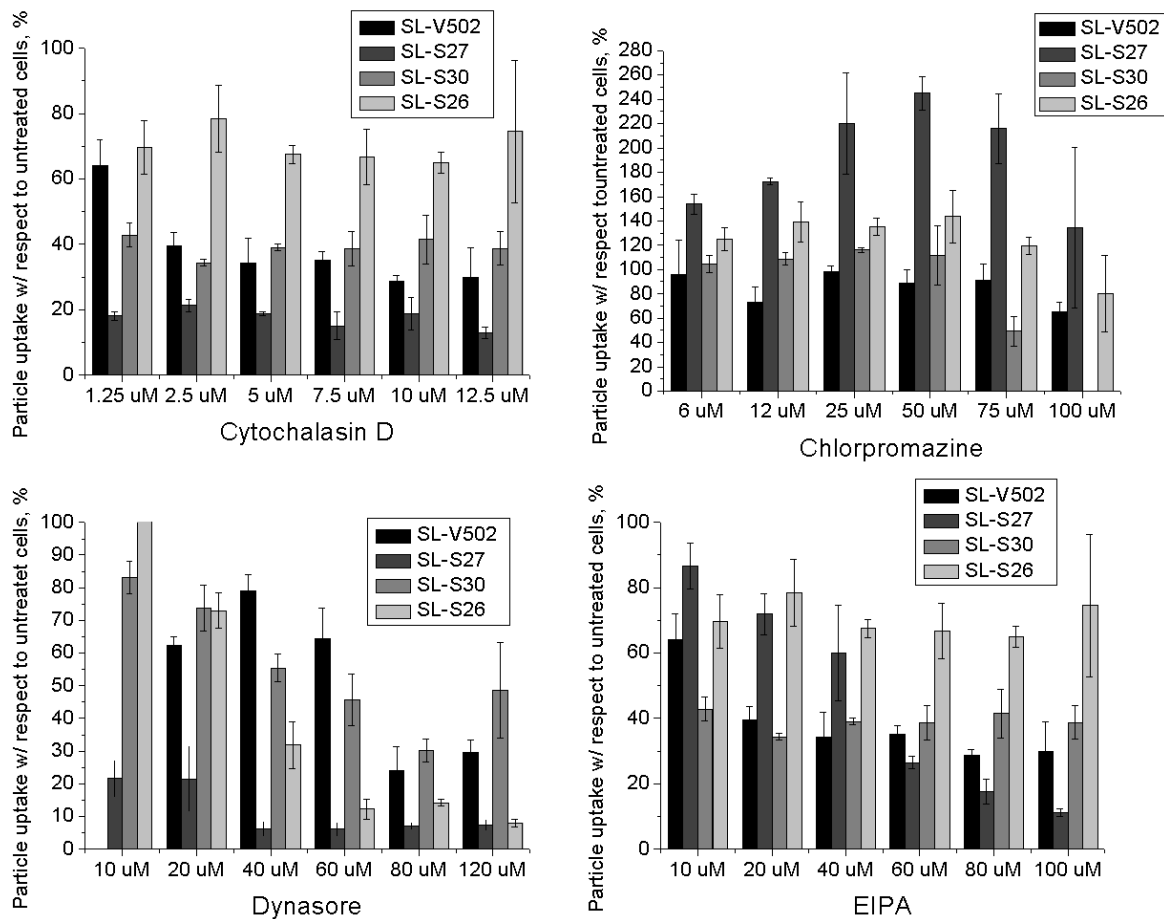
*Figure 21: Influence of different pharmacological inhibitors on the uptake of cationic NPs with different sizes as measured by flow cytometry. A detailed particle characteristic is given in Table 11. Cytochalasin D: Inhibition of actin filament formation; Chlorpromazine: Inhibition of clathrin-mediated endocytosis; Dynasore: Inhibition of dynamin-dependent endocytosis, EIPA: Inhibition of macropinocytosis.*
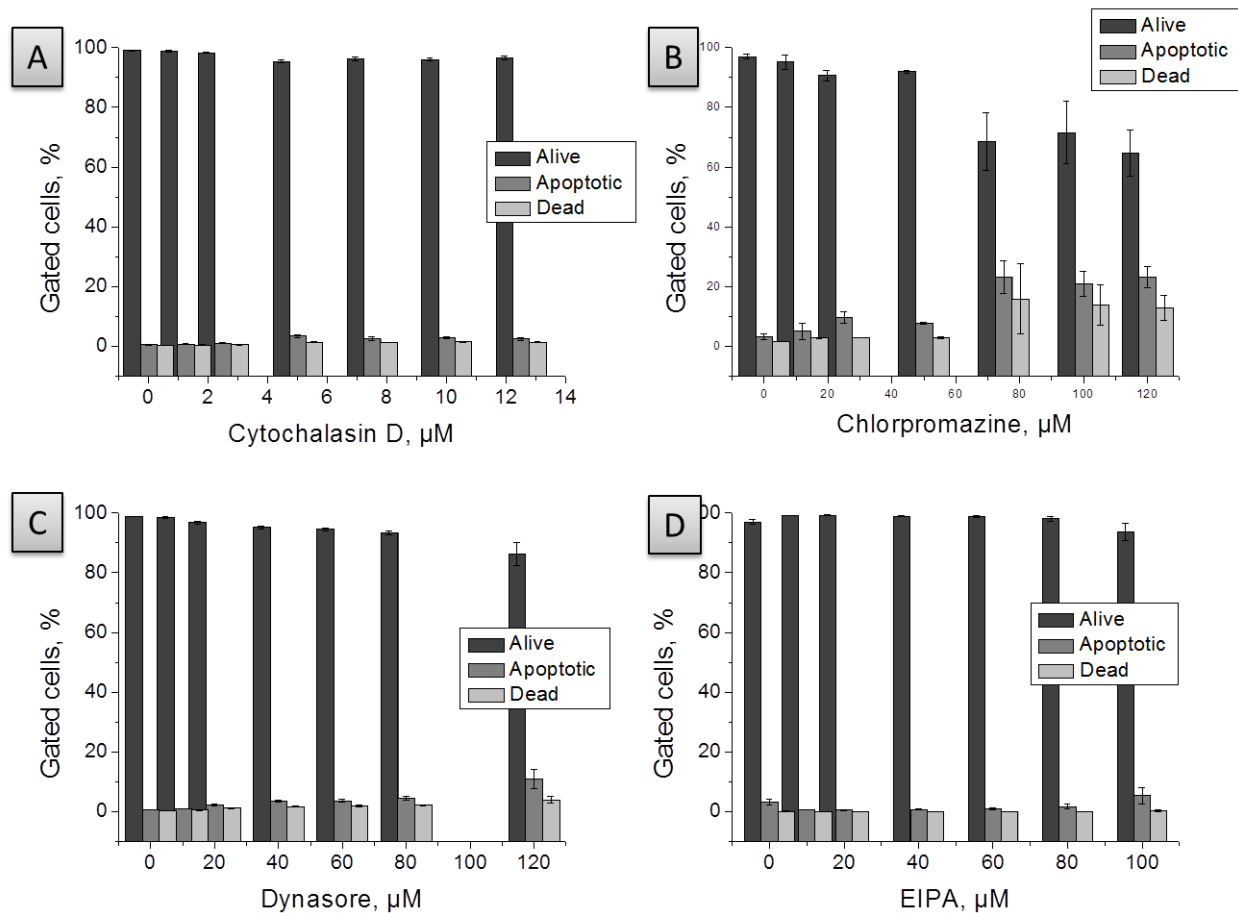
Figure 22: Toxic effects of the pharmacological inhibitors cytochalasin D, chlorpromazine, dynasore and EIPA at different concentrations as determined with 7-AAD staining in flow cytometry.

In Figure 23, the values for the highest concentration of each inhibitor that does not show any cell toxicity are shown. As can be seen, dynamin, and a form of macropinocytosis are essentially involved in the uptake of the nanoparticles in HeLa cells. Only the clathrin-dependent pathway can be excluded. This is expected for several reasons: on the one hand clathrin baskets, due to their geometry, can adopt only a maximum size of 100 nm. On the other hand clathrin-dependent uptake is a form of receptor-mediated endocytosis. Since the nanoparticles used here possess non-specific ammonium and amide chloride groups contributed by the surfactant and initiator, respectively, and no specific ligand is immobilized on the particle surface, a receptor-mediated pathway is unlikely.
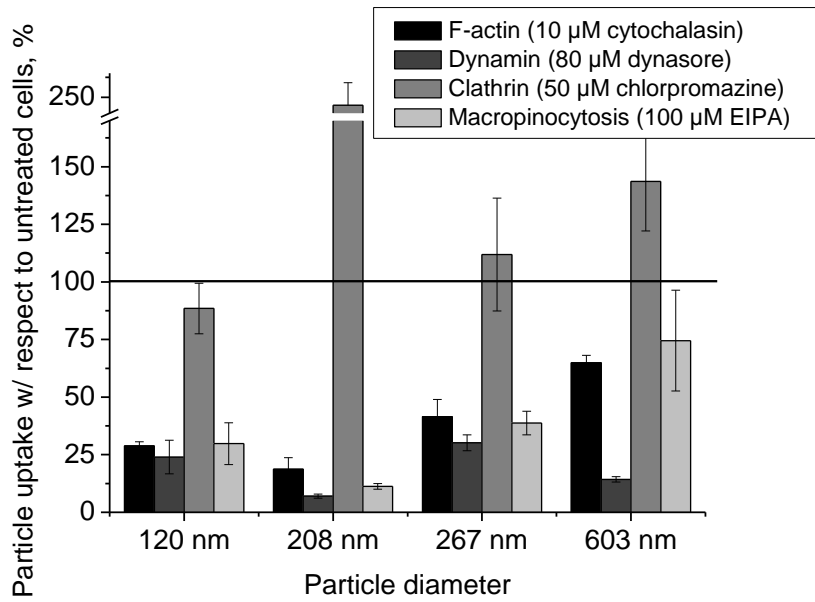
Figure 23: Relative uptake of nanoparticles under the influence of different inhibitors for F-actin, dynamin and clathrin mediated endocytosis as well as macropinocytosis referred to untreated cells. Untreated cells are set to 100%.

F-actin is known to participate in all endocytic pathways to contribute in several stages to the formation of the vesicles. Different points of attack for such participation are described [43]. It has been shown that endosomes, pinosomes, clathrin coated and secretory vesicles are associated in the cytoplasm with a so-called actin tail [44-46].

As has been shown here, the participation of dynamin on F-actin-dependent endocytosis is probable. The vesicles formed and transported by actin need to be pinched off by the GTPase dynamin. An involvement of actin is also important for macropinocytosis as described by Conner and Schmid [41]. Actin creates a membrane ruffle and protrusion of macropinocytotic arms into the exoplasma. Actin can participate both in the formation of invaginated vesicles into the cytoplasma as well as of membrane ruffles for macropinocytosis. Involvement of dynamin into macropinocytosis as well as inhibition of dynamin-dependent endocytosis by EIPA up to now was not described in the literature.

A significant difference in the uptake with regard to the NP size cannot be detected. All particles feature a similar blocking behavior which may suggest that all particles are taken up by a comparable endocytotic route.

The uptake mechanism is a kind of macropinocytosis, dependent on the formation of actin filaments as well as the small GTPase dynamin, responsible for the pinching off of vesicles from the membrane. While actin filaments are said to be responsible for the formation and transport of vesicles that are formed by invagination as well as by membrane ruffles on the outer side of the membrane [43], dynamin is reported to be participating only in the pinching off of invaginated endosomes, not in the formation of macropinocytotic vesicles [39, 48, 49].

Either, the particles are taken up by a dynamin-dependent macropinocytosis or two different endocytotic mechanisms, macropinocytosis and a form of unspecific invagination, such as e.g. caveolae-dependent endocytosis. This needed to be studied in further experiments.

6.1.4 Colocalization of particles with endocytotic proteins: Cytological staining

By staining specific proteins within a cell that participate in special endocytotic processes, a colocalization of these proteins with NPs can be detected. Cells were incubated for 24 h with the set of cationic NPs with different sizes as characterized in Table 11. After fixation and permeabilisation of the membrane, a set of different primary antibodies for caveolin-1, clathrin heavy chain, cathepsin D, Lamp1, M6PR and EEA1 is applied. A secondary antibody/Alexa488 conjugate labels the primary antibodies. The cell core is stained with a far-red DNA dye and imaging is performed with cLSM. In all following images, the antibody is colored green, the NPs red and the cell core blue. An overlay of green and red is shown as yellow. No bleed-through between the antibody and the nanoparticle occurs and the nonspecific staining of the 2AK is marginal, as can be seen in the control images in Figure 24. An accurate tuning of the cLSM hardware and software settings is essential for further data evaluation, because a bleed-through of the channels induces a false-positive colocalization signal.
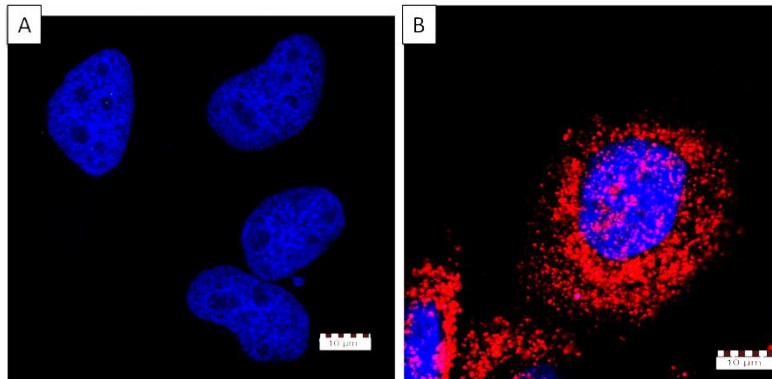
Figure 24: A: Negative control of HeLa cells stained with a DNA dye. B: HeLa cells incubated with the NP SL-S30 (red) and the 2AK (green). The nonspecific staining of the 2 AK is marginal and a bleed-through of the channels cannot be observed.

Each primary antibody features a unique staining profile due to the individual disposition of the proteins within the cell, as is shown in Figure 25. Most proteins are distributed in the cytoplasmatic vesicles. They are not present in the cell core (except for cathepsin D) and the Golgi apparatus (except for M6PR). M6PR is especially present in the Golgi and only lower concentrations are found in the cytoplasm. The NPs, regardless of their size, are spread throughout the cytoplasmatic vesicles, sparing the cell core and the Golgi, which is expected as the NPs enter the cell via endocytotic processes. For some stainings, a colocalization can be detected, especially with cav-1.

To quantify the colocalization, the ICQ values of the images are calculated. This coefficient expresses the co-increase or decrease of both channels. If a colocalization is present, both the intensity of the NPs and the antibody increase in comparison to the mean value in a set voxel. The opposite occurs for complete exclusion. An ICQ value of 0.5 is complete colocalization; -0.5 complete exclusion and values around 0 are considered random staining. However, for thorough data interpretation, the ICQ value needs to be supported by a graphic analysis. The PDM value, i.e. the ratio of the difference of both channels from the mean intensity, is correlated with the channel intensity. Constructed examples for 100% colocalization, random colocalization as well as exclusion can be found in chapter 5.2.5, Figure 5. This chapter also gives insights into the calculation of ICQ values. With higher intensity of the channel, the PDM ratio

also increases. A complete exclusion is a mirror image of a true colocalization plot. Random staining gives an hour glass form centered at 0.
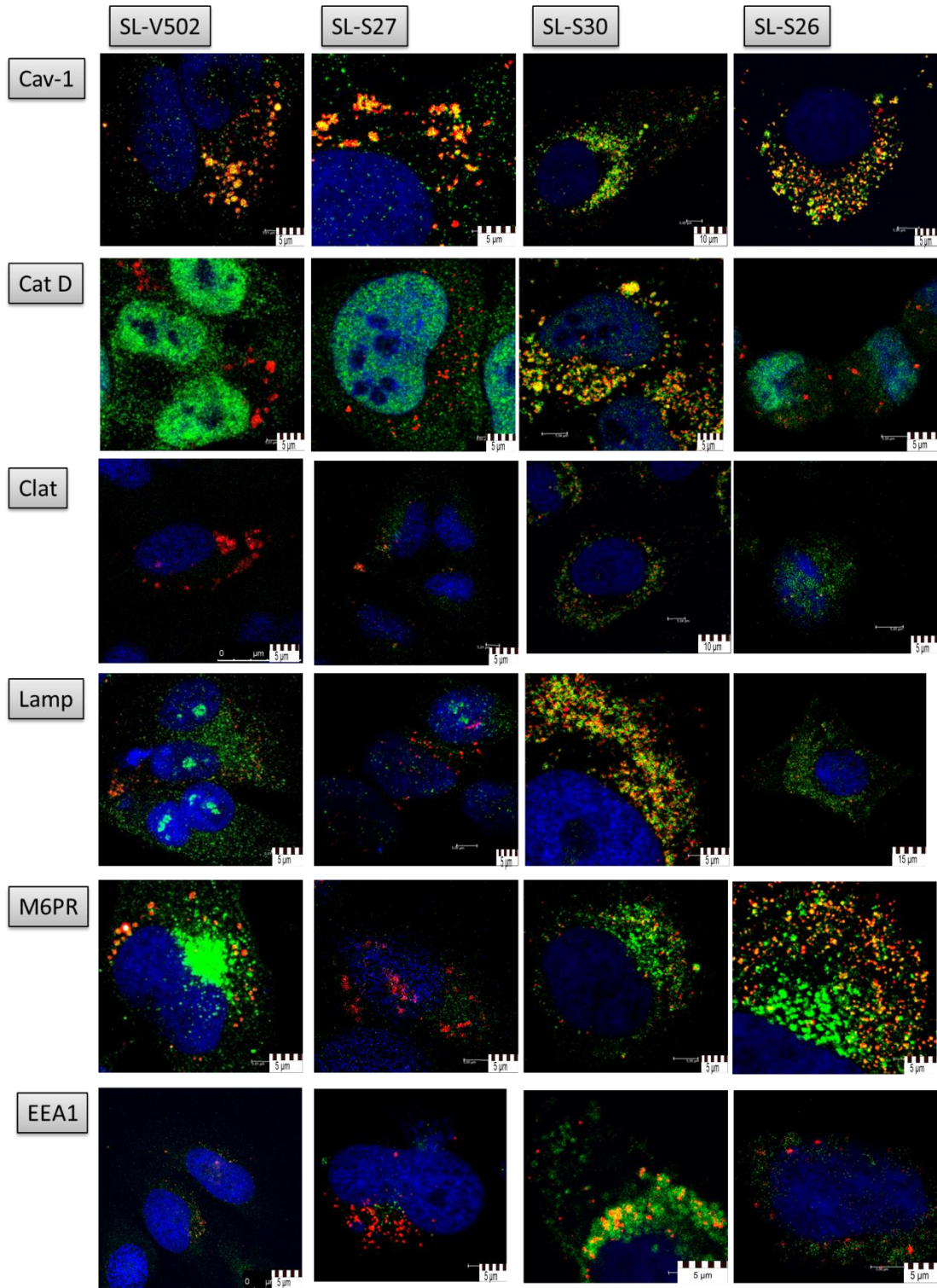
Figure 25: Immunecytochemical staining of HeLa cells with different antibodies (green) and pre-incubated 24 h with 75 µg · ml⁻¹ NPs. The characteristics of the particles are given in Table 11. The cell core is labeled blue.

The clathrin heavy chain protein is part of the clathrin lattice network. Uptake via clathrin is a receptor-mediated endocytosis, where receptor-bound ligands are accumulated and taken up into clathrin-coated vesicles. The clathrin heavy chain is quickly released from the vesicle after endocytosis and is returned to the cell membrane. Therefore, the clathrin-coated vesicle ICS probes only the immediate uptake mechanism and not any subsequent processes. The staining profile of clathrin is shown in Figure 26. The PDM plots of all NPs do not show a definite colocalization form, but the axis of the hour glass shape is not completely at zero, but at a slightly positive value. This indicates that only a very small amount of NPs colocalize with the clathrin antibody or that the random colocalization is more pronounced here. The ICQ value is also below 0.2. SL-S30/clat shows a higher value of > 0.3, which is not perceivable in the respective plot. Although a colocalization with clathrin cannot be completely excluded, especially for SL-S30/clat, if anything it is present only in a small amount and could also be due to random staining.

Caveolin is an integral membrane protein that is a part of specific type of lipid raft, called caveolae. From these lipid rafts, invaginations bud off from the cell membrane to form caveolin-labeled vesicles. The caveolin is removed from the vesicles at a later stage of the vesicle ripening. Unlike clathrin, caveolin is an integral membrane protein that needs to be returned to the membrane via endosomal transport. The caveolin ICS therefore probes the immediate uptake of NPs with caveolin but also some later endosomal stage, where caveolin is still part of the formed vesicles. The ICQ values, PDM plots and channel overlays for a specific ROI for caveolin ICC are presented in Figure 27. For the particles SL-V502 and SL-S26 the PDM plots indicate a strong colocalization; for SL-S27 and SL-S30 some random colocalization can be additionally depicted. The ICQ values are above and for SL-S30 and SL-S26 well above 0.25 indicating a colocalization of all particles with caveolin.

EEA1 serves as a membrane integrated marker protein for early endosomes. It is not present in vesicles newly budded from the cell membrane and in late endosomes or lysosomes. The EEA1 staining depicted in Figure 28 shows a partial colocalization for all NPs, although SL-S27 and

SL-S30 are slightly more pronounced than SL-S26. The ICQ value is approx. 0.2 or higher and almost all values in the PDM plot are positive.

The M6PR travels between the trans-Golgi network and late endosomes, where it participates in the transportation of M6P-tagged proteins. For M6PR, the two smaller particles SL-V502 and SL-S27 do not show a colocalization neither in the PDM plots nor the ICQ values (see Figure 29). SL-S30 has a distinct higher ICQ value and a PDM plot that indicates real colocalization in addition to random staining. For the biggest particle, both ICQ value and PDM plot show a considerable colocalization. M6PR is therefore the only staining which exhibits a size-dependent colocalization.

The protease cathepsin D becomes activated at the low pH typical for lysosomes. For cathepsin D, as shown in Figure 30, all PDM plots express the typical butterfly or hour glass form of random staining. The ICQ values are between 0.1 and 0.2, whereupon the bigger NP SL-S30 and SL-S26 also feature the higher ICQ values. This might indicate that with a higher particle size the chance for random colocalization increases and explain, why although expressing a random staining in the PDM plots, the ICQ values are not zero, but slightly higher (between approx. 0.1 and 0.2). In conclusion, a colocalization with cathepsin D cannot be detected for all NPs. However, as cathepsin D is not an integral membrane protein, it could be released from the lysosomes upon permeabilisation with a surfactant to allow the antibodies to cross the cell membrane. If that is the case, cathepsin D would be dispensed throughout the cytoplasm without any distinct staining. The staining profile of cathepsin D does not indicate a complete dispersion of the protein. However, to backup lysosomal colocalization, the membrane integrated protein Lamp1 is also tested.

Lamp1 is a membrane glycoprotein that can be found in lysosomes, where it participates in the sorting process. Once Lamp1 has been transported to the lysosomes, its turnover is restricted to these compartments as lysosomes undergo a permanent fission and fusion process. The Lamp1 ICS therefore probes the colocalization in lysosomes. Lamp1 features a colocalization profile comparable to clathrin, as it is shown in Figure 31. A definite colocalization cannot be concluded from the hour glass shape of the PDM plots, although their axis is at a slightly positive value,

which may be a more pronounced random staining or true colocalization at a very low amount. The ICQ values are also below 0.2. Although a colocalization with Lamp1 cannot be completely excluded, if anything it is present only in a small amount and could also be due to random staining. Particles may colocalize in a very small amount or not at all with lysosomal structures. In addition, more particles may be present in lysosomes after a longer incubation time. Due to an acidification of the particle environment as is shown later, particles may still be present in lysosomes that are not tagged with Lamp1.

Clathrin

	SL-V502 120 nm	SL-S27 208 nm	SL-S30 267 nm	SL-S26 603 nm
A				
B				
C				
D	0.184	0.178	0.311	0.125
E	0.239	0.210	0.310	0.201
F	0.047	0.032	0.007	0.098
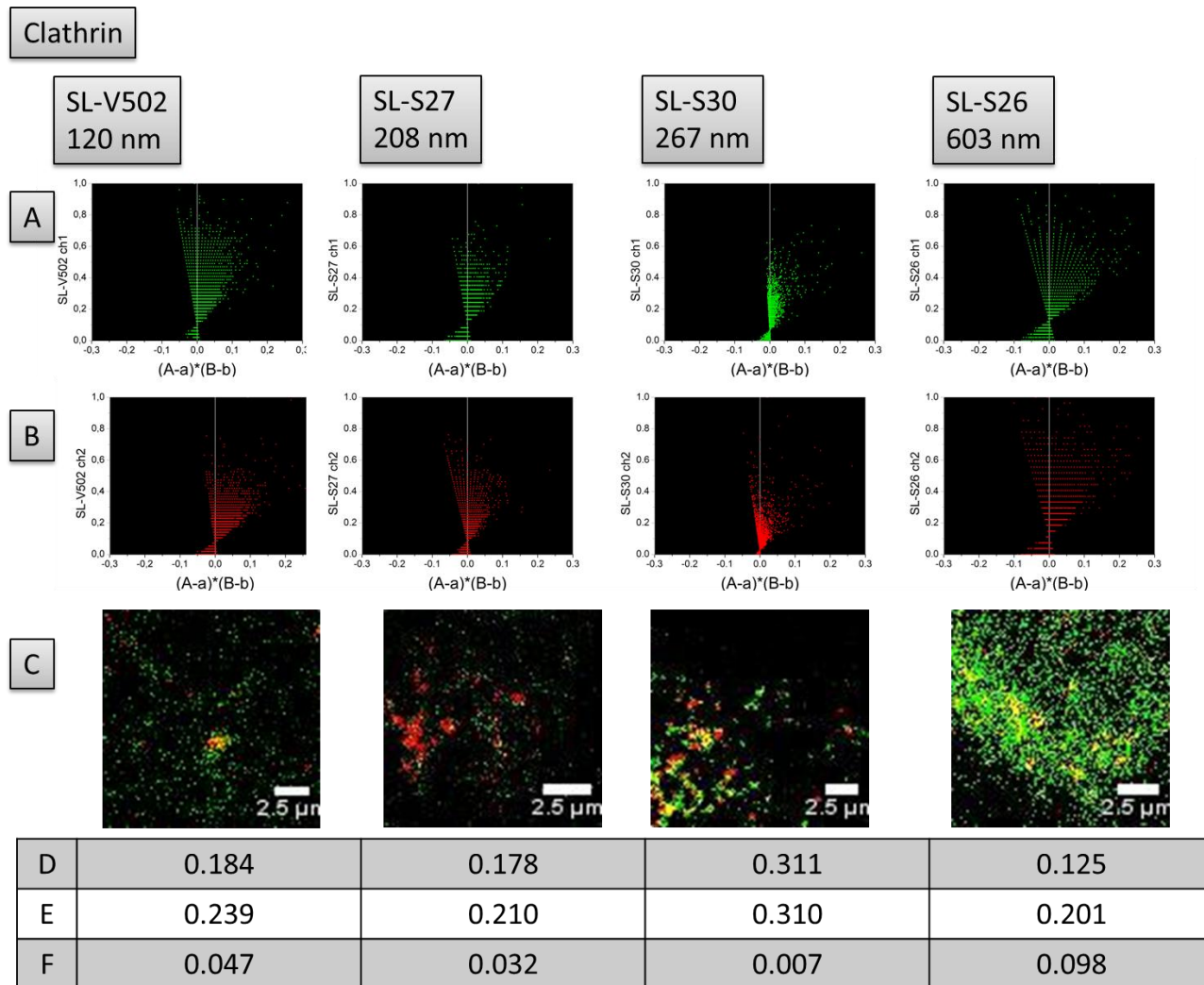
Figure 26: Immunocytological staining of NPs with clathrin antibodies. The characteristics of the particles are given in Table 11. A: Diagram of the PDM values in correlation to the fluorescence intensity of the antibody (channel 1, green); B: Diagram of the PDM values in correlation to the fluorescence intensity of the NPs (channel 2, red); C: Merged image of the selected region of interest used for the calculations; D: ICQ value for the selected region of interest as depicted in C; E: mean ICQ (triplicate); F: standard deviation of the mean ICQ.

Caveolin-1

	SL-V502 120 nm	SL-S27 208 nm	SL-S30 267 nm	SL-S26 603 nm
D	0.256	0.257	0.319	0.332
E	0.200	0.185	0.300	0.317
F	0.053	0.063	0.020	0.071
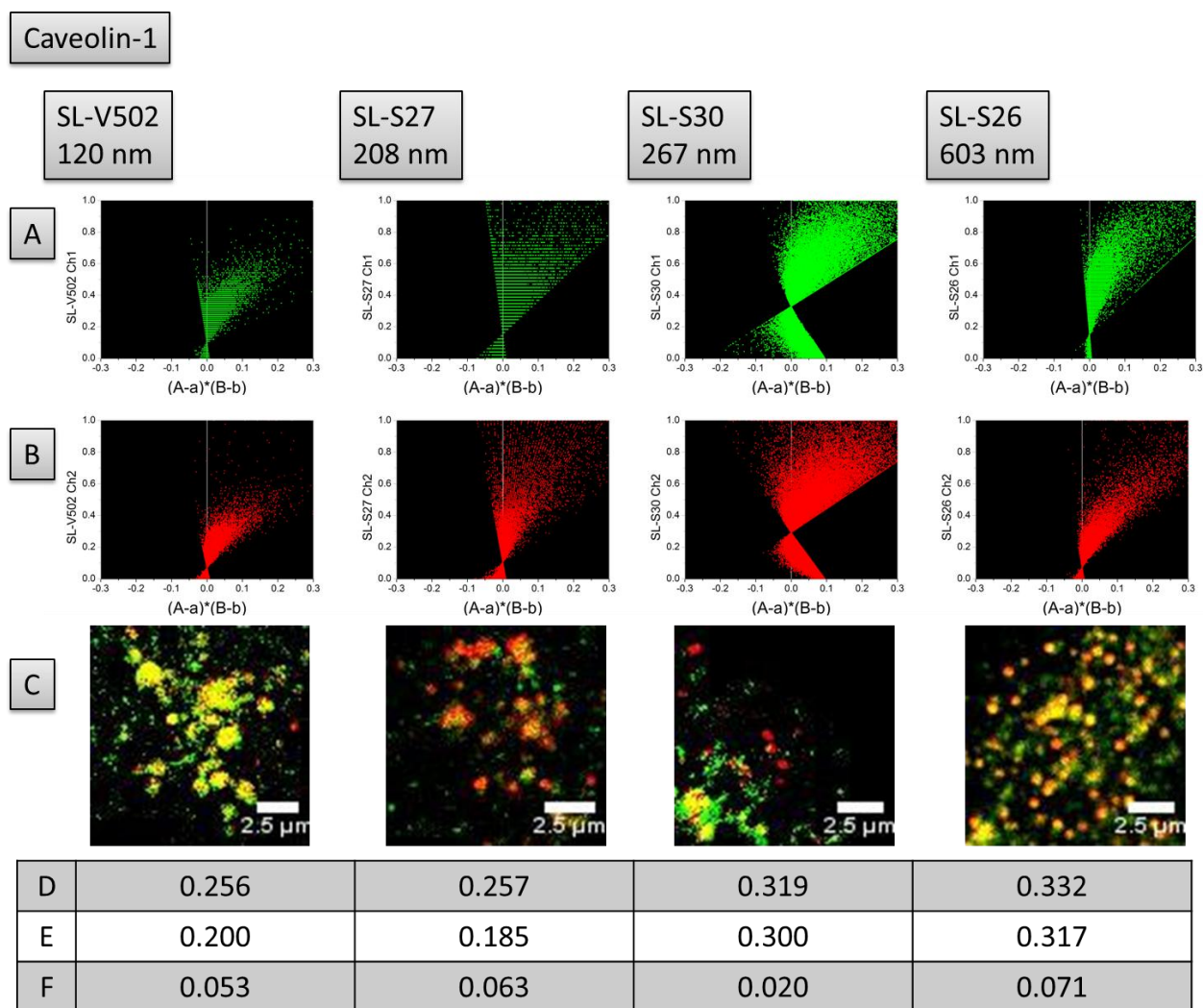
Figure 27: Immunocytological staining of NPs with caveolin antibodies. The characteristics of the particles are given in Table 11. A: Diagram of the PDM values in correlation to the fluorescence intensity of the antibody (channel 1, green); B: Diagram of the PDM values in correlation to the fluorescence intensity of the NPs (channel 2, red); C: Merged image of the selected region of interest used for the calculations; D: ICQ value for the selected region of interest as depicted in C; E: mean ICQ (triplicate); F: standard deviation of the mean ICQ.

EEA1

	SL-V502 120 nm	SL-S27 208 nm	SL-S30 267 nm	SL-S26 603 nm
D	0.192	0.229	0.307	0.184
E	0.261	0.219	0.278	0.189
F	0.032	0.027	0.095	0.010
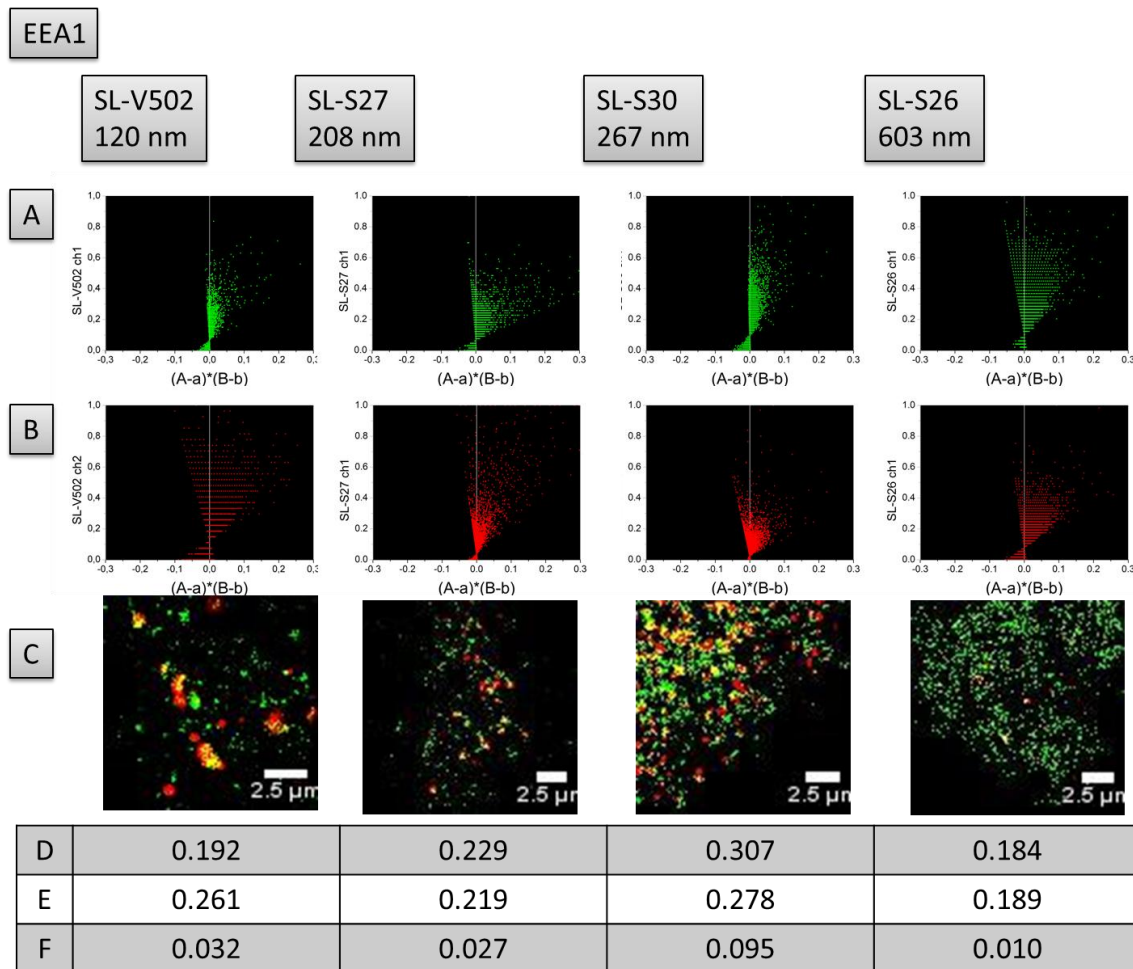
Figure 28: Immunocytological staining of NPs with EEA1 antibodies. The characteristics of the particles are given in Table 11. A: Diagram of the PDM values in correlation to the fluorescence intensity of the antibody (channel 1, green); B: Diagram of the PDM values in correlation to the fluorescence intensity of the NPs (channel 2, red); C: Merged image of the selected region of interest used for the calculations; D: ICQ value for the selected region of interest as depicted in C; E: mean ICQ (triplicate); F: standard deviation of the mean ICQ.
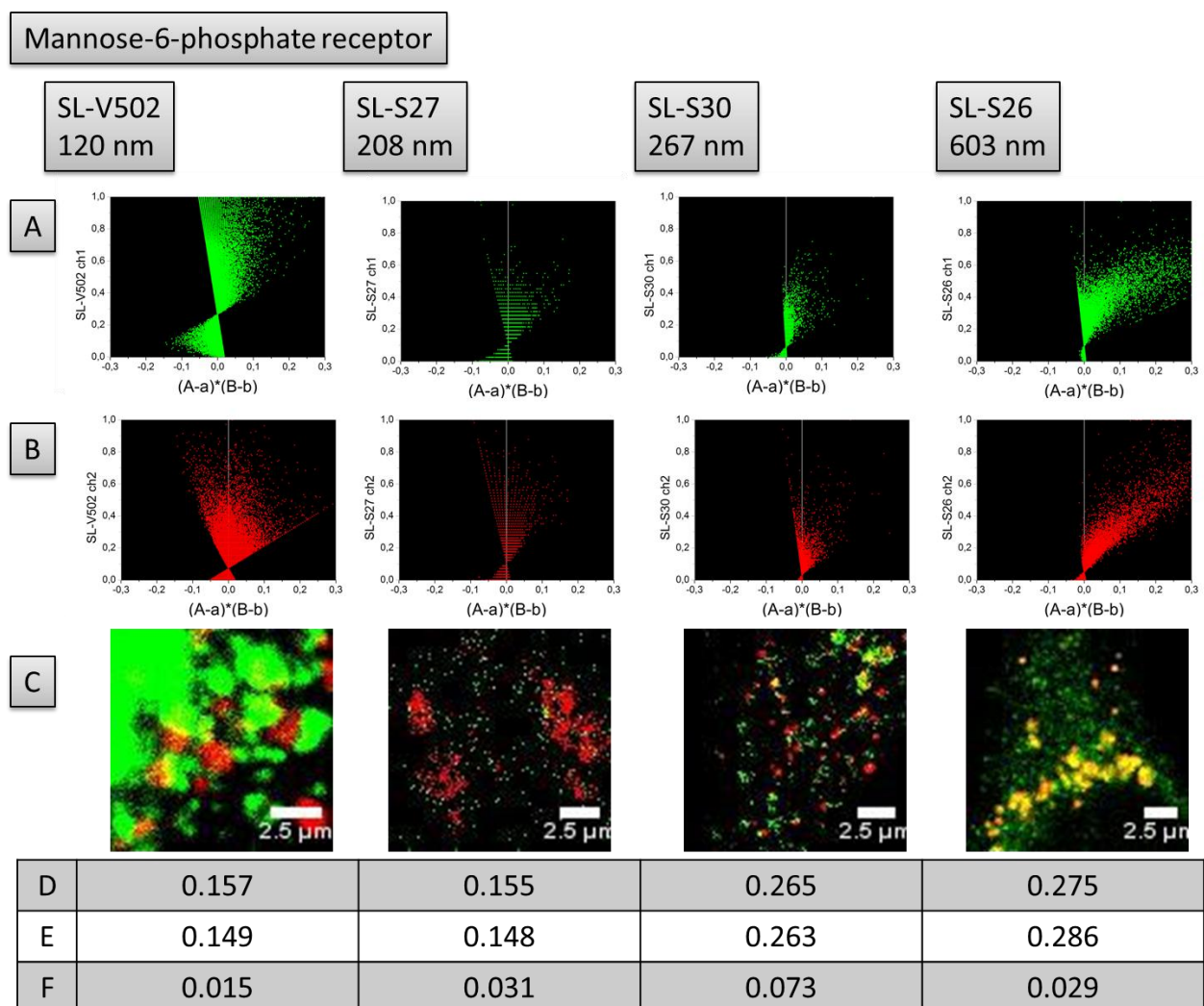
Figure 29: Immunocytological staining of NPs with M6PR antibodies. The characteristics of the particles are given in Table 11. A: Diagram of the PDM values in correlation to the fluorescence intensity of the antibody (channel 1, green); B: Diagram of the PDM values in correlation to the fluorescence intensity of the NPs (channel 2, red); C: Merged image of the selected region of interest used for the calculations; D: ICQ value for the selected region of interest as depicted in C; E: mean ICQ (triplicate); F: standard deviation of the mean ICQ.
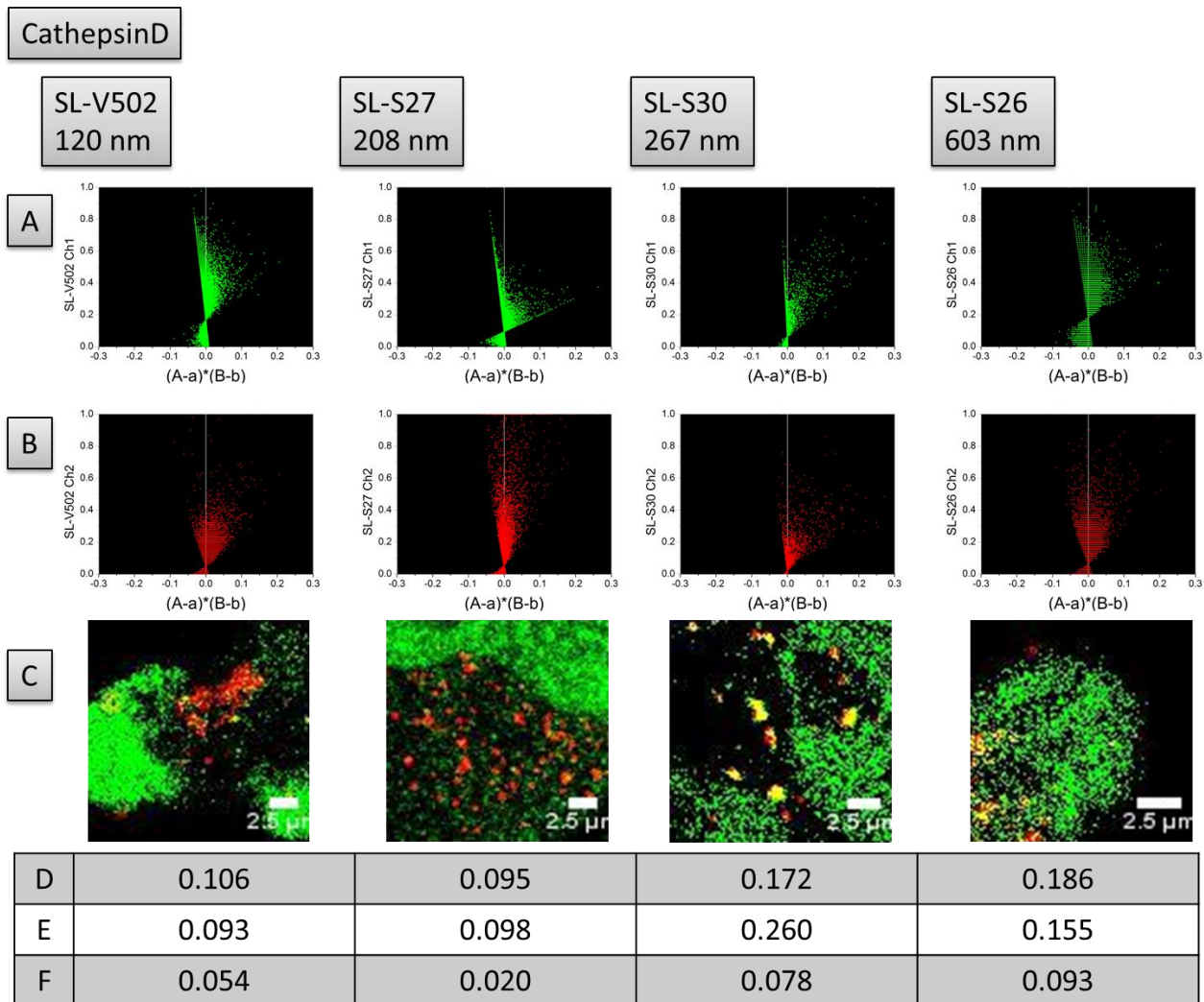
Figure 30: Immunocytological staining of NPs with cathepsin D antibodies. The characteristics of the particles are given in Table 11. A: Diagram of the PDM values in correlation to the fluorescence intensity of the antibody (channel 1, green); B: Diagram of the PDM values in correlation to the fluorescence intensity of the NPs (channel 2, red); C: Merged image of the selected region of interest used for the calculations; D: ICQ value for the selected region of interest as depicted in C; E: mean ICQ (triplicate); F: standard deviation of the mean ICQ.

Lamp1

| SL-V502 120 nm | SL-S27 208 nm | SL-S30 267 nm | SL-S26 603 nm |
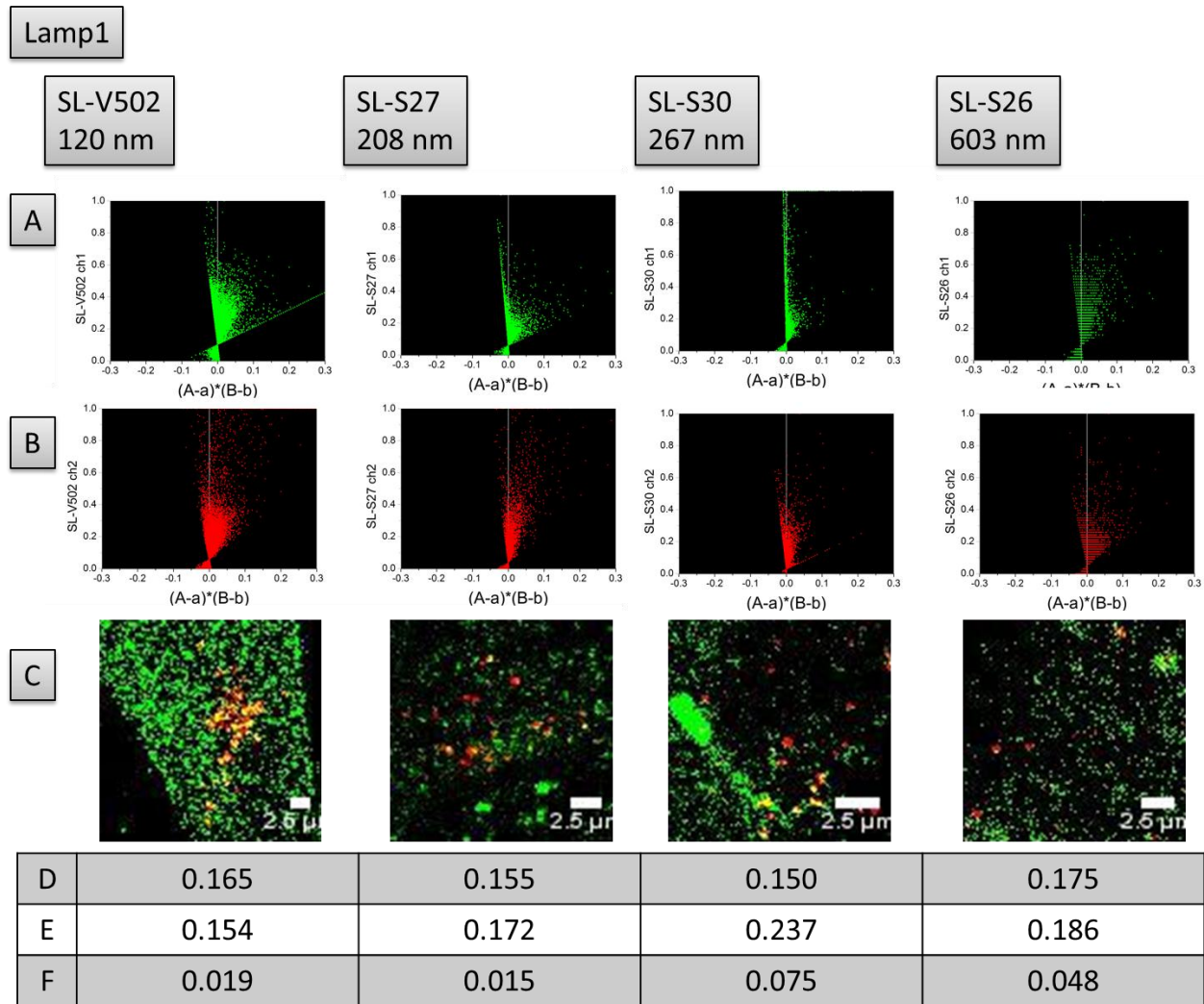
Figure 31: Immunocytological staining of NPs with Lamp1 antibodies. The characteristics of the particles are given in Table 11. A: Diagram of the PDM values in correlation to the fluorescence intensity of the antibody (channel 1, green); B: Diagram of the PDM values in correlation to the fluorescence intensity of the NPs (channel 2, red); C: Merged image of the selected region of interest used for the calculations; D: ICQ value for the selected region of interest as depicted in C; E: mean ICQ (triplicate); F: standard deviation of the mean ICQ.

	SL-V502 120 nm	SL-S27 208 nm	SL-S30 267 nm	SL-S26 603 nm
D	0.165	0.155	0.150	0.175
E	0.154	0.172	0.237	0.186
F	0.019	0.015	0.075	0.048

An overview over the colocalization found is given in Table 13. In conclusion, caveolin is involved in the uptake of NPs of all sizes. A participation of cathepsin D, clathrin and LAMP1 cannot be detected. A small part of NPs colocalize with EEA1 and NPs with bigger size (> 267 nm) colocalize with M6PR. An uptake via clathrin-mediated endocytosis for the NPs is not unexpected as clathrin is known for receptor-mediated endocytosis of small vesicles (< 100nm [138]), that do not fit for NPs > 120 nm as are used in this study. An exclusion of both lysosomal

proteins LAMP1 and cathepsin D is surprising. Either the NPs are not present in lysosomes or alternatively in lysosomes that are not encoded with LAMP1 and cathepsin D or they are not probed with this method. It could be that a longer incubation would lead to a colocalization of NPs with lysosomal proteins, as is discussed in chapter 6.2 (Sensor nanoparticles to probe the intracellular pH). However, incubation times of 72 h led to an increased uptake of NPs to the HeLa cells, so that distinguished colocalization studies could not be performed. Figure 32 displays an exemplary image of NPs (SL-S26) incubated for 72 h with HeLa cells. As can be seen, the cell is crowded with vesicles (except for the region of Golgi apparatus and the cell core) so that a distinguished conclusion regarding the colocalization of particles with the antibodies is not possible.
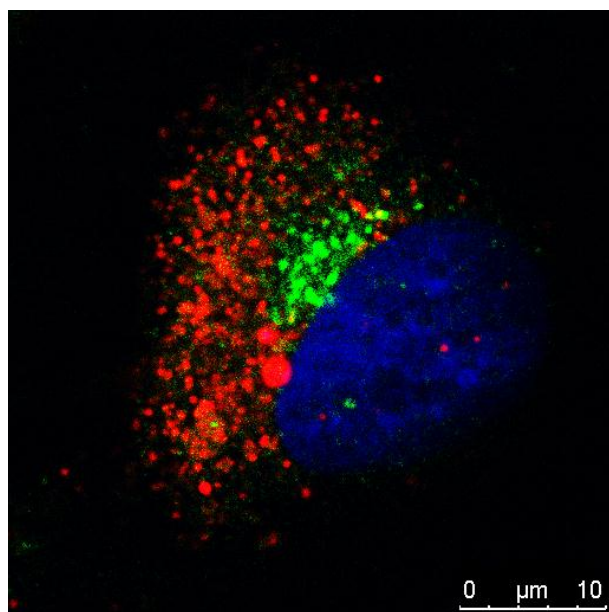

Figure 32: Immunecytochemical staining of HeLa cells with M6PR antibody (green) and pre-incubated 72 h with 75 µg · ml⁻¹ NPs (SL-S26). The characteristics of the particles are given in Table 11. The cell core is labeled blue.

On the other hand, incubation times of 1 – 2 h yielded too little NP fluorescence signals for colocalization studies. As mentioned before, it is possible that cathepsin D is released into the cytoplasm upon permeabilization of the cells. However, this is not valid for the membrane-integrated Lamp1. Immunocytological staining can only be considered as a snapshot at a certain time. If no colocalization is found, it cannot be concluded that none occurs. The M6PR travels

mainly between the trans-Golgi network and the late endosome. NPs do not seem present in the Golgi, which is a bright fluorescent area next to the nucleus. Therefore the bigger NPs that colocalize with the M6PR must be localized within the late endosome. It remains questionable if the size of the NPs is responsible for the colocalization.

From these results, NPs are taken up by cells via a caveolin-mediated endocytosis and are then transported to early and late endosomes. They cannot be found in lysosomes that are encoded with Lamp1 and cathepsin D.

Table 13: Colocalization of NPs with different endocytotic proteins as determined by ICQ values and PDM plots after 24 h incubation.

Sample	D_i, nm	Cav-1	Cat D	Clathrin	Lamp1	M6PR	EEA1
SL-V502	120	++	-	0	0	0	+
SL-S27	208	+	-	0	0	0	+
SL-S30	267	++	0	0	0	+	+
SL-S26	603	++	0	0	0	++	+

++: clear colocalization; +: partial colocalization; 0: random colocalization; -: exclusion.

6.1.5 *Colocalization of particles with endocytotic proteins: live cell labeling by the expression of fluorescent caveolin*

HeLa cells can express a fluorescent variant of caveolin, when a DNA construct is introduced into the cells. Caveolin is the main protein in so called caveolae, a specific type of lipid rafts. Colocalization of NPs with caveolin in ICS (see chapter 6.1.4) proved successful in previous experiments. However, as has been discussed before, the probing of endocytotic processes should always be performed as a set of techniques to eliminate the flaws of each method. In order to validate the results from the immunocytological staining, we used GFP-tagged caveolin for confirmation.

Two different EGFP-tagged variants of caveolin were expressed in the cells: a construct with C-terminally fused EGFP (caveolin-EGFP, CE) and one with N-terminally fused EGFP (EGFP-

caveolin, EC). The latter is described to inhibit caveolin-mediated endocytosis as a dominant negative mutant [120, 131]. Cholera toxin subunit B (CTB), which is used as a control, is known to enter cells mainly via caveolin-mediated endocytosis [139, 140] and can therefore be used as a positive control.

The set of positively charged particles with different sizes is inhibited with CE or EC expressing cells. The cLSM images after 24 h (see Figure 33) reveal that the constructs severely disturb the endocytotic mechanism. Particles taken up to untreated cells are regularly distributed throughout the cells and are taken up at a high rate. However, the particle uptake is considerably decreased in cells expressing one of the mutant proteins. This effect is more pronounced for smaller particles, where only very large particles enter the cell. The uptake of NPs to undifferentiated cells remains undisturbed, as non-fluorescent cells in the vicinity of differentiated cells express the same NP uptake pattern as the untreated control. This suggests that a) the caveolin-mediated endocytosis is disturbed by both constructs and b) NPs enter the cell by a caveolin-dependent pathway. As the effect is strongest for small particles (sample SL-V502), it hints that beside caveolin-mediated endocytosis larger NPs enter the cell via a competitive pathway. If the constructs are prone to disturb caveolin-mediated endocytosis, cells may also switch-on emergency side pathways that affect mainly larger particles. Alternatively, the transfection may affect major uptake routes and the observed effect is therefore unspecific.

The uptake of CTB is shown in Figure 34. CTB is endocytosed by both CE and EC cells, although CTB does not show the same distribution pattern as caveolin. Although CTB is not exclusively taken up by caveolin-mediated endocytosis, other pathways for CTB uptake contribute to a lesser extent. The exclusion of CTB and fluorescent caveolin also indicates a dysfunction of the caveolae machinery.
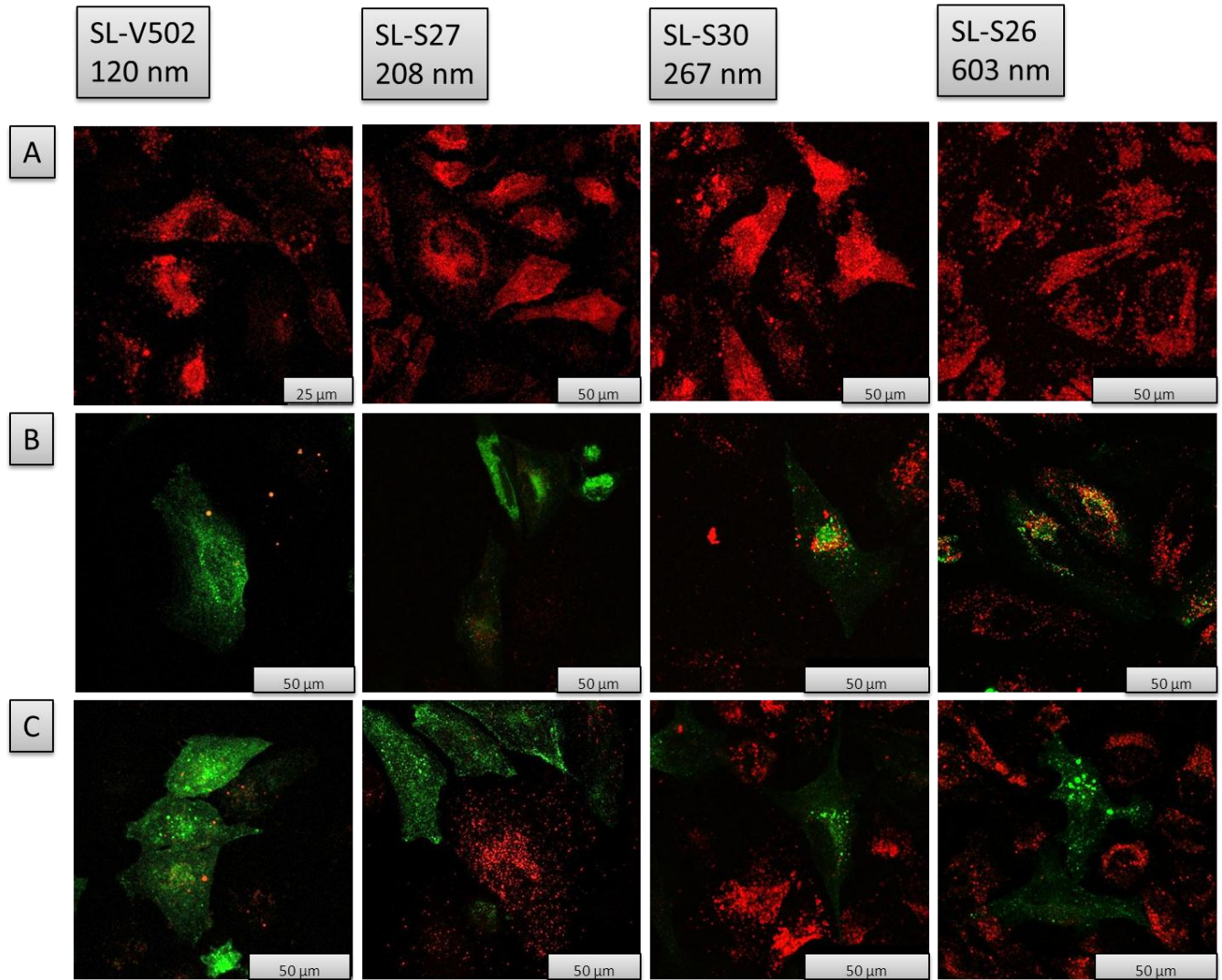
Figure 33: LSM images of HeLa cells expressing caveolin-EGFP (CE) or EGFP-caveolin (EC, green) that were incubated for 24 h with 75 µg · ml⁻¹ cationic NPs (red) with different sizes. The characteristics of the particles are given in Table 11. A: Untreated cells; B: CE expressing cells; C: EC expressing cells.
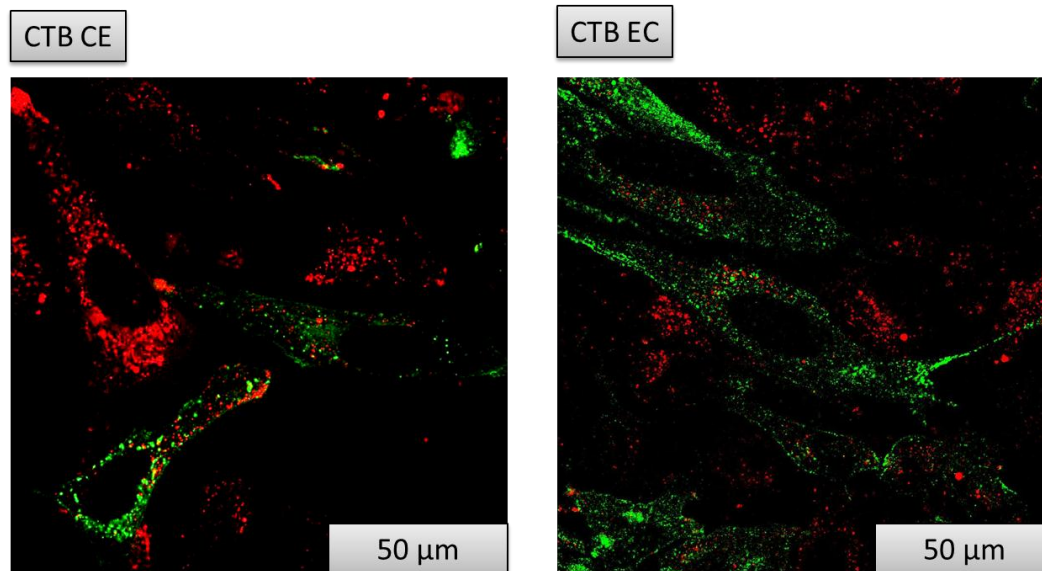
Figure 34: LSM images of cholera toxin B (red) with caveolin-EGFP (CTB CE, green) and EGFP-caveolin (CTB EC, green) expressing HeLa cells.

The colocalization rate of caveolin and NPs or CTB is quantified by determining the ICQ coefficient and plotting the PDM values, similar to the procedure for the ICS colocalization described in chapter 6.1.4. The PDM plots and ICQ values for HeLa cells expressing CE or EC and incubated with the cationic NPs with different sizes are displayed in Figure 35 and Figure 36, respectively. Most of the cells either show a high expression of fluorescent caveolin or have taken up NPs at a significant rate. ROI for colocalization analysis were chosen from transfected cells where NPs could still be discovered. For the uptake of the large particle fraction of sample SL-V502, a clear colocalisation for single particles with CE can be found. Other large particles of the same sample show no colocalization (data not shown), which is indicated by the high standard deviation of the ICQ coefficient. A clear colocalization is also present for SL-S6 EC. The PDM plot shows a curve progression typical for non-random colocalization, the ICQ value is at 0.240 and the colocalization can be seen as a yellow color. The hour glass shape of the PDM plot eliminates the possibility for true colocalization and suggest random staining.
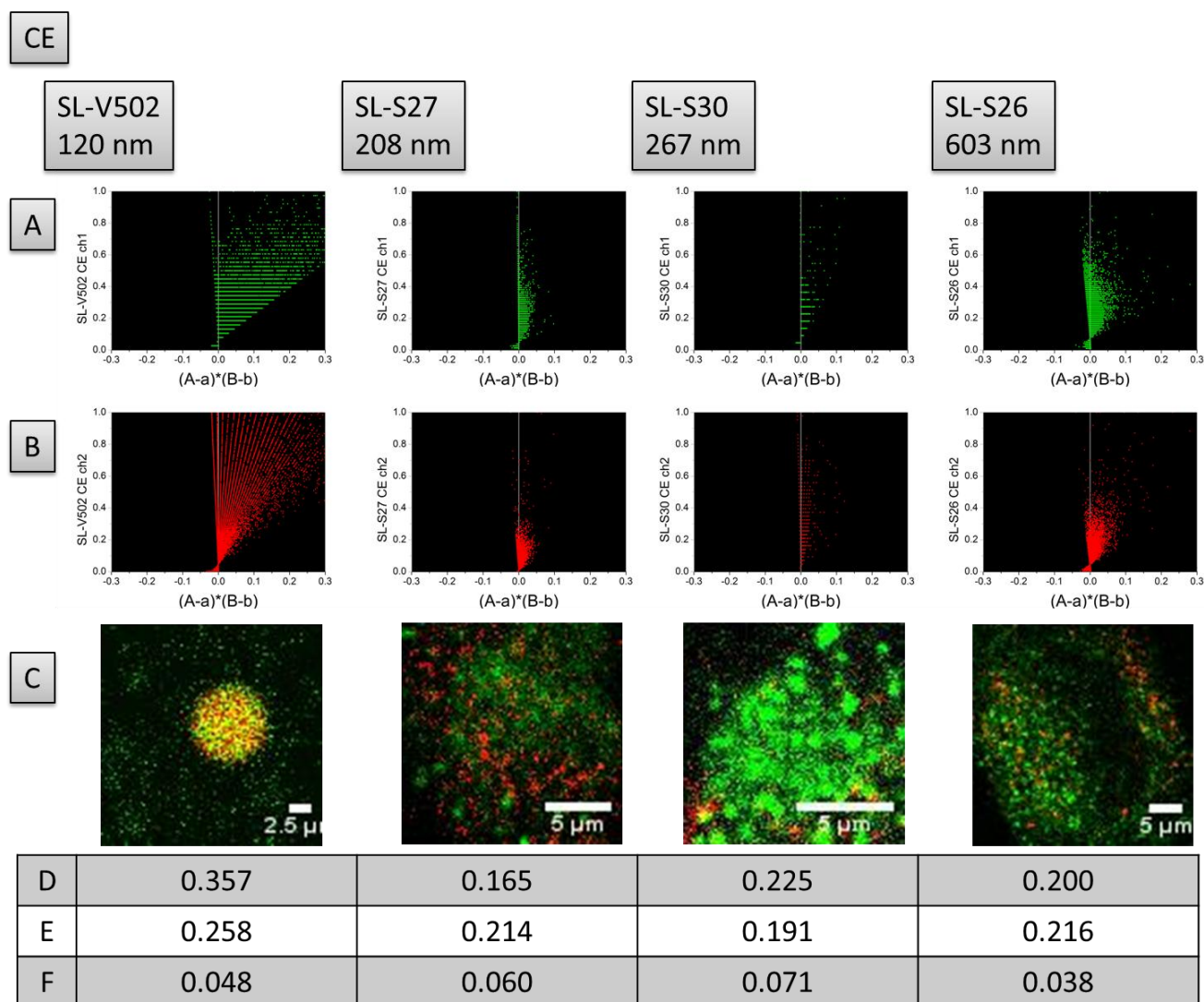
Figure 35: HeLa cells expressing fluorescent CE and incubated with cationic NPs with different sizes. The characteristics of the particles is given in Table 11. A: Diagram of the PDM values in correlation to the fluorescence intensity of CE (channel 1, green); B: Diagram of the PDM values in correlation to the fluorescence intensity of the NPs (channel 2, red); C: Merged image of the selected region of interest used for the calculations; D: ICQ value for the selected region of interest as depicted in C; E: mean ICQ (triplicate); F: standard deviation of the mean ICQ.
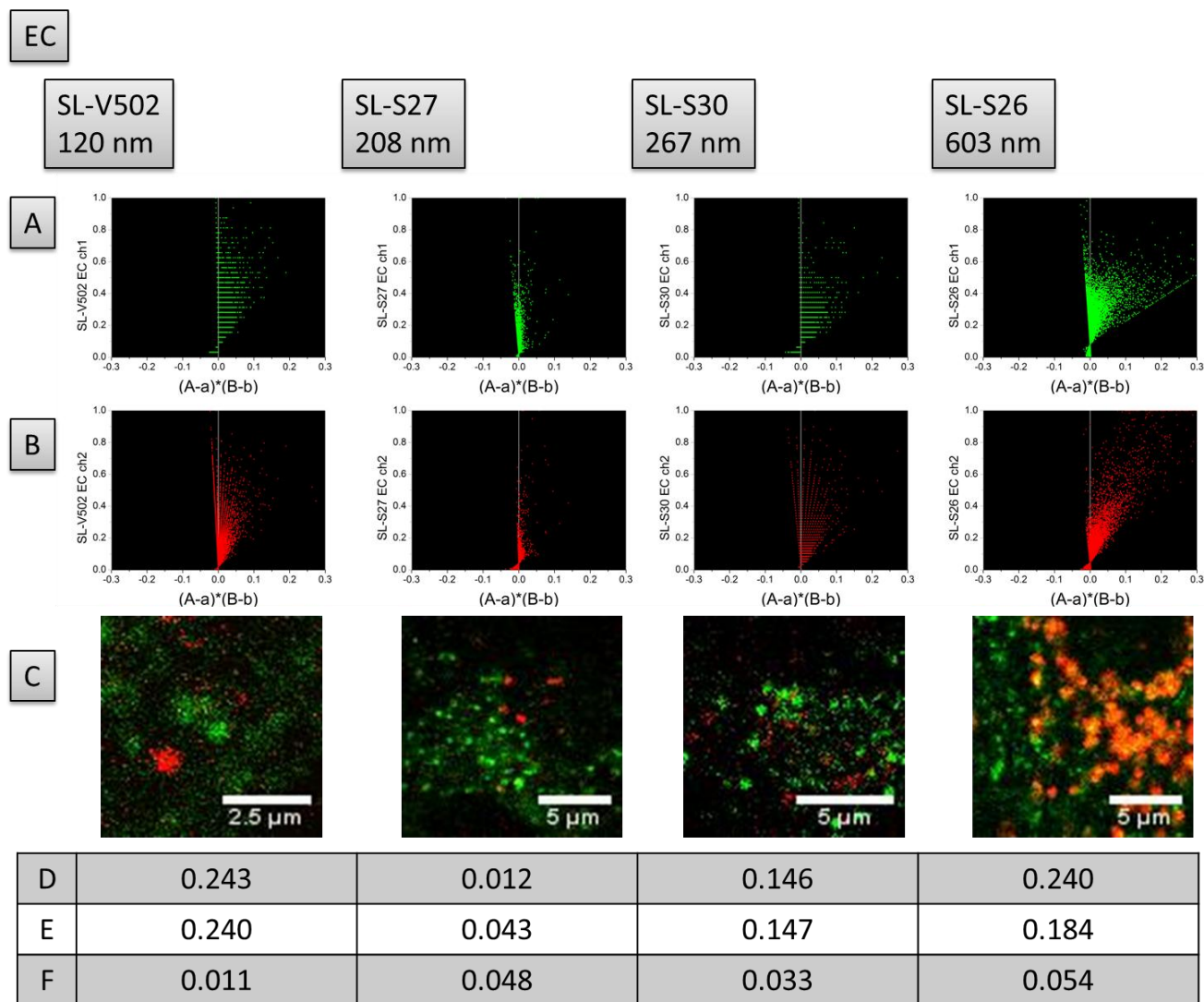
Figure 36: HeLa cells expressing fluorescent EC and incubated with cationic NPs with different sizes. A characteristic of the particles is given in Table 11. A: Diagramm of the PDM values in correlation to the fluorescence intensity of EC (channel 1, green); B: Diagramm of the PDM values in correlation to the fluorescence intensity of the NPs (channel 2, red); C: Merged image of the selected region of interest used for the calculations; D: ICQ value for the selected region of interest as depicted in C; E: mean ICQ (triplicate); F: standard deviation of the mean ICQ.

The PDM plots and ICQ values for CTB are given in Figure 37. The shape of the plots, the channel overlay as well as the ICQ values clearly eliminate a true colocalization. It is very surprising that no colocalization could be found for CTB which was supposed to serve as a positive control as CTB is mainly taken up via caveolin-mediated endocytosis. This could be due to a disposition of the caveolae uptake pathway in a way which is as yet unknown.
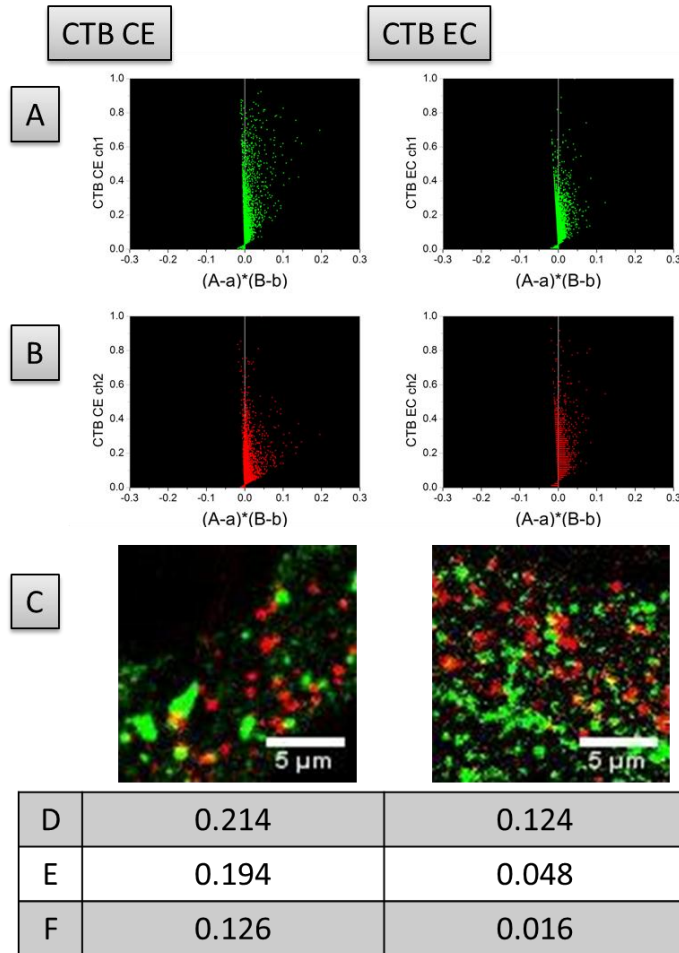
Figure 37: HeLa cells expressing fluorescent CE and EC. A: Diagram of the PDM values in correlation to the fluorescence intensity of CE or EC (channel 1, green); B: Diagram of the PDM values in correlation to the fluorescence intensity of the NPs (channel 2, red); C: Merged image of the selected region of interest used for the calculations; D: ICQ value for the selected region of interest as depicted in C; E: mean ICQ (triplicate); F: standard deviation of the mean ICQ.

An overview of the results is given in Table 14. Taking into account the reduced uptake of NPs into transfected cells in addition to the absence of clear colocalization for cells expressing CE or EC constructs, although a considerable colocalization for all NPs could be found with ICS, it is suggested that both CE and EC constructs, in our hands, severely disrupt caveolin-mediated endocytosis. NPs are then taken up by competing pathways, although to a lesser extent. In addition, the positive control CTB shows no sign of colocalization with caveolin whatsoever. However, caveolin seems to have an influence on the NP uptake, as disrupting of caveolin

mediated endocytosis with CE or EC constructs leads to a down-regulation of the NP uptake kinetic.

Table 14: Colocalization of NPs with CE and EC as determined by ICQ values and PDM plots.

Sample	D_i, nm	Cav-EGFP	EGFP-Cav
SL-V502	120	+ [a]	0
SL-S27	208	0	0
SL-S30	267	0	0
SL-S26	603	0	+
CTB	NA	0	0

[a] **for some large particles; NA: not applicable.**

6.1.6 Conclusions on the route of cellular uptake

Three different techniques were employed to determine the routes of NP uptake to HeLa cells as a function of NP diameter. Macropinocytosis, F-Actin formation, clathrin-mediated endocytosis and dynamin-dependent endocytosis were blocked with pharmacological inhibitors. Immunocytological staining probed the participation of cathepsin D, Lamp1, caveolin-1, clathrin, EEA1 and M6PR on the intracellular fate of NPs. Caveolin-EGFP and EGFP-caveolin expressing HeLa cells were used for uptake inhibition and colocalization studies. An overview over the results is given in Table 15.

.

Table 15: Overview of endocytotic processes found by the uptake of cationic NPs with different sizes.

Sample	MP a)	Actin b)	Clath c)		Dy d)	Cav e)		EE f)	LE g)	Ly h)
			Inh.	ICS		ICS	EGFP			
SL-V502 120 nm	+	+	-	0	+	++	+	+	0	0-
SL-S27 208 nm	+	+	-	0	+	+	+	+	0	0-
SL-S30 267 nm	+	+	-	0	+	++	+	+	+	0
SL-S26 603 nm	+	+	-	0	+	++	+	+	++	0

++: clear colocalization; +: partial colocalization; 0: random colocalization; -: exclusion; NA: data not available. a) macropinocytosis; b) F-actin; c) clathrin as probed with inhibitors and ICS; d) dynamin; e) caveolin as probed with ICS and caveolin mutants; f) early endosome; g) late endosome; h) lysosome.

The uptake of NPs into the endo-lysosomal machinery is dominated by a caveolin-mediated endocytosis. Other pathways, which include macropinocytosis and a dynamin-dependent mechanism but exclude clathrin-mediated endocytosis, also occur. All particles can be found in early endosomes, but only bigger particles showed colocalization in late endosomes. Small particles may feature a different turn-over kinetic within the endo-lysosomal compartments and may already have passed through or not yet arrived within early endosomes. No particles were found in lysosomes, although two different lysosomal proteins were used for detection (cathepsin D and Lamp1). However, a negative signal in ICS does not relevantly mean that the probed proteins do not colocalize with the NPs as ICS only gives a snapshot at one certain time point of a comparably small amount of cells. Localization of NPs within lysosomal compartments remains possible. The data suggests that particles regardless of the size are taken up by a caveolin- and dynamin-dependent mechanism into the endo-lysosomal compartments.

However, the difference between particle sizes regarding early endosomes could be due to a different turn-over kinetic dependent on the particle size. Particles may not yet have arrived in lysosomes or the lysosomal vesicles where particles are located do not feature Lamp1 or cathepsin D.

6.2   Sensor nanoparticles to probe the intracellular pH

NPs are mainly taken up by the cells into the endo-lysosomal compartments, as shown above. Upon ripening from early endosome to lysosome, the pH of these vesicles increases gradually due to a v-ATPase proton pump. The rise in pH triggers specific enzymatic reactions and supports the degradation process of nutrients or other down-regulated proteins. Possessing a thorough knowledge of the acidification process after endocytosis to cells gives insights to intracellular localization of NPs and enables to purposefully design NPs that can release incorporated drugs upon pH trigger at a certain time scale.

To probe the intracellular pH environment of NPs, the pH-sensitive dye SNARF-4F is grafted onto amino-functionalized NPs synthesized with miniemulsion polymerization by an EDC coupling reaction. The pH-sensitive properties are sustained after the coupling process. An intracellular calibration is performed to take intracellular fluorescent changes into account. The environmental pH values of NPs after endocytosis are quantified over time.

6.2.1   Synthesis of amino functionalized particles

For the preparation of amino- and non-functionalized polystyrene particles, the radical miniemulsion polymerization was used, which is a powerful tool for the synthesis of defined functionalized polymeric NPs.

The characteristics of amino-functionalized particles (PS-NH2) and non-functionalized polystyrene used as negative control particles (PS) are summarized in Table 16.

Table 16: Characteristics of polystyrene NP used for the coupling reaction.

Sample	Amount of AEMH[a)], wt%[b)]	D_i, nm	Std-dev[c)], %	Amino groups per nm^{2} [d)]
PS	0	220	9,2	0
PS-NH2	5	255	25	0.31

[a)] *Amino functionalized comonomer (2-amino-ethylmethacrylate hydrochloride),* [b)] *with respect to styrene,* [c)] *standard deviation,* [d)] *as determined by particle charge detection.*

6.2.2 Grafting of pH-sensitive dye onto the nanoparticle surface

After the coupling process, most of uncoupled Snarf-4F molecules is removed by the first centrifugation cycle, as can be seen from the fluorescence measurements of the unpurified sample and the appendant supernatants in Figure 38. The physically adsorbed SNARF-4F is removed by ultrasonication of the purified particles in methanol. Figure 39 demonstrates the fluorescence intensities of the methanol-purified particles with and without amino-functionalization and their corresponding supernatants. The fluorescence intensity of functionalized particles is approx. 70% higher than of non-functionalized particles. Also, the amount of dye removed from the non-functionalized particles is approx. 7 times higher than that of the amino-functionalized particles, suggesting that 15 – 20% physically adsorbed dye is on the particles. The particle diameter increases after the coupling process by approx. 2 nm, which proves that no crosslinking or coagulation of particles occurs. The zeta potential changes from +7.4 mV to -2.9 mV after the coupling reaction and purification, which also indicates a successful reaction as the positive amino functions have been replaced with the negative carboxy-functionalized SNARF-4F.

A quantification of covalently bonded SNARF-4F was tried with fluorescence spectroscopy and NMR measurements. The fluorescence intensity of the unpurified sample can be compared with the supernatant after centrifugation. The difference between the intensities should correlate to the amount of dye that is covalently bounded and physically adsorbed on the particle surface. However, as a 100x excess of dye with respect to the amino functionalization is used, fluorescence spectroscopy was not sensitive enough to detect the changes and was also

influenced by different factors such as scattering of particles, quenching effects of reaction participants etc. Another possibility to quantify the amount of SNARF-4F with fluorescence spectroscopy would be the direct measurement of the particles. However, an adequate calibration cannot be applied as this would require previously defined amounts of covalently bonded SNARF-4F molecules. Quantification with NMR techniques was also not applicable as polystyrene and SNARF-4F were not soluble in different percentages of d-THF/d-MeOH. Other solvents were considered to be poorer solvents for the particle-dye conjugate. The obtained signal of the aromatic groups of polystyrene could not be distinguished from the signal of the aromatic SNARF-4F dye. As SNARF-4F is a dual-wavelength dye, the exact concentration per nm2 on the NP surface is not necessary for determining the intracellular environmental pH of the particles. The important fact is that the pH-sensitive fluorescent spectrum is not altered by the coupling process, which has been ensured.
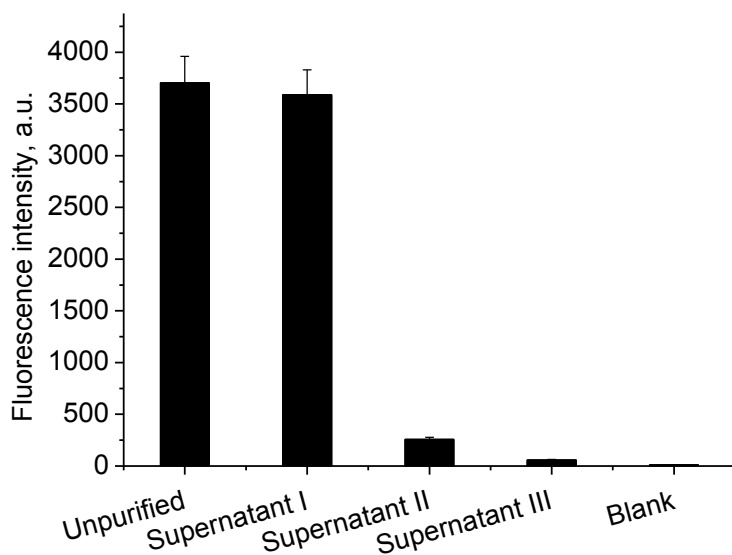

Figure 38: Fluorescence intensities of the sample SNARF-4F-NH2 directly after synthesis and subsequent supernatants of centrifugation / redispersion cycles. All samples were diluted in phosphate buffer pH 8.0 and fluorescence intensities are collected at λ_{Exc} = 542 nm and λ_{Em} = 675 nm (emission wavelength for deprotonated form).
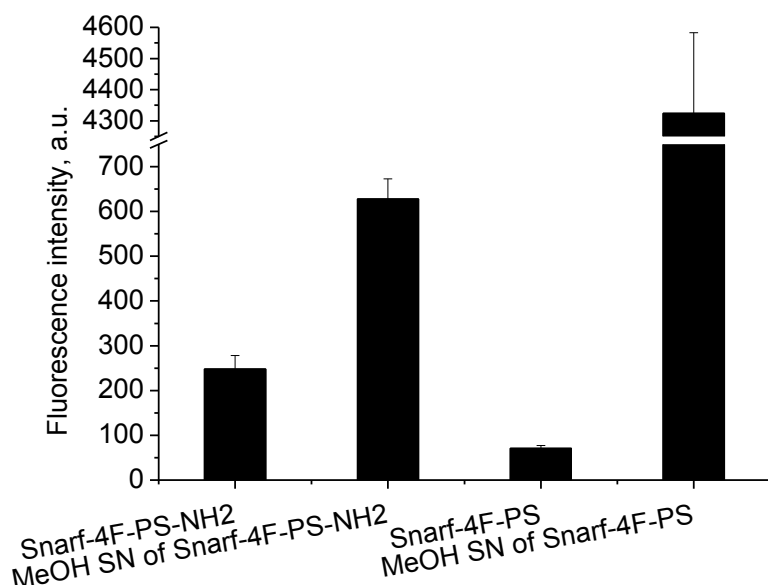
Figure 39: Fluorescence intensities of purified samples SNARF-4F-PS-NH2 and SNARF-4F-PS after washing with methanol and redispersion as well as the fluorescence intensities of freeze-dried and redispersded supernatants (MeOH SN). All samples were ingested after the coupling in phosphate buffer pH 8.0 and fluorescence intensities are collected at $\lambda_{Exc} = 542$ nm and $\lambda_{Em} = 675$

To ensure that the fluorescent properties of the dye are not altered, fluorescence spectra of "free" (not coupled) dye and of SNARF-4F-NPs are compared in Figure 40. For better comparison, the ratios of the protonated and deprotonated emission peaks are given by integrating the spectra over a certain wavelength range (550 – 610 nm for the protonated and 640 – 750 nm for the deprotonated form) to obtain the area under the curve. As can be seen in Figure 41, the ratios of both "free" molecule dye and dye-nanoparticle constructs show the same trend. In the range of pH 6.5 to pH 8.0 the magnitude of the integrated intensities is equal for "free" dye and coupled-to-NP dye. Below pH 6.5 the course of "free" dye differs from the NP dye. This can be due to the scattering effects of the particles, which become eminent at wavelengths closer to the excitation one, which is the case at low pH values. Alternatively, the particles might form a microenvironment at low pH values that differs slightly in pH in comparison to the bulk solution. In general, the pH-sensitive properties of Snarf-4F are not altered by the coupling process and the Snarf-4F NP conjugates can be used for cell uptake experiments.
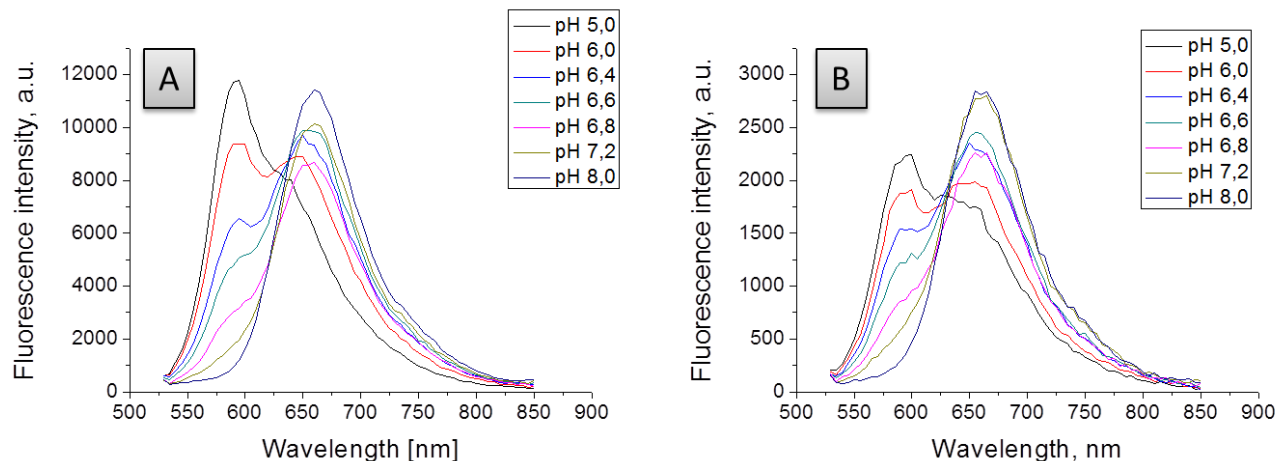
Figure 40: Fluorescence spectra of SNARF-4F "free" dye molecules (A) and SNARF-4F-NP constructs (B) at different pH values in buffer, $\lambda_{Exc} = 514$ nm.
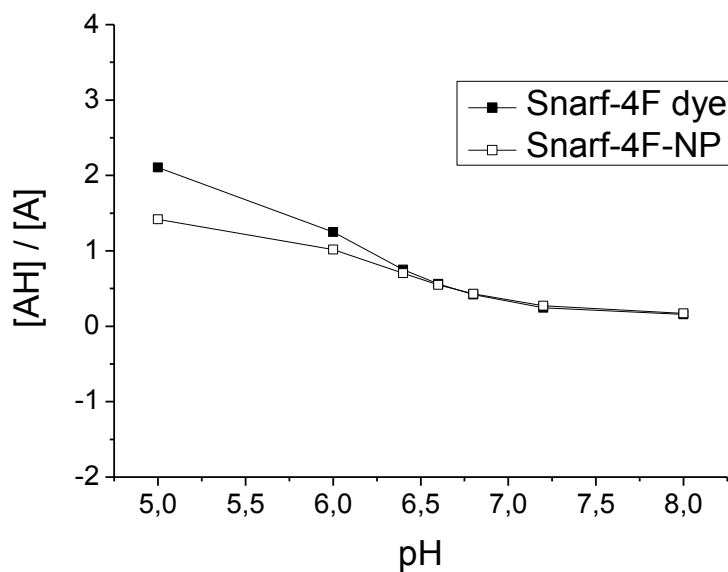

Figure 41: Ratios of emission integrals obtained from the fluorescence spectroscopy of protonated (AH) and deprotonated (A) emission range for the "free" dye and for nanoparticle-dye constructs (see Figure 40; $\lambda_{Exc} = 514$ nm, Integral $\lambda_{EmAH} = 550 – 620$ nm, Integral $\lambda_{EmA} = 650 – 720$ nm).

6.2.3 Intracellular calibration with SNARF-4F AM ester and SNARF-4F-NPs

The fluorescence properties of SNARF-4F may be altered in the presence of cellular components as has been shown by Owen et al. [124], thus an intracellular calibration using platereader spectroscopy and cLSM imaging is performed by loading the cells with SNARF-4F AM ester or

SNARF-4F-NPs (at the three representative pH values 6.0, 7.2 and 8.0). The ester is used because Snarf-4F molecules are to hydrophilic to pass the cell membrane. By introducing ester groups, the molecule becomes hydrophobic enough to enter the cell. In the cytoplasm, the ester is cleaved by unspecific hydrolases and the dye is trapped within the cell. The extracellular and intracellular pH value is equilibrated with the ionophores valinomycin and nigericin [125]. However, it is reported that the intracellular pH in the cytoplasm (pH_i) does not fully adjust to the values of the extracellular pH values (pH_e) in nigericin in high K^+ saline buffer, but deviates by -0.12 +/- 0.02 [141], which must be considered as an additional calibration error.

With platereader spectroscopy, a higher number of samples and cells can be analyzed faster and simultaneously in comparison to cLSM imaging. Figure 42 A shows the ratio of the protonated and deprotonated emission channel after addition of the ionophores at $t = 0$ over time. After approx. 120 s, the equilibration of the intracellular and extracellular pH value is stable and no eminent changes occur. The intracellular pH 6.9 of SNARF-4F AM ester loaded cells is stable over time, too (Figure 42 B). The same pH value was detected for HeLa cells [142]. It was found that the calibration can be fitted binomially, as presented in Figure 42 C. However, platereader measurements only give a mean value of all NPs present in a sample, whereas with the cLSM imaging, the pH environment of single NPs can be probed.
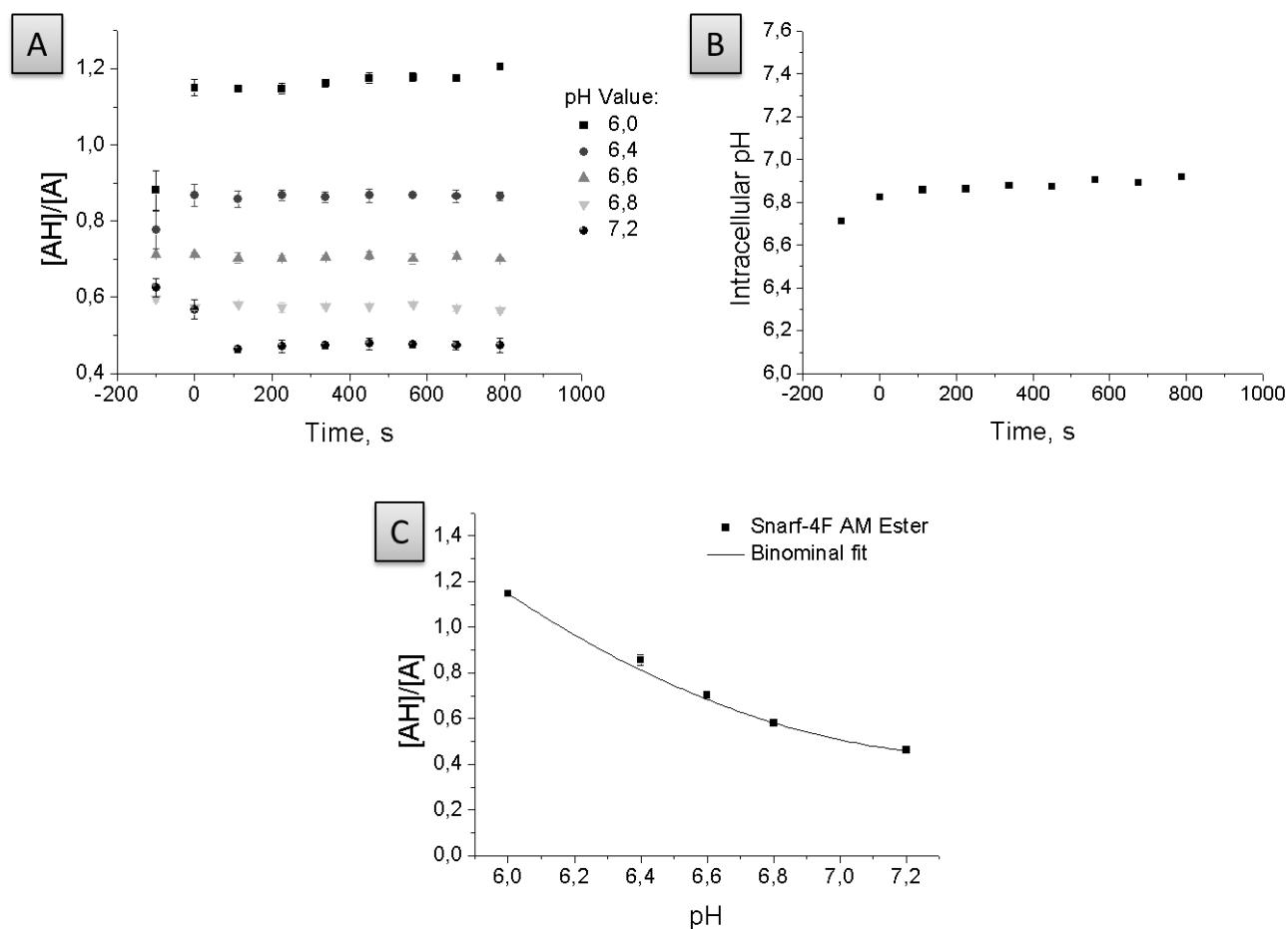
Figure 42: HeLa cells loaded with SNARF-4F AM ester as measured with platereader spectroscopy. A: Time-dependent equilibration after the addition of the ionophores nigericin and valinomycin at t = 0 sec; B: Stability of the intracellular pH of a positive control over time as determined by applying the calibration fit; C: Ratio of protonated (AH) and deprotonated (A) channel as a function of the pH value and the corresponding binominal fit.

cLSM images of SNARF-4F AM ester loaded cells are shown in Figure 44. The dye can be found homogeneously distributed in the cytoplasm of the cells and also in the nucleus. The intensity differences of the two channels at different pH values are shown. SNARF-4F AM ester aggregates may also enter the cell to a small amount via endocytosis [125]. Probably the "spots" which are visible especially at pH 8.0 represent endocytotic vesicles loaded with the dye. However, this does not affect the quality of the calibration, because the ionophores equilibrate the pH not only between the extracellular medium and cytoplasm, but also between cytoplasm and vesicles [143, 144].

The calibration values are fitted binomially, as shown in

Figure 43 and the resulting equation is used to calibrate all further images. Values are estimated as a mean value of several ROIs set within the cells. To prevent severe toxic effects of the ionophores to cells, which might cause the membrane rupture and release of the trapped dye into the medium, the measurements are performed immediately after the addition of ionophores. A positive control of dye-loaded cells gives an intracellular pH of approx. 7.2, which is consistent with previously published values of 7.4 for HeLa cells [142].
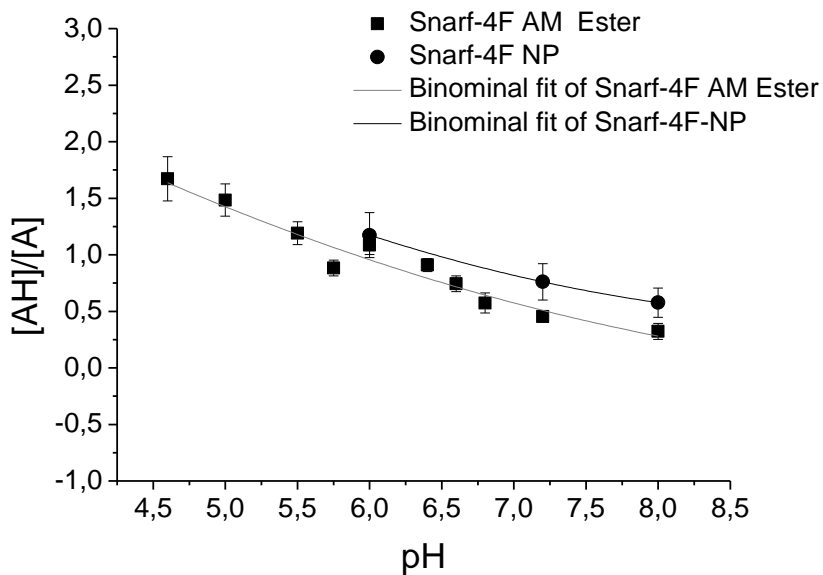

Figure 43: Intracellular ratios of emission integrals obtained from intracellular cLSM imaging of protonated (AH) and deprotonated (A) emission range for the free dye and for nanoparticle-dye constructs.
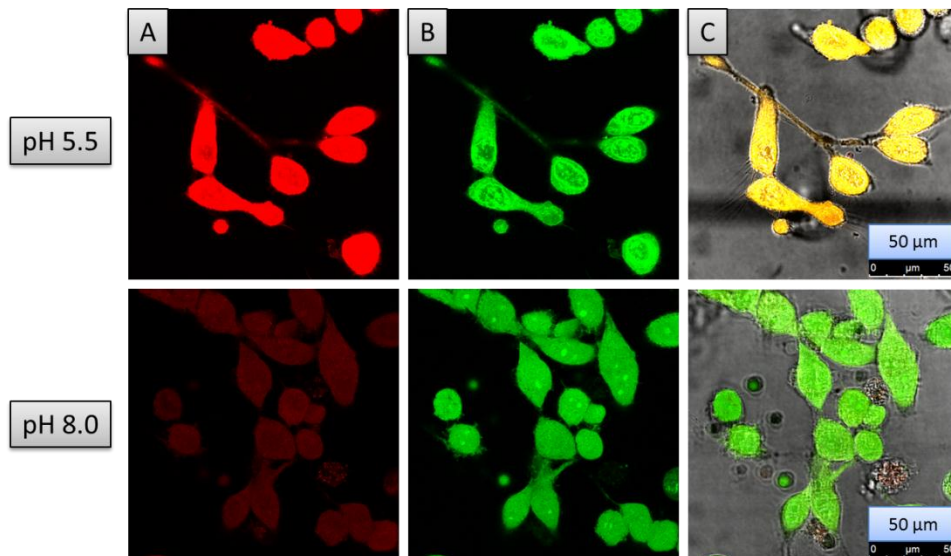
Figure 44: Loading of cells with SNARF-4F AM ester and adjusting the intracellular pH with ionophores as measured with cLSM. A: channel 1 protonated form, B: channel 2 deprotonated form, C: overlay of channel 1, channel 2 and transmission image.

6.2.4 Intracellular probing of NP pH environment

The pH environment of the NPs was monitored by applying the calibration fit function to cLSM images, which were taken after different incubation times. Pseudo-colored pH images and movies were obtained by image batch processing. A self-written batch program automatically executes a macro for the image processing program ImageJ for a given set of corresponding channels. The macro subtracts the background as obtained by a negative control, creates a ratio image, multiplies a mask image with only 0 and 1 values with the ratio image to reduce the noise and applies the binominal fit function and a LUT. The source code for both the automated batch program and the ImageJ macro can be found in the appendage.

The cell viability was investigated by a MTS test. All studied particles were non-toxic with more than 95% living cells after 2 and 24 h of incubation with SNARF-4F-NPs (Figure 45).
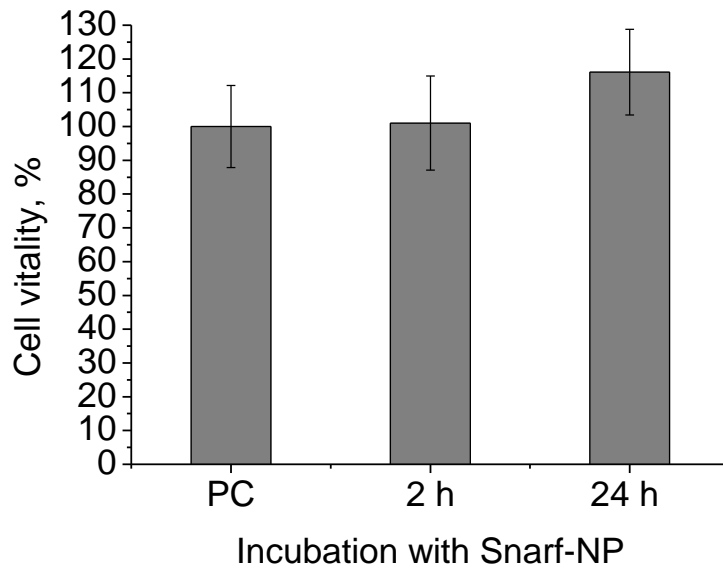
Figure 45: Toxicity of 75 µg · ml⁻¹ SNARF-4F-NPs to HeLa cells after 2 and 24 h incubation as determined by MTS vitality test; PC: Positive control.

Figure 46 shows cLSM image overlay of channel 1, channel 2 and transmission image of HeLa cells incubated with SNARF-4F-NPs for 1, 4 and 24 h and the corresponding pseudocolored images displaying the pH values of the particles. It was possible to determine the pH environment of single nanoparticle spots. The uptake of NPs increases with the time and an acidification (red color) can be observed.
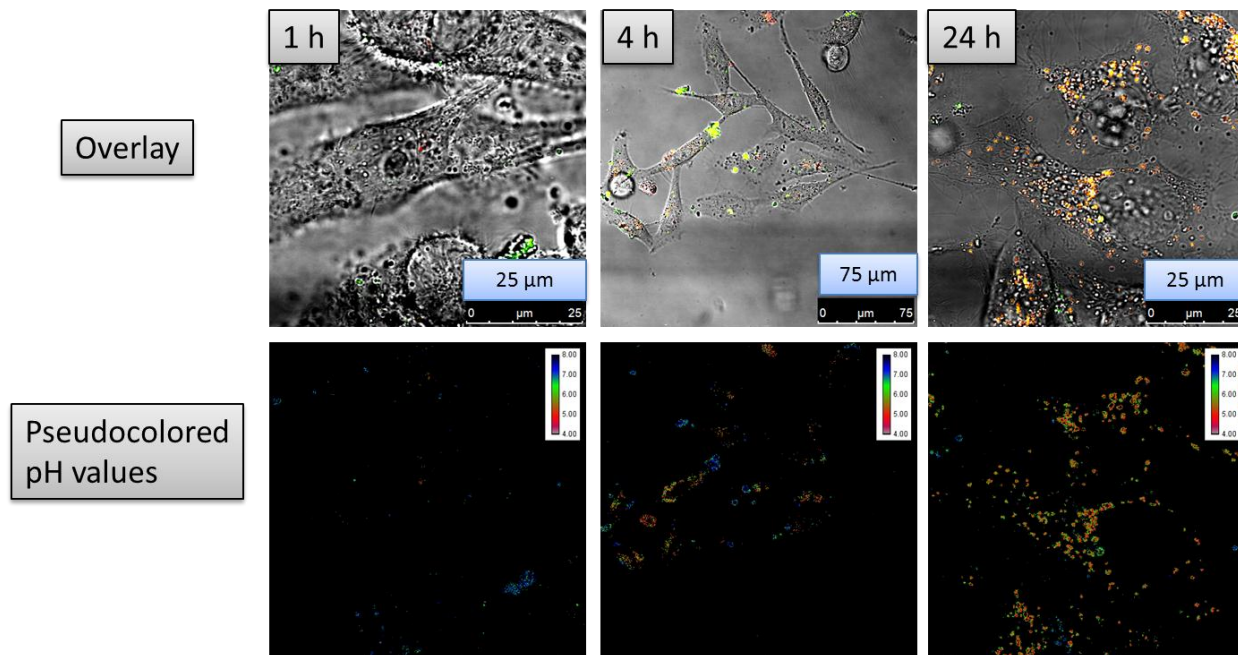
Figure 46: cLSM images of HeLa cells incubated with SNARF-4F-NPs as a channel overlay and as pH value pseudo colored image.

Some particles were found accumulated at the cell surface. With the combination of Snarf-4F-NP constructs with cLSM imaging, it is possible to distinguish between endocytosed particles and those attached to the outer membrane by their environmental pH without staining the membrane as it is usually done in cLSM studies. Figure 47 displays a 3D volume view of a cLSM z-stack with pH pseudo colors after 24 h incubation with SNARF-4F-NPs. The blue spots at a neutral pH indicate NPs accumulated at the cell surface. The red spots, at a more acidic pH, originated from the particles that are endocytosed into the endo-lysosomal compartments.
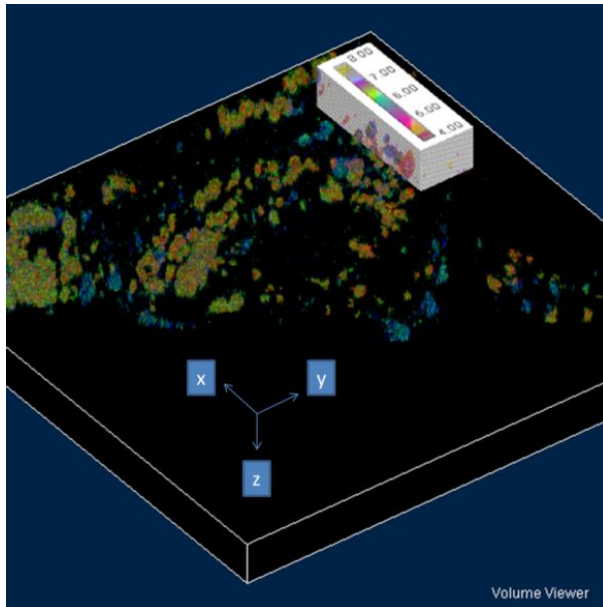
Figure 47: 3D volume view of pH pseudo-colored cLSM z-stack after 24 h incubation of HeLa cells with SNARF-4F-NPs.

Quantification for each image can be obtained using the ImageJ software. As the intensities of the pH values ("y-axis") are dependent on the amount of SNARF-NPs present in the cell, values are adjusted relative to each other. The highest peak of each histogram is set to 1 for comparison reasons. The high resolution of the histogram, which gives values in a 0.02 range (i.e. for pH 4.52, 4.54 and so on) induces a high noise and does not correlate with standard errors of the experiment. Ergo, a smoothing of the data was performed by multiple averages of three values. Figure 48 displays the unprocessed histogram (Figure 48A) and three corresponding smoothed histograms (Figure 48B-D) with a smoothing factor of 1, 2 and 5, respectively.
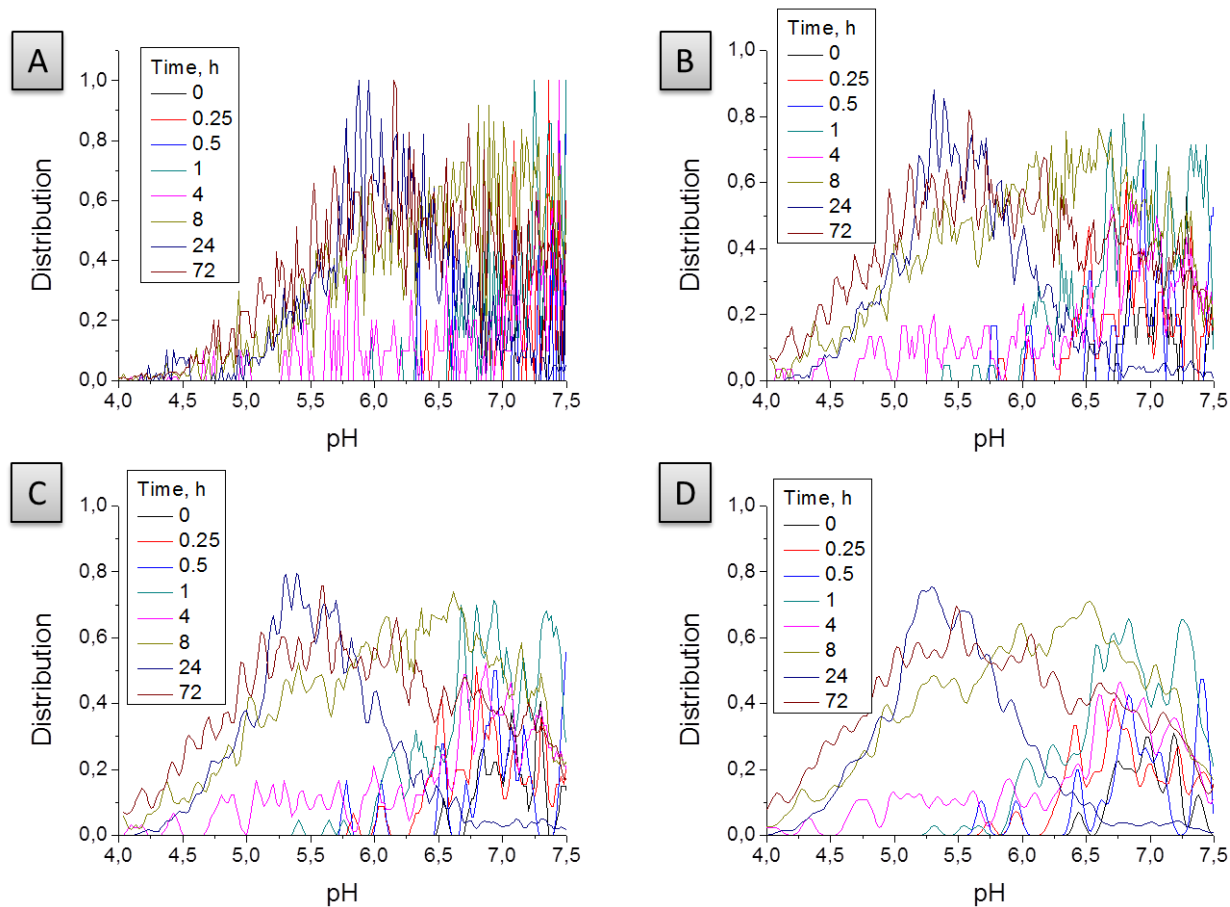
Figure 48: Quantification and data processing of pH values after incubation of SNARF-4F-NPs with HeLa cells for different times. A: Calibrated raw data (the highest value of each data was set to 1); B: Smoothing factor 1; C: Smoothing factor 2; D: Smoothing factor 5.

A time-dependent quantification of the environmental pH value of endocytosed NPs is displayed in Figure 49. Directly after endocytosis (t = 0), NPs are still at a neutral pH range. Between 0.25 and 1 h, some particles are at a slightly more acidic pH value in the range of 6.0, which is typical for early endosomes. The pH value of 6.0 – 5.0, was observed after 4 – 8 h incubation time for some particles, and could be the late endosomes [145]. After 24 h, the majority of particles has undergone an acidification process to acid compartment (pH 5.0 or lower), which are supposed to be lysosomes.
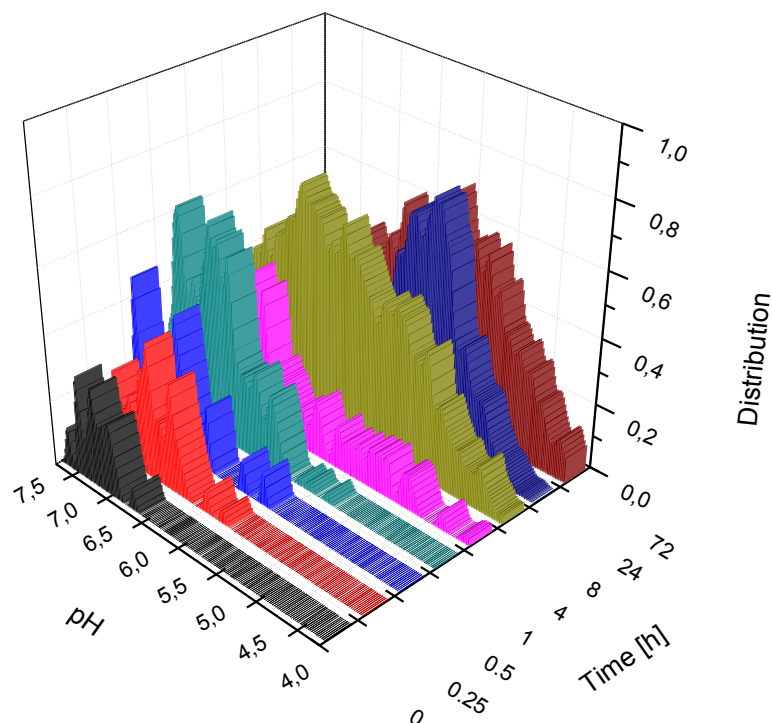
Figure 49: Time-dependent pH distribution of nanoparticle environment after endocytosis to cells.

The proposed acidification process of NPs after their uptake to HeLa cells is shown schematically in Figure 50. Before endocytosis, most of the SNARF-4F molecules on the NP surface are present in the deprotonated form (green stars). During maturation from early to late endosomes and lysosomes, the ratio of protonated (red stars) to deprotonated (green stars) SNARF-4F molecules rises as the pH is lowered by the vacuolar type of H^+-ATPases (V-ATPases) [146] at a much slower rate as it is known for the receptor-mediated endocytosis [145]. This suggests a unique acidification mechanism for NPs that is different than the one for nutrients and other small molecules. The acidification kinetic is important for the design of novel drug delivery systems if the release is triggered by a change in pH. The unique acidification characteristics for NPs shall be taken into account when designing pH-sensitive purpose-driven drug delivery vehicles.
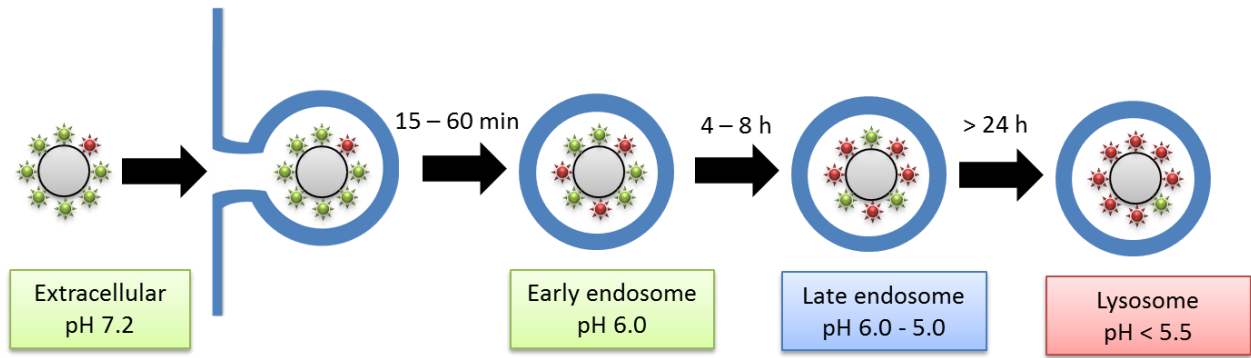
Figure 50: Proposed acidification process of SNARF-4F-NPs after endocytosis to HeLa cells.

7 *Summary and outlook*

What is the intracellular fate of nanoparticles (NPs) taken up by the cells? This question has been investigated in this work for polystyrene NPs of different sizes with a set of molecular biological and biophysical techniques.

Two sets of fluorescent NPs, cationic and non-ionic, were synthesized with three different polymerization techniques. Non-ionic particles with 132, 180, 242, 635, 816 and 846 nm were synthesized with dispersion polymerization in an ethanol/water solution. Cationic NPs with a diameter of 120 nm were synthesized by miniemulsion polymerization. The main step is the formation of a stable oil-in-water emulsion by ultrasonication followed by the particle formation via radical polymerization. Particles with 208, 267 and 603 nm were produced by seeding the 120 nm particle obtained by miniemulsion polymerization with drop-wise added monomer and polymerization of such. The colloidal characterization of all particles showed a comparable amount of the surface groups. In addition, particles were characterized with regard to their size, morphology, solid content, amount of incorporated fluorescent dye and zeta potential. The fluorescent intensities of all particles were measured by fluorescence spectroscopy for calibration in further cellular experiments.

The uptake of the NPs to HeLa cells as measured with flow cytometry after 1 – 24 h revealed a much higher uptake (factor 100) of cationic NPs in comparison to non-ionic NPs. If the same amount of NPs with different sizes is introduced to the cell, a different amount of particles is present in the cell medium, which complicates a comparison of the uptake. The same conclusion is valid for the particles' overall surface area. Therefore, HeLa cells were incubated with the same concentration, amount and surface area of NPs. It was found that with the same concentration always the same polymer amount is taking up by cells. However, the amount of particles taken up decreases for the biggest particles with 603 nm diameter. A correlation to the surface area could not be found. We conclude that particles are endocytosed by an excavator-shovel like mechanism, which does not distinguish between different sizes, but is only dependent on the volume that is taken up. For the decreased amount of large particles, an overload of this mechanism was assumed, which leads to a decrease in the uptake.

The participation of specific endocytotic processes has been determined by the use of pharmacological inhibitors, immunocytological staining and immunofluorescence. The uptake of NPs into the endo-lysosomal machinery is dominated by a caveolin-mediated endocytosis. Other pathways, which include macropinocytosis and a dynamin-dependent mechanism but exclude clathrin mediated endocytosis, also occur as competing processes. All particles can be found to some extent in early endosomes, but only bigger particles were proven to localize in late endosomes. No particles were found in lysosomes; at least not in lysosomes that are labeled with Lamp1 and cathepsin D. However, based on the character of the performed experiment, a localization of particles in lysosomes cannot be excluded.

During their ripening process, vesicles undergo a gradual acidification from early over late endosomes to lysosomes. It is hypothesized that NPs in endo-lysosomal compartments experience the same change in pH value. To probe the environmental pH of NPs after endocytosis, the pH-sensitive dye SNARF-4F was grafted onto amino functionalized polystyrene NPs. The pH value is a ratio function of the two emission wavelengths of the protonated and deprotonated form of the dye and is hence independent of concentration changes. The particles were synthesized by the aforementioned miniemulsion polymerization with the addition of the amino functionalized copolymer AEMH. The immobilization of SNARF-4F was performed by an EDC-coupling reaction. The amount of physically adsorbed dye in comparison to covalently bonded dye was 15% as determined by precipitation of the NPs in methanol, which is a very good solvent for SNARF-4F. To determine influences of cellular proteins on the fluorescence properties, a intracellular calibration fit was established with platereader measurements and cLSM imaging by the cell-penetrable SNARF-4F AM ester. Ionophores equilibrated the extracellular and intracellular pH.

SNARF-4F-NPs were taken up well by HeLa cells and showed no toxic effects. The pH environment of SNARF-4F-NPs has been qualitatively imaged as a movie over a time period up to 1 h in pseudo-colors by a self-written automated batch program. Quantification revealed an acidification process until pH value of 4.5 over 24 h, which is much slower than the transport of nutrients to lysosomes. NPs are present in early endosomes after min. 1 h, in late endosomes at

approx. 8 h and end up in vesicles with a pH value typical for lysosomes after > 24 h. We therefore assume that NPs bear a unique endocytotic mechanism, at least with regards to the kinetic involved. It remains questionable if this acidification kinetic can be altered by specific NP properties, such as charge and size and if it is dependent on the cell type.

8 Zusammenfassung und Ausblick

Welches ist das intrazelluläre Schicksal von Nanopartikeln (NPs), nachdem sie von Zellen aufgenommen wurden? Diese Frage wurde im Zuge dieser Arbeit für Polystyrolpartikel unterschiedlicher Größe untersucht.

Zwei Reihen fluoreszenter NPs, kationisch und nicht-ionisch stabilisiert, wurden mit drei verschiedenen Polymerisationsmethoden synthetisiert. Nicht-ionische Partikel mit 132, 180, 635, 816 und 846 nm Durchmesser wurden mit der Dispersionspolymerisation in einer Ethanol/Wasser-Lösung hergestellt. Kationische NPs mit einem Durchmesser von 120 nm wurden über die Miniemulsionspolymerisation synthetisiert. Der wichtigste Schritt dabei ist die Bildung einer Öl-in-Wasser Emulsion durch Ultraschall und die anschließende Partikelbildung über radikalische Polymerisation. Kationische Partikel mit 208, 267 und 603 nm wurden über tropfenweise Zugabe von Styrolmonomer zu 120 nm großen *Seedpartikeln*, welche mit Hilfe der Miniemulsionspolymerization hergestellt wurden, erlangt. Die kolloidale Charakterisierung ergab, dass alle Partikel eine vergleichbare Anzahl an geladenen Gruppen auf der Oberfläche (Gruppen pro nm^2) tragen. Zusätzlich wurden die NPs nach ihrer Größe, Morphologie, Feststoffgehalt, Menge an eingebrachtem Fluoreszenzfarbstoff und Zetapotential charakterisiert. Die Fluoreszenzintensität wurde über Fluoreszenzspektroskopie bestimmt, um für spätere Zellexperimente als Kalibration zu dienen.

Die Aufnahme von NP nach 1 – 24 h Inkubationszeit, gemessen mit Durchflusszytometrie, zeigte, dass kationische Partikel deutlich besser (mit einem Faktor von 100) in HeLa-Zellen aufgenommen werden als nicht-ionische NPs. Wird dieselbe Menge NPs unterschiedlicher Größe den Zellen dargeboten, ist eine ungleiche Anzahl an Partikeln im Zellmedium vorhanden, was den direkten Vergleich der Aufnahme kompliziert. Dieselbe Schlussfolgerung ist gültig für die Partikeloberfläche. Deshalb wurden HeLa-Zellen mit der gleichen Polymerkonzentration, der gleichen Anzahl an Partikeln sowie der gleichen Gesamtoberfläche inkubiert. Es stellte sich heraus, dass bei gleicher Konzentration immer die gleiche Menge an Polymer aufgenommen wird. Allerdings nahm die Aufnahme der Partikelanzahl für den größten Partikel mit 603 nm ab. Eine Korrelation der Aufnahme zur Oberfläche konnte nicht gefunden werden. Dies erlaubt die

Schlussfolgerung, dass NPs über einen baggerschaufelartigen Mechanismus aufgenommen werden, der nicht zwischen Partikelgrößen unterscheidet und allein vom Aufnahmevolumen abhängt. Für die Abnahme der Aufnahme des größten Partikels kann eine Überladung des Mechanismus' angenommen werden, der zu einer verhältnismäßig reduzierten Anzahl großer NPs in der Zelle führt.

Die Beteiligung von spezifischen Endozytoseprozessen wurde über den Einsatz pharmakologischer Inhibitor, immunzytologischer Färbung sowie Immunfluoreszenz bestimmt. Die Aufnahme von NPs in die endo-lysosomale Maschinerie wird von caveolin-vermittelter Endozytose dominiert. Andere Wege, welche Makropinozytose und einen dynamin-abhängigen Mechanismus ein-, aber clathrin-vermittelte Endozytose ausschließen, kamen auch als konkurrierende Prozesse vor. Clathrin-vermittelte Endozytose spielte hierbei keine Rolle. Alle Partikel waren zu einem kleinen Anteil in frühen Endosomen zu finden, aber nur größere Partikel (267 und 603 nm) kommen in späten Endosomen vor. Partikel wurden nicht in Lysosomen gefunden; zumindest nicht in Lysosomen, welche mit Lamp1 und Cathepsin D markiert waren. Nichtsdestotrotz kann eine Lokalization der Partikel in Lysosomen aufgrund des Charakters des Experiments nicht ausgeschlossen werden.

Während des Reifungsprozesses von frühen über späten Endosomen zu Lysosomen durchlaufen Vesikel eine graduelle Ansäuerung. Es wird angenommen, dass NPs in endo-lysosomalen Kompartimenten eine vergleichbare Veränderung des pH-Werts erfahren. Um den Umgebungs-pH-Wert von NPs nach der Endozytose zu bestimmen, wurde der pH-sensitive Farbstoff SNARF-4F auf aminofunktionalisierte Polystyrolpartikel aufgebracht. Der pH-Wert ist eine Quotientenfunktion der beiden Emissionsbereiche der protonierten und deprotonierten Form des Farbstoffs und ist somit unabhängig von Konzentrationsänderungen. Die Partikel wurden mit der zuvor erwähnten Miniemulsionspolymerisation unter Beteiligung des aminofunktionalisierten Copolymers AEMH synthetisiert. Die Immobilisierung von SNARF-4F erfolgte über eine EDC-Kopplungsreaktion. Die Menge an physikalisch adsorbiertem Farbstoff im Vergleich zu kovalent gebundenem betrug 15%, wie über Fällung der Partikel in Methanol, welches ein sehr gutes Lösungsmittel für SNARF-4F darstellt, ermittelt wurde. Um den Einfluss

von zellulären Bestandteilen auf die Fluoreszenzeigenschaften zu determinieren, wurde ein intrazellulärer Kalibrationsfit über Platereadermessungen und cLSM-Mikroskopie mit dem zelldurchlässigen SNARF-4FAM-Ester etabliert. Ionophoren äquilibrierten dazu den extrazellulären und intrazellulären pH-Wert gleich.

SNARF-4F-NPs wurden gut von HeLa-Zellen aufgenommen und zeigten keine toxischen Effekte. Die von SNARF-4F-NPs gemessenen pH-Werte wurden qualitativ als ein bis zu 1 h dauernder Film in Falschfarben aufgenommen und von einem selbstgeschriebenen automatischen *batch*-Bearbeitungsproramm umgesetzt. Eine Quantifizierung offenbarte, dass der Ansäuerungsprozess bis zu einem pH von 4,5 über 24 h andauert, was sehr viel langsamer ist als der Transport von Nährstoffen in Lysosomen. NPs sind nach mindestens 1 h in frühen Endosomen auffindbar; in späten Endosomen nach ca. 8 h und sie enden in Vesikeln mit einem typischen pH für Lysosomen nach > 24 h. Wir nehmen daher an, dass NPs einen einzigartigen Endozytosemechanismus besitzen, zumindest in Bezug auf die beteiligte Kinetik. Es bleibt fragwürdig, ob die Ansäuerungskinetik von bestimmten NPs Eigenschaften wie z.B. Ladung und Größe, beeinflusst werden kann und ob sie vom Zelltyp abhängig ist.

9 Bibliography

1. Chowdhury, N., *Regulation of nanomedicines in the EU: distilling lessons from the pediatric and the advanced therapy medicinal products approaches.* Nanomedicine, 2010. **5**(1): p. 135-142.

2. Benoy CJ, E.L., Schneider R., *Multiple emulsions, a suitable vehicle to provide sustained release of cancer chemotherapeutic agents.* Br J Pharmacol., 1972. **45**(1): p. 135-136.

3. Green, M.R., et al., *Abraxane®, a novel Cremophor®-free, albumin-bound particle form of paclitaxel for the treatment of advanced non-small-cell lung cancer.* Annals of Oncology, 2006. **17**(8): p. 1263-1268.

4. Montserrat Colilla, M.M., and María Vallet-Regí, *Recent advances in ceramic implants as drug delivery systems for biomedical applications.* Int J Nanomedicine, 2008. **3**(4): p. 403–414.

5. Renn, O. and M. Roco, *Nanotechnology and the need for risk governance.* Journal of Nanoparticle Research, 2006. **8**(2): p. 153-191.

6. Feynmann, R., *There's plenty of room at the bottom*, A.P. Society, Editor. 1959: Caltech.

7. van Schooneveld, M.M., et al., *A fluorescent, paramagnetic and PEGylated gold/silica nanoparticle for MRI, CT and fluorescence imaging.* Contrast Media & Molecular Imaging, 2010. **5**(4): p. 231-236.

8. Costas Kaparissides, S.A., Katerina Kotti and Sotira Chaitidou, *Recent Advances in Novel Drug Delivery Systems.* Journal of Nanotechnology Online, 2006.

9. Minchin, R., *Nanomedicine: Sizing up targets with nanoparticles.* Nat Nano, 2008. **3**(1): p. 12-13.

10. Crespy, D. and K. Landfester, *Miniemulsion polymerization as a versatile tool for the synthesis of functionalized polymers.* Beilstein Journal of Organic Chemistry, 2010. **6**: p. 1132-1148.

11. Landfester, K., A. Musyanovych, and V. Mailänder, *From polymeric particles to multifunctional nanocapsules for biomedical applications using the miniemulsion process.* Journal of Polymer Science Part A: Polymer Chemistry, 2010. **48**(3): p. 493-515.

12. Verena Holzapfel, et al., *Preparation of Fluorescent Carboxyl and Amino Functionalized Polystyrene Particles by Miniemulsion Polymerization as Markers for Cells.* Macromolecular Chemistry and Physics, 2005. **206**(24): p. 2440-2449.

13. Kar P. Lok, C.K.O., *Particle size control in dispersion polymerisation of polystyrene.* Can. J. Chem., 1985. **63**(209).

14. Seigou Kawaguchi, K.I., *Dispersion Polymerization.* Advances in Polymer Science, 2005. **175/2005**(Polymer Particles): p. 299-328.

15. Castelvetro, V., et al., *Role of anionic and nonionic surfactants on the control of particle size and latex colloidal stability in the seeded emulsion polymerization of butyl methacrylate.* Journal of Applied Polymer Science, 2006. **102**(4): p. 3083-3094.

16. Chern, C.-S., et al., *Semibatch Seeded Emulsion Polymerization of Acrylic Monomers: Bimodal Particle Size Distribution.* Journal of Macromolecular Science, Part A: Pure and Applied Chemistry, 1997. **34**(7): p. 1221 - 1236.

17. Hansen, F.K. and J. Ugelstad, *Particle nucleation in emulsion polymerization. II. Nucleation in emulsifier-free systems investigated by seed polymerization.* Journal of Polymer Science: Polymer Chemistry Edition, 1979. **17**(10): p. 3033-3045.

18. Hansen, F.K. and J. Ugelstad, *Particle nucleation in emulsion polymerization. III. Nucleation in systems with anionic emulsifier investigated by seeded and unseeded polymerization.* Journal of Polymer Science: Polymer Chemistry Edition, 1979. **17**(10): p. 3047-3067.

19. Jiang, S., et al., *Seeding as a means of controlling particle size in dispersion polymerization.* Journal of Applied Polymer Science, 2008. **108**(6): p. 4096-4107.

20.   Liu, W.-J., et al., *Interfacial-initiated seeded emulsion polymerization: preparation of polystyrene/poly(methacrylic acid) core/shell particles in the absence of surfactant.* Polymer International, 2006. **55**(5): p. 520-524.

21.   Okubo, M., T. Hosotani, and T. Yamashita, *Influences of the locations of monomer and initiator in the seeded polymerization systems on the morphologies of micron-sized monodispersed composite polymer particles.* Colloid & Polymer Science, 1996. **274**(3): p. 279-284.

22.   Okubo, M., et al., *Preparation of micron-size monodisperse polymer particles by seeded polymerization utilizing the dynamic monomer swelling method.* Colloid & Polymer Science, 1991. **269**(3): p. 222-226.

23.   N. Bechthold, et al., *Miniemulsion polymerization: applications and new materials.* Macromolecular Symposia, 2000. **151**(1): p. 549-555.

24.   Swanson, J.A. and C. Watts, *Macropinocytosis.* Trends in Cell Biology, 1995. **5**(11): p. 424-428.

25.   Wiley, H.S., et al., *The role of tyrosine kinase activity in endocytosis, compartmentation, and down-regulation of the epidermal growth factor receptor.* Journal of Biological Chemistry, 1991. **266**(17): p. 11083-11094.

26.   Benmerah, A., *Endocytosis: Signaling from Endocytic Membranes to the Nucleus.* Current biology : CB, 2004. **14**(8): p. R314-R316.

27.   Vieira, A.V., C. Lamaze, and S.L. Schmid, *Control of EGF Receptor Signaling by Clathrin-Mediated Endocytosis.* Science, 1996. **274**(5295): p. 2086-2089.

28.   Mercer J, S.M., Helenius A., *Virus entry by endocytosis.* Annu Rev Biochem, 2010. **79**: p. 803-33.

29.   Nichols, B., *Caveosomes and endocytosis of lipid rafts.* Journal of Cell Science, 2003. **116**(23): p. 4707-4714.

30.   Hayer, A., et al., *Caveolin-1 is ubiquitinated and targeted to intralumenal vesicles in endolysosomes for degradation.* The Journal of Cell Biology, 2010. **191**(3): p. 615-629.

31.   Malaval, C., et al., *RhoA/ROCK I signalling downstream of the P2Y13 ADP-receptor controls HDL endocytosis in human hepatocytes.* Cellular Signalling, 2009. **21**(1): p. 120-127.

32.   Khandelwal, P., W.G. Ruiz, and G. Apodaca, *Compensatory endocytosis in bladder umbrella cells occurs through an integrin-regulated and RhoA- and dynamin-dependent pathway.* EMBO J, 2010. **29**(12): p. 1961-1975.

33.   Garrett, W.S., et al., *Developmental Control of Endocytosis in Dendritic Cells by Cdc42.* Cell, 2000. **102**(3): p. 325-334.

34.   D'Souza-Schorey, C., et al., *A regulatory role for ARF6 in receptor-mediated endocytosis.* Science, 1995. **267**(5201): p. 1175-1178.

35.   Orth, J.D. and M.A. McNiven, *Get Off My Back! Rapid Receptor Internalization through Circular Dorsal Ruffles.* Cancer Research, 2006. **66**(23): p. 11094-11096.

36.   Urrutia, R., et al., *The dynamins: Redundant or distinct functions for an expanding family of related GTPases?* Proceedings of the National Academy of Sciences, 1997. **94**(2): p. 377-384.

37.   Gratton, S.E.A., et al., *The effect of particle design on cellular internalization pathways.* Proceedings of the National Academy of Sciences, 2008. **105**(33): p. 11613-11618.

38.   Iversen, T.-G., T. Skotland, and K. Sandvig, *Endocytosis and intracellular transport of nanoparticles: Present knowledge and need for future studies.* Nano Today, 2011. **6**(2): p. 176-185.

39.   Kirchhausen, T., E. Macia, and H.E. Pelish, *Use of Dynasore, the Small Molecule Inhibitor of Dynamin, in the Regulation of Endocytosis*, in *Methods in Enzymology*, C.J.D. William E. Balch and H. Alan, Editors. 2008, Academic Press. p. 77-93.

40.   Rejman, J., et al., *Size-dependent internalization of particles via the pathways of clathrin- and caveolae-mediated endocytosis.* Biochem. J., 2004. **377**(1): p. 159-169.

41.   Conner, S.D. and S.L. Schmid, *Regulated portals of entry into the cell.* Nature, 2003. **422**(6927): p. 37-44.

42.   Stenmark, H., *Rab GTPases as coordinators of vesicle traffic.* Nat Rev Mol Cell Biol, 2009. **10**(8): p. 513-525.

43.   Qualmann, B., M.M. Kessels, and R.B. Kelly, *Molecular Links between Endocytosis and the Actin Cytoskeleton.* The Journal of Cell Biology, 2000. **150**(5): p. F111-F116.

44.   Rozelle, A.L., et al., *Phosphatidylinositol 4,5-bisphosphate induces actin-based movement of raft-enriched vesicles through WASP-Arp2/3.* Current Biology, 2000. **10**(6): p. 311-320.

45.   Frischknecht, F., et al., *Actin-based motility of vaccinia virus mimics receptor tyrosine kinase signalling.* Nature, 1999. **401**(6756): p. 926-929.

46.   Merrifield, C.J., et al., *Endocytic vesicles move at the tips of actin tails in cultured mast cells.* Nat Cell Biol, 1999. **1**(1): p. 72-74.

47.   Brodsky, F., *Living with clathrin: its role in intracellular membrane traffic.* Science, 1988. **242**(4884): p. 1396-1402.

48.   Damke, H., et al., *Induction of mutant dynamin specifically blocks endocytic coated vesicle formation.* The Journal of Cell Biology, 1994. **127**(4): p. 915-934.

49.   Herskovits, J.S., et al., *Effects of mutant rat dynamin on endocytosis.* The Journal of Cell Biology, 1993. **122**(3): p. 565-78.

50.   Mu, F.-T., et al., *EEA1, an Early Endosome-Associated Protein.* Journal of Biological Chemistry, 1995. **270**(22): p. 13503-13511.

51.   Saftig, P. and J. Klumperman, *Lysosome biogenesis and lysosomal membrane proteins: trafficking meets function.* Nat Rev Mol Cell Biol, 2009. **10**(9): p. 623-635.

52.   Gieselmann, V., et al., *Biosynthesis and transport of cathepsin D in cultured human fibroblasts.* The Journal of Cell Biology, 1983. **97**(1): p. 1-5.

53.   Behrens, I., et al., *Comparative Uptake Studies of Bioadhesive and Non-bioadhesive Nanoparticles in Human Intestinal Cell Lines and Rats: The Effect of Mucus on Particle Adsorption and Transport.* Pharmaceutical Research, 2002. **19**(8).

54.   Yin Win, K. and S.-S. Feng, *Effects of particle size and surface coating on cellular uptake of polymeric nanoparticles for oral delivery of anticancer drugs.* Biomaterials, 2005. **26**(15): p. 2713-2722.

55.   Lorenz, M.R., et al., *Uptake of functionalized, fluorescent-labeled polymeric particles in different cell lines and stem cells.* Biomaterials, 2006. **27**(14): p. 2820-2828.

56.   He, C., et al., *Effects of particle size and surface charge on cellular uptake and biodistribution of polymeric nanoparticles.* Biomaterials, 2010. **31**(13): p. 3657-3666.

57.   Dash, B.C., et al., *The influence of size and charge of chitosan/polyglutamic acid hollow spheres on cellular internalization, viability and blood compatibility.* Biomaterials, 2010. **31**(32): p. 8188-8197.

58.   Harush-Frenkel, O., et al., *Surface Charge of Nanoparticles Determines Their Endocytic and Transcytotic Pathway in Polarized MDCK Cells.* Biomacromolecules, 2008. **9**(2): p. 435-443.

59.   Hu, L., Z. Mao, and C. Gao, *Colloidal particles for cellular uptake and delivery.* Journal of Materials Chemistry, 2009. **19**(20): p. 3108-3115.

60.   Pang, S.-W., et al., *Effects of charge density and particle size of poly(styrene/(dimethylamino)ethyl methacrylate) nanoparticle for gene delivery in 293 cells.* Colloids and Surfaces B: Biointerfaces, 2002. **26**(3): p. 213-222.

61.   Makino, K., et al., *Phagocytic uptake of polystyrene microspheres by alveolar macrophages: effects of the size and surface properties of the microspheres.* Colloids and Surfaces B: Biointerfaces, 2003. **27**(1): p. 33-39.

62. Harris, T.J., et al., *Tissue-specific gene delivery via nanoparticle coating.* Biomaterials, 2010. **31**(5): p. 998-1006.

63. Lai, S.K., et al., *Privileged delivery of polymer nanoparticles to the perinuclear region of live cells via a non-clathrin, non-degradative pathway.* Biomaterials, 2007. **28**(18): p. 2876-2884.

64. Foged, C., et al., *Particle size and surface charge affect particle uptake by human dendritic cells in an in vitro model.* International Journal of Pharmaceutics, 2005. **298**(2): p. 315-322.

65. P. Decuzzi, M.F., *The Role of Specific and Non-Specific Interactions in Receptor-Mediated Endocytosis of NanoparticlesThe Role of Specific and Non-Specific Interactions in Receptor-Mediated Endocytosis of Nanoparticles.* 2007.

66. Cortez, C., et al., *Influence of Size, Surface, Cell Line, and Kinetic Properties on the Specific Binding of A33 Antigen-Targeted Multilayered Particles and Capsules to Colorectal Cancer Cells.* ACS Nano, 2007. **1**(2): p. 93-102.

67. Zauner, W., N.A. Farrow, and A.M.R. Haines, *In vitro uptake of polystyrene microspheres: effect of particle size, cell line and cell density.* Journal of Controlled Release, 2001. **71**(1): p. 39-51.

68. Rosario M. Sánchez-Martín, L.A., Mark Bradley,, *Multifunctionalized Biocompatible Microspheres for Sensing.* Annals of the New York Academy of Sciences, 2008. **1130**(Fluorescence Methods and Applications: Spectroscopy, Imaging, and Probes): p. 207-217.

69. McClean, S., et al., *Binding and uptake of biodegradable poly--lactide micro- and nanoparticles in intestinal epithelia.* European Journal of Pharmaceutical Sciences, 1998. **6**(2): p. 153-163.

70. Clark, H.A., et al., *Optochemical Nanosensors and Subcellular Applications in Living Cells.* Microchimica Acta, 1999. **131**(1): p. 121-128.

71. Park, E.J., et al., *Ratiometric optical PEBBLE nanosensors for real-time magnesium ion concentrations inside viable cells.* Anal. Chem., 2003. **75**(15): p. 3784-3791.

72. Kreft, O., et al., *Polymer microcapsules as mobile local pH-sensors.* Journal of Materials Chemistry, 2007. **17**(42): p. 4471-4476.

73. Almdal, K., et al., *Erratum: Fluorescent gel particles in the nanometer range for detection of metabolites in living cells.* Polymers for Advanced Technologies, 2007. **18**(12): p. 1020-1020.

74. Iain Johnson, M.T.Z.S., *The Handbook: A Guide to Fluorescent Probes and Labeling Technologies.* 2010. **11th edition**.

75. Cullum, B.M. and T. Vo-Dinh, *The development of optical nanosensors for biological measurements.* Trends in Biotechnology, 2000. **18**(9): p. 388-393.

76. Koo Yong-Eun, L., et al., *Photonic Explorers Based on Multifunctional Nanoplatforms: In Vitro and In Vivo Biomedical Applications*, in *New Approaches in Biomedical Spectroscopy*. 2007, American Chemical Society. p. 200-218.

77. von Werne, T. and T.E. Patten, *Preparation of Structurally Well-Defined Polymer–Nanoparticle Hybrids with Controlled/Living Radical Polymerizations.* Journal of the American Chemical Society, 1999. **121**(32): p. 7409-7410.

78. Kopelman, R., et al., *Multifunctional nanoparticle platforms for in vivo MRI enhancement and photodynamic therapy of a rat brain cancer.* Journal of Magnetism and Magnetic Materials, 2005. **293**(1): p. 404-410.

79. Veiseh, O., et al., *Optical and MRI Multifunctional Nanoprobe for Targeting Gliomas.* Nano Letters, 2005. **5**(6): p. 1003-1008.

80. CHOI, Y.H., et al., *New Method of Preparing a Stable and Functional Antibody-Polymer Nanoparticle Based on Deflocculation via Ultra-Sonication*. Vol. 30. 2009, Seoul, COREE, REPUBLIQUE DE: Korean Chemical Society. 3.

81. Koo Lee, Y.-E., R. Smith, and R. Kopelman, *Nanoparticle PEBBLE Sensors in Live Cells and In Vivo.* Annual Review of Analytical Chemistry, 2009. **2**(1): p. 57-76.

82.   Meallet-Renault, R., et al., *Metal-chelating nanoparticles as selective fluorescent sensor for Cu2+.* Chemical Communications, 2004(20): p. 2344-2345.

83.   M. Brasuel, R.K., I. Kasman, T J Miller, M A Philbert, *Ion concentrations in live cells from highly selective ion correlation fluorescent nano-sensors for sodium.* Sensors 2002. **1**: p. 288 - 292.

84.   Talley, C.E., et al., *Intracellular pH Sensors Based on Surface-Enhanced Raman Scattering.* Analytical Chemistry, 2004. **76**(23): p. 7064-7068.

85.   Anker, J., C. Behrend, and R. Kopelman, *Aspherical magnetically modulated optical nanoprobes (MagMOONs).* Journal of Applied Physics, 2003. **93**(10): p. 6698-6700.

86.   Baunack, S., et al., *Distribution of Ion-Implanted Nitrogen in Iron Alloys Investigated by AES.* Microchimica Acta, 2000. **132**(2): p. 237-242.

87.   Kumar, S., et al., *Plasmonic Nanosensors for Imaging Intracellular Biomarkers in Live Cells.* Nano Letters, 2007. **7**(5): p. 1338-1343.

88.   Brasuel, M., et al., *Fluorescent Nanosensors for Intracellular Chemical Analysis: Decyl Methacrylate Liquid Polymer Matrix and Ion-Exchange-Based Potassium PEBBLE Sensors with Real-Time Application to Viable Rat C6 Glioma Cells.* Analytical Chemistry, 2001. **73**(10): p. 2221-2228.

89.   Davis, C.G., et al., *Acid-dependent ligand dissociation and recycling of LDL receptor mediated by growth factor homology region.* Nature, 1987. **326**(6115): p. 760-765.

90.   Tannock, I.F. and D. Rotin, *Acid pH in Tumors and Its Potential for Therapeutic Exploitation.* Cancer Research, 1989. **49**(16): p. 4373-4384.

91.   Kratz, F., *DOXO-EMCH (INNO-206): the first albumin-binding prodrug of doxorubicin to enter clinical trials.* Expert Opinion on Investigational Drugs, 2007. **16**(6): p. 855-866.

92.   Khramtsov, V.V., *Biological Imaging and Spectroscopy of pH.* Current Organic Chemistry, 2005. **9**: p. 909-923.

93.   Keizer, H.G. and H. Joenje, *Increased Cytosolic pH in Multidrug-Resistant Human Lung Tumor Cells: Effect of Verapamil.* Journal of the National Cancer Institute, 1989. **81**(9): p. 706-709.

94.   Brown, J.Q., et al., *Enzymatic Fluorescent Microsphere Glucose Sensors:Evaluation of Response Under Dynamic Conditions.* Diabetes Technology & Therapeutics, 2006. **8**(3): p. 288-295.

95.   Liu, J., Z. Diwu, and W.-Y. Leung, *Synthesis and photophysical properties of new fluorinated benzo[c]xanthene dyes as intracellular pH indicators.* Bioorganic & Medicinal Chemistry Letters, 2001. **11**(22): p. 2903-2905.

96.   Nozaki, S., *Effects of amounts of additives on peptide coupling mediated by a water-soluble carbodiimide in alcohols.* The Journal of Peptide Research, 1999. **54**(2): p. 162-167.

97.   Goldburg, W.I., *Dynamic light scattering.* American Journal of Physics, 1999. **67**(12): p. 1152-1160.

98.   Sze, A., et al., *Zeta-potential measurement using the Smoluchowski equation and the slope of the current-time relationship in electroosmotic flow.* Journal of Colloid and Interface Science, 2003. **261**(2): p. 402-410.

99.   Böckenhoff, K.B. and W.F. Fischer, *Determination of electrokinetic charge with a particle-charge detector, and its relationship to the total charge.* Fresenius' Journal of Analytical Chemistry, 2001. **371**(5): p. 670-674.

100.   Musyanovych, A., et al., *Effect of Hydrophilic Comonomer and Surfactant Type on the Colloidal Stability and Size Distribution of Carboxyl- and Amino-Functionalized Polystyrene Particles Prepared by Miniemulsion Polymerization.* Langmuir, 2007. **23**(10): p. 5367-5376.

101.   Fuwa, K. and B.L. Valle, *The Physical Basis of Analytical Atomic Absorption Spectrometry. The Pertinence of the Beer-Lambert Law.* Analytical Chemistry, 1963. **35**(8): p. 942-946.

102.   Lakowicz, J.R. and B.R. Masters, *Principles of Fluorescence Spectroscopy, Third Edition.* Journal of Biomedical Optics, 2008. **13**(2): p. 029901.

103. Balke, S.T., et al., *Gel Permeation Chromatography.* Product R&D, 1969. **8**(1): p. 54-57.

104. Mena, J.A., O.T. Ramírez, and L.A. Palomares, *Quantification of rotavirus-like particles by gel permeation chromatography.* Journal of Chromatography B, 2005. **824**(1-2): p. 267-276.

105. Cebecauer, M., et al., *Signalling complexes and clusters: functional advantages and methodological hurdles.* Journal of Cell Science, 2010. **123**(3): p. 309-320.

106. Abbe, E., *Beiträge zur Theorie des Mikroskops und der mikroskopischen Wahrnehmung.* Archiv für Mikroskopische Anatomie, 1873. **9**(1): p. 413-418.

107. Erni, R., et al., *Atomic-Resolution Imaging with a Sub-50-pm Electron Probe.* Physical Review Letters, 2009. **102**(9): p. 096101.

108. Ford, M.G.J., et al., *Simultaneous Binding of PtdIns(4,5)P2 and Clathrin by AP180 in the Nucleation of Clathrin Lattices on Membranes.* Science, 2001. **291**(5506): p. 1051-1055.

109. Moore, C.A.C., S.K. Milano, and J.L. Benovic, *Regulation of Receptor Trafficking by GRKs and Arrestins.* Annual Review of Physiology, 2007. **69**(1): p. 451-482.

110. Wang, L.H., K.G. Rothberg, and R.G. Anderson, *Mis-assembly of clathrin lattices on endosomes reveals a regulatory switch for coated pit formation.* The Journal of Cell Biology, 1993. **123**(5): p. 1107-1117.

111. Roth, M.G., *Integrating Actin Assembly and Endocytosis.* Developmental Cell, 2007. **13**(1): p. 3-4.

112. Peterson, J.R. and T.J. Mitchison, *Small Molecules, Big Impact: A History of Chemical Inhibitors and the Cytoskeleton.* Chemistry & biology, 2002. **9**(12): p. 1275-1285.

113. Kaksonen, M., C.P. Toret, and D.G. Drubin, *Harnessing actin dynamics for clathrin-mediated endocytosis.* Nat Rev Mol Cell Biol, 2006. **7**(6): p. 404-414.

114. Merrifield, C.J., *Seeing is believing: imaging actin dynamics at single sites of endocytosis.* Trends in Cell Biology, 2004. **14**(7): p. 352-358.

115. Marechal, V., et al., *Human Immunodeficiency Virus Type 1 Entry into Macrophages Mediated by Macropinocytosis.* J. Virol., 2001. **75**(22): p. 11166-11177.

116. Ivanov, A.I., A. Nusrat, and C.A. Parkos, *Endocytosis of Epithelial Apical Junctional Proteins by a Clathrin-mediated Pathway into a Unique Storage Compartment.* Mol. Biol. Cell, 2004. **15**(1): p. 176-188.

117. Kerr, M.C. and R.D. Teasdale, *Defining Macropinocytosis.* Traffic, 2009. **10**(4): p. 364-371.

118. Fretz, M., et al., *Effects of Na+/H+ exchanger inhibitors on subcellular localisation of endocytic organelles and intracellular dynamics of protein transduction domains HIV-TAT peptide and octaarginine.* Journal of Controlled Release, 2006. **116**(2): p. 247-254.

119. Macia, E., et al., *Dynasore, a Cell-Permeable Inhibitor of Dynamin.* Developmental Cell, 2006. **10**(6): p. 839-850.

120. Spoden, G., et al., *Clathrin- and Caveolin-Independent Entry of Human Papillomavirus Type 16—Involvement of Tetraspanin-Enriched Microdomains (TEMs).* PLoS ONE, 2008. **3**(10): p. e3313.

121. Li, Q., et al., *A Syntaxin 1, Gαo, and N-Type Calcium Channel Complex at a Presynaptic Nerve Terminal: Analysis by Quantitative Immunocolocalization.* The Journal of Neuroscience, 2004. **24**(16): p. 4070-4081.

122. Bolte, S. and F.P. CordeliÈRes, *A guided tour into subcellular colocalization analysis in light microscopy.* Journal of Microscopy, 2006. **224**(3): p. 213-232.

123. T. Collins, M.B.F. *Online Manual for the MBF-ImageJ collection.* 2009.

124. Owen, C.S., et al., *pH-dependent intracellular quenching of the indicator carboxy-SNARF-1.* Journal of Fluorescence, 1992. **2**(2): p. 75-80.

125. Kao, J.P.Y., *Chapter 7 Practical Aspects of Measuring [Ca2+] with Fluorescent Indicators*, in *Methods in Cell Biology*, N. Richard, Editor. 1994, Academic Press. p. 155-181.

126. Holtzmann, E., *Lysosomes*. 1989, Springer.

127. Fenghua Meng, G.H.M.E., Jan Feijen,, *Polyethylene glycol-grafted polystyrene particles.* Journal of Biomedical Materials Research Part A, 2004. **70A**(1): p. 49-58.

128. JONES, H.W.J., et al., *GEORGE OTTO GEY (1899-1970): The HeLa Cell and a Reappraisal of its Origin.* Obstetrics & Gynecology, 1971. **38**(6): p. 945-949.

129. Walther, P. and A. Ziegler, *Freeze substitution of high-pressure frozen samples: the visibility of biological membranes is improved when the substitution medium contains water.* Journal of Microscopy, 2002. **208**(1): p. 3-10.

130. Julia Dausend, A.M., Martin Dass, Paul Walther, Hubert Schrezenmeier, Katharina Landfester, Volker Mailänder,, *Uptake Mechanism of Oppositely Charged Fluorescent Nanoparticles in HeLa Cells.* Macromolecular Bioscience, 2008. **8**(12): p. 1135-1143.

131. Pelkmans, L., J. Kartenbeck, and A. Helenius, *Caveolar endocytosis of simian virus 40 reveals a new two-step vesicular-transport pathway to the ER.* Nat Cell Biol, 2001. **3**(5): p. 473-483.

132. Li, D., et al., *Critical micelle concentrations of cetyltrimethylammonium chloride and their influence on the periodic structure of mesoporous silica.* Colloid Journal, 2008. **70**(6): p. 747-752.

133. Temporal RM, C.-F.L., Echevarria A, de Souza MA, Sertà M, da Silva-Gonçalves AJ, Pirmez C, Leon LL., *Effects of amidine derivatives on parasite-macrophage interaction and evaluation of toxicity.* Arzneimittelforschung., 2002. **52**(6): p. 489-93.

134. Yamamoto, N., et al., *Dependence of the phagocytic uptake of polystyrene microspheres by differentiated HL60 upon the size and surface properties of the microspheres.* Colloids and Surfaces B: Biointerfaces, 2002. **25**(2): p. 157-162.

135. Baker, P.F., D.E. Knight, and J.R. Garrett, *Calcium Control of Exocytosis and Endocytosis in Bovine Adrenal Medullary Cells [and Discussion].* Philosophical Transactions of the Royal Society of London. B, Biological Sciences, 1981. **296**(1080): p. 83-103.

136. Beutner, D., et al., *Calcium Dependence of Exocytosis and Endocytosis at the Cochlear Inner Hair Cell Afferent Synapse.* Neuron, 2001. **29**(3): p. 681-690.

137. Sankaranarayanan, S. and T.A. Ryan, *Calcium accelerates endocytosis of vSNAREs at hippocampal synapses.* Nat Neurosci, 2001. **4**(2): p. 129-136.

138. Stoorvogel, W., V. Oorschot, and H.J. Geuze, *A novel class of clathrin-coated vesicles budding from endosomes.* The Journal of Cell Biology, 1996. **132**(1): p. 21-33.

139. Nichols, B.J., *A distinct class of endosome mediates clathrin-independent endocytosis to the Golgi complex.* Nat Cell Biol, 2002. **4**(5): p. 374-378.

140. Pelkmans, L., et al., *Caveolin-Stabilized Membrane Domains as Multifunctional Transport and Sorting Devices in Endocytic Membrane Traffic.* Cell, 2004. **118**(6): p. 767-780.

141. Nett, W. and J.W. Deitmer, *Simultaneous measurements of intracellular pH in the leech giant glial cell using 2',7'-bis-(2-carboxyethyl)-5,6-carboxyfluorescein and ion-sensitive microelectrodes.* Biophysical Journal, 1996. **71**(1): p. 394-402.

142. Tafani, M., et al., *Regulation of Intracellular pH Mediates Bax Activation in HeLa Cells Treated with Staurosporine or Tumor Necrosis Factor-α.* Journal of Biological Chemistry, 2002. **277**(51): p. 49569-49576.

143. Doherty, J.J., et al., *Selective degradation of insulin within rat liver endosomes.* The Journal of Cell Biology, 1990. **110**(1): p. 35-42.

144. Galloway, C.J., et al., *Acidification of macrophage and fibroblast endocytic vesicles in vitro.* Proceedings of the National Academy of Sciences, 1983. **80**(11): p. 3334-3338.

145. Geisow, M.J. and W.H. Evans, *pH in the endosome : Measurements during pinocytosis and receptor-mediated endocytosis.* Experimental Cell Research, 1984. **150**(1): p. 36-46.

146. Marshansky, V. and M. Futai, *The V-type H+-ATPase in vesicular trafficking: targeting, regulation and function.* Current Opinion in Cell Biology, 2008. **20**(4): p. 415-426.

10 Appendage

10.1 Source codes for automated batch program

The automated batch program written in Java is used to process cLSM images from two channels into a pseudo colored image that displays the different pH values per pixel. In general, it opens the two images in ImageJ, runs an ImageJ macro and saves the newly generated file and closes all images. The cycle is then repeated.

10.1.1 Batch.bat

Batch.bat opens all images in a specific folder that possess a filename that ends with *ch00* (first channel) and then calls Interm.bat

```
@echo off
setlocal EnableDelayedExpansion
rem MUST be done in windows XP manually in reg Windows Registry Editor Version rem
5.00[HKEY_CURRENT_USER\Software\Microsoft\Command Processor]
rem "DelayedExpansion"=dword:00000001
for %%F in (Series???_????_ch00.tif) do (
call interm.bat %%F
)
```

10.1.2 Interm.bat

Interm.bat renames the filenames of the two images according to the ones given in the macro and then calls Process.bat.

```
set FILE1=%1
set FILE2=%FILE1:ch00=ch01%
set RFILE=%FILE1:ch00=result%
echo call process2.bat %FILE1% %FILE2% %RFILE%
call process.bat %FILE1% %FILE2% %RFILE%
```

10.1.3 Process.bat

Process.bat opens the two images renamed in Interm.bat in ImageJ und runs the macro. The data is saved and all files closed.

```
rem Aufruf mit:
rem call "c:\ImageJ\ImageJ.exe" channel0.tif channel1.tif -macro ..\Macro.txt
@echo off
set FILE1=%1
set FILE2=%2
set RFILE=%3
rem echo "parameters received: " %FILE1% %FILE2% %RFILE%
mkdir work
copy %FILE1% work\channel0.tif
copy %FILE2% work\channel1.tif
cd work
call "c:\ImageJ\ImageJ.exe" channel0.tif channel1.tif -macro ..\Macro.txt
ping 127.0.0.1 -n 7 -w 1000 > nul
taskkill /IM javaw.exe
copy result.tif ..\%RFILE%
del channel0.tif
del channel1.tif
del result.tif
del null.jpg
cd ..
rem rmdir work
echo %RFILE% processed from %FILE1%,%FILE2%
```

10.1.4 ImageJ Macro for image processing

The ImageJ macro subtracts the background as obtained by a negative control, creates a ratio image, multiplies a mask image with only 0 and 1 values with the ratio image to reduce the noise and applies the binominal fit function and a LUT.

```
run("Brightness/Contrast...");
\\Subtract background
run("Subtract...", "value=0.235");
run("Subtract...", "value=0.133");
\\Create and multiply ratio with mask
run("Duplicate...", "title=Mask");
setAutoThreshold();
setThreshold(10, 50);
run("Threshold", "thresholded remaining");
run("Divide...", "value=255");
run("Enhance Contrast", "saturated=0.5");
imageCalculator("Divide create 32-bit", "channel0", "channel1");
\\Apply fit function
run("Multiply...", "value=-1");
run("Add...", "value=15.58489");
run("Multiply...", "value=-0.94632");
run("Add...", "value=14.487235");
run("Square Root");
run("Subtract...", "value=3.80621");
run("Multiply...", "value=-2.11345");
imageCalculator("Multiply create 32-bit", "Result of channel0", "Mask");
\\Set LUT
open("C:\\ImageJ\\lut\\Snarfi.lut");
run("Invert LUT");
setMinAndMax(4.5, 8.1);
```

```
run("Calibration Bar...", "location=[Upper Right] fill=White label=Black number=5 decimal=2
font=12 zoom=1");
saveAs("Tif", "result.tif");
close();
saveAs("jpg", "null.jpg");
close();
saveAs("jpg", "null.jpg");
close();
saveAs("jpg", "null.jpg");
close();
saveAs("jpg", "null.jpg");
close();
saveAs("jpg", "null.jpg");
close();
// run("Close All")
```

11 Acknowledgement

This work would not have come into existence without the support of many helpful, competent, kind and patient people from the Max-Planck-Institute of Polymer Research as well as the rest of the world.

Huge THANKS goes to

- **Name entfernt** for inviting me to Mainz and giving me the opportunity to work in such a formidable interdisciplinary and international environment. Thank you for your great support!
- Many thanks also go to **Name entfernt** for undertaking the task of the second evaluation of this thesis.
- My project **Name entfernt** and **Name entfernt** for mentoring my work, all the scientific discussions and the thorough assistance!
- **Name entfernt** for formidable experimental, theoretical and software assistance,
- The *chemical troop* for all the productive and amiable time in the lab as well as in front of the computer, endless coffee breaks and sufficient supply of sweets and beverages:
- The *Cell lab* for the enjoyable working atmosphere, excellent breakfasts, delicious cakes, teamwork in feeding the ever hungry HeLas and keeping the lab running:
- The Polymeranalytic and EM technicians for their patience, excellent scientific advice and measurements,
- All my friends who had to suffer at some time or another and still talk to me,
- The Aikido group for exhaustive training sessions, pure wasabi sushi, Feuerzangenbowle and the Jazz concert.
- The hiking fellows along the Rhine river,
- The Max-Planck graduate center and SPP1313 combatants for informative and pleasant seminars, retreats and night outs,
- The Max-Planck graduate center and SPP1313 for financial support,
- All the hard-working coffee machines: I value your assiduity!

Moon is no egg, Khaleesi.

It is goddness, wife of sun.

It is known.

12 Curriculum vitae

Simone Lerch
Rembrandtstr. 34
55127 Mainz
Germany

Cell: +49 179 2383676
Simone.Lerch@web.de

Date of Birth: 09/23/1981
Place of Birth: Haan
Children: Hannes Lerch, 12/21/02

Study and career

06/08 – 11/11 Dissertation

Prof. Katharina Landfester, Max-Planck-Institute for Polymer Research, Mainz, Germany

Uptake mechanism and intracellular fate of polystyrene nanoparticles to cells

09/06 – 04/08 Master degree, grade *very good* (1.3)

Biochemistry, University of Ulm, Germany

Master thesis: *Chromatisch unterscheidbare Polystyrolpartikel unterschiedlicher Größe und Oberflächenladung zur simultanen Zellaufnahme*

09/03-08/06   Bachelor degree

Biochemistry, University of Ulm, Germany

03/02-09/03   Parental leave

06/01   Final secondary school examination

Emil-von-Behring Gymnasium, Spardorf, Germany

Stipendia and memberships

10/09-11/11   Max-Planck-Graduate Center with the Johannes-Gutenberg University (MPGC), Mainz

06/08-11/11   Deutsche Forschungsgemeinschaft (DFG), Priority program SPP 1313, *Biological response to nanoscale particles*

Skill enhancement

02/09-03/10   Certificate of the general graduation course of lectures (Allgemeines Promotionskolleg), University of Mainz for *soft skill courses*

02/11   Max-Planck-Graduate Center retreat, soft skill course *Communication*, Cologne, Germany

09/09-10/10   Summer schools
Priority program SPP *1313 Biological response to nanoscale particles*, Tutzing, Germany *Membrane transport*, Sasbach-Walden, Germany
Biomimetric, Segovia, Spain

Teaching activity, student traineeship and assistance

04/08-05/11   Contemporaneous to dissertation
Supervision of student interns
Supervision of the practical course "Advanced physical chemistry"

09/03-04/08   Contemporaneous to master and bachelor studies
Working student at EADS, *Health, safety and environment (HSE)*
Supervision of the practical course "Chemistry for medics"
Student traineeship at Prof. Katharina Landfester, Macromolecular chemistry and Prof. Ulrich Nienhaus, Biophysics
Internship at Thermo Electron, *Peptide synthesis* and at the nuclear medical clinic, Friedrich-Alexander-University Erlangen, *Radio pharmaceutics as tumor labels*

Foreign languages

German   First language
English   Fluently in spoken and written
French   Basic knowledge

Professional skill and interests

IT   MS Office / Origin / ImageJ / Fluorescence microscopy image processing / Flow cytometer data analysis / Endnote / SAP / Latex

Leisure Time   Traveling, Sport (Hiking, Aikido), Theatre, Reading

Publications

13 Publications

Paper

- Cell Uptake Behavior of Non-ionic and Cationic Polystyrene Particles of Different Sizes (in progess)
- pH-sensitive read-out nanoparticles for intracellular probing (in progress)

Talks

- Nanoprobing the pH in intracellular compartments by polymeric nanoparticles, Polymers in Medicine and Biology, Santa Rosa, California, USA
- Miniemulsion synthesis as a versatile platform for surface functionalized nanoparticles, DFG priority program SPP 1313 workshop, Jena, Germany
- Nano – cell interactions, invited talk at the Institute for Medical Microbiology and Hygiene, Dr. Florin, Mainz, Germany

Poster

- *Cellular uptake of polymer nanoparticles: Effect of particle size, surface charge and polymer nature*; A. Höcherl & S. Lerch, K. Landfester, V. Mailänder, and A. Musyanovych; Annual MPIP Meeting at Naurod, 2008
- *Synthesis of Polystyrene Particles for Intracellular Trafficking*; Simone Lerch, S. Glaschick, C.-H. Röcker, M. Dass, U. Nienhaus, V. Mailänder, A. Musyanovych and K. Landfester; DFG SPP1313 Thematischer Workshop I: Zellbiologie / Biofunktionen at Ruderclub an der Alster, Hamburg, 2008
- *Functional Polymeric Nanoparticles for Biomedical Application*; A. Ziegler, A. Höcherl, S. Lerch, H. Keller, V. Mailänder, A. Musyanovych, K. Landfester, 25 years of MPIP, Mainz, 2009
- *Nano – Cell Interactions*; S. Lerch, A. Höcherl, J. Dausend, J.-M. Cramer, N. Kotmann, U. Nienhaus, K. Landfester, V. Mailänder; 25 years of MPIP, Mainz, 2009
- *Functionalized nanoparticles and nanocapsules as markers and nanocarriers in biomedical applications*; G. Baier, A. Höcherl, S. Lerch, U. Paiphansiri, E.- M. Rosenbauer, J. Dausend, K. LandfesterA. Musyanovych ; Frontiers in Polymer science; International Symposium Celebrating the 50th Anniversary of the journal Polymer, 2009

Seite 153

- *Designing non-charged and charged polystyrene nanoparticles with different sizes to study the particle – HeLa cell interaction and uptake kinetic*; S. Lerch, A. Musyanovych, K. Landfester and V. Mailänder; BioNanoMed 2010, Krems, Austria

14 Declaration

I hereby declare that I wrote the dissertation submitted without any unauthorized external assistance and used only sources acknowledged in the work. All textual passages which are appropriated verbatim or paraphrased from published and unpublished texts as well as all information obtained from oral sources are duly indicated and listed in accordance with bibliographical rules. In carrying out this research, I complied with the rules of standard scientific practice as formulated in the statutes of Johannes Gutenberg-University Mainz to insure standard scientific practice.

Simone Lerch

Mainz, November 09, 2011